Universitat
de les Illes Balears

IFISC

Universitat
de les Illes Balears

CSIC

DOCTORAL THESIS
2017

SPIN AND CHARGE TRANSPORT IN THERMALLY AND AC DRIVEN NANODEVICES

Maria Isabel Alomar Bennassar

DOCTORAL THESIS
2017

Doctoral Programme of Physics

SPIN AND CHARGE TRANSPORT IN THERMALLY AND AC DRIVEN NANODEVICES

Maria Isabel Alomar Bennassar

Director: David Sánchez
Tutor: Raúl Toral

Doctor by the Universitat de les Illes Balears

List of Publications

- M. I. Alomar and David Sánchez, Phys. Rev. B **89**, 115422 (2014).
- M. I. Alomar and David Sánchez, in *Dynamical Systems, Differential Equations and Applications*, AIMS Proceedings, pp. 1–9 (2015).
- M. I. Alomar, Llorenç Serra and David Sánchez, Phys. Rev. B **91**, 075418 (2015).
- M. I. Alomar, Jong Soo Lim and David Sánchez, J. Phys.: Conf. Ser. **647**, 012049 (2015).
- M. I. Alomar, Llorenç Serra and David Sánchez, Phys. Rev. B **94**, 075402 (2016).
- M. I. Alomar, Jong Soo Lim and David Sánchez, Phys. Rev. B **94**, 165425 (2016).

Acknowledgments

First of all, I would like to thank David Sánchez for having helped me to strive for the better and succeed for the last six years, first as my master thesis supervisor, and, for the last four years, as my PhD supervisor. I remember when, right after graduation, I had no idea of how to continue my career and, unexpectedly, I met you. Your patience, guidance and optimism motivated me and made me believe that I could indeed follow my way and obtain a PhD in physics. Thanks for believing in me and thanks a lot for having encouraged me to enjoy this experience.

I would also like to thank Llorenç Serra and Jong Soo Lim for their help and collaboration in the development of this thesis and, by extension, all members of the FISNANO group. My gratitude is also extended to Francesca Garcias, for having believed in me during the PhD period. Additional heartfelt thanks to IFISC, for the fantastic work environment, and to the UIB Physics Department, for the position of assistant that has allowed me to carry out this thesis. Finally, many thanks to Jairo Sinova for welcoming me to his group in Mainz for a short stay funded by Fundació La Caixa.

It is now time for my family. What can I say that you don't already know? From my very childhood you have encouraged me to pursue my dreams, and without you I wouldn't be where I am now. Mom, thank you for spending hours doing homework with me. I will never forget the day you ripped off that math sheet from my notebook and you forced me to rewrite it. I remember I couldn't understand why you did it, but now I know that was the best reaction you could have had, because perseverance and self-improvement have paved my way ever since. And dad, oh dad, I think that this "scientifi" spirit of mine comes, largely, from you and from the enthusiasm with which you spent so much time teaching me mathematics, the subject that, all of a sudden, stopped using numbers and became a whole mess of Greek and Latin letters (one alphabet is just not enough for us!). Finally, Toni and Catina, my brother and sister, you are an important part of my life and, although we are not permanently in touch, I know that you will always be by my side, just as I will by yours.

Last, but not least, thank you, Toni Fullana, my partner and fiancé, for having supported me all these years. Since we met the summer right before starting the degree, you have experienced (and suffered!) all the nerves and insecurities that this path entails. Yet, not everything has been bad, we have also celebrated successes and I hope we are able to enjoy many more together. Thanks for encouraging me to be better. I love you.

Agraïments

En primer lloc, vull agrair a David Sánchez el fet d'haver-me ajudat a créixer i superar-me durant aquests darrers sis anys. Els dos primers com a professor del màster i supervisor de la beca de col·laboració i els quatre darrers com a director de tesi. Record que tot just havia acabat la llicenciatura i no sabia quin camí agafar ni què era això de "la investigació" i, sense esperar-ho, et vaig conèixer. Amb la teva paciència, serenitat i optimisme em vas motivar i em vas fer creure que podia seguir aquest camí, que podia aspirar al títol de Doctora. Gràcies per creure en mi i mil gràcies per haver-me encoratjat a viure aquesta experiència.

Com no podria ser d'una altra manera, vull agrair a Llorenç Serra i Jong Soo Lim la seva ajuda i col·laboració en el desenvolupament d'aquesta tesi i, per extensió, a tots els membres del grup FISNANO. També vull agrair a Francesca Garcies el fet d'haver apostat per mi i haver-hi confiat durant aquests anys. Vull donar també les gràcies al IFISC pel fantàstic ambient de feina i al Departament de Física de la UIB per l'ajudantia que m'ha permès dur a terme aquesta tesi. Finalment, vull agrair a Jairo Sinova el fet d'haver-me rebut en el seu grup de Mainz durant una estada curta finançada per la Fundació La Caixa.

Ara arriba el torn de la meva família. Què puc dir que ja no sapigueu? Des de petita m'heu animat a perseguir els meus somnis i heu fet tot el possible perquè pogués arribar on volia, on soc ara. Mamà, gràcies per passar-te hores fent els deures amb mi; sempre recordaré el dia que vas arrabassar-me un full del quadern de matemàtiques i me'l vas fer reescriure. Record que estava bastant brut, però per mi no era necessari repetir-lo i en aquell moment no ho vaig entendre. Ara sé que ho feres per mi i que aquest esperit de constància, superació i perfecció que em vas inculcar, que m'heu inculcat, m'ha ajudat a arribar fins aquí. I papà, ai papà, aquest esperit "científic" crec que ve sobretot de part teva i de l'entusiasme i el temps que vas dedicar a explicar-me les matemàtiques. Matemàtiques que amb el temps han deixat d'utilitzar nombres i han passat a semblarte simplement un caramull de lletres gregues i llatines (no ens basta un sol alfabet). Finalment, Toni i Catina, com a germans meus, sou una part important en la meva vida i, encara que no estiguem permanentment en contacte, sé que sempre estareu al meu costat i jo al vostre.

Per acabar, vull agrair a la meva parella, i futur marit Toni Fullana, el fet d'haver-me fet costat durant tots aquests anys. Anecdòticament ens vam conèixer l'estiu abans de començar la llicenciatura i, per tant, has viscut i sofert tots els nirvis, inseguretats i alts i baixos emocionals que aquest camí comporta. Emperò, no tot ha estat dolent, també hem festejat èxits i esper que en puguem gaudir molts més plegats. Gràcies per animar-me a ser millor. T'estim.

Agradecimientos

Primero quisiera agradecer a David Sánchez el haberme ayudado a crecer y a superarme durante estos últimos seis años. Los dos primeros como profesor del máster y supervisor de la beca de colaboración y los cuatro últimos como director de tesis. Recuerdo que justo acababa de salir de la licenciatura y no tenía ni idea de qué camino escoger ni de qué era esto de "la investigación" y, sin esperarlo, te conocí. Con tu paciencia, serenidad y optimismo me motivaste y me hiciste creer que podía seguir este camino, que podía aspirar al título de Doctora. Gracias por creer en mí y mil gracias por haberme alentado a vivir esta experiencia.

Me gustaría también agradecer a Llorenç Serra y Jong Soo Lim su ayuda y colaboración en el desarrollo de esta tesis y, por extensión, a todos los miembros del grupo FISNANO. También agradezco a Francesca Garcias el haber confiado y apostado por mí durante estos años. Doy asimismo las gracias al IFISC por el fantástico ambiente de trabajo y al Departamento de Física de la UIB por la ayudantía que me ha permitido llevar a cabo esta tesis. Finalmente, agradezco a Jairo Sinova por recibirme en su grupo de Mainz durante una estancia corta financiada por Fundació La Caixa.

Llega el turno de la familia y ¿qué puedo decir que ya no sepáis? Desde pequeña me habéis animado y habéis hecho todo lo posible para que pudiera llegar hasta donde quisiera, hasta donde estoy ahora. Mamá, gracias por pasarte hora haciendo los deberes conmigo, siempre recordaré el día que me arrancaste una hoja del cuaderno de matemáticas y me la hiciste repetir. Recuerdo que estaba bastante sucia, pero para mí no era necesario repetirla y en ese momento no entendí. Ahora sé que lo hiciste por mí y que este espíritu de constancia, superación y perfección que me inculcaste, que me habéis inculcado, me ha ayudado a llegar hasta aquí. Y papá, ay papá, este espíritu "científico" creo que viene en mayor medida de tu parte y del entusiasmo y tiempo que dedicaste a explicarme las matemáticas. Matemáticas que con el tiempo han dejado de utilizar números y han pasado a parecerte simplemente un montón de letras griegas y latinas (no nos basta un solo alfabeto). Finalmente Toni y Catina, como hermanos míos sois una parte importante de mi vida y, aunque no estemos permanentemente en contacto, sé que siempre estaréis a mi lado y yo al vuestro.

Como broche final, agradecer a mi pareja y futuro marido Toni Fullana el haber estado a mi lado durante todos estos años. Anecdóticamente nos conocimos el año justo antes de empezar la licenciatura y, por ello, has vivido y sufrido todos los nervios, inseguridades y altibajos emocionales que esta camino conlleva. Aunque no todo ha sido malo, también hemos festejado éxitos y espero poder disfrutar de muchos más juntos. Gracias por animarme a ser mejor. Te quiero.

Index

List of publications i

Acknowledgments iii

Abstract 1

1 Introduction 7

1.1 Spintronics 7

1.2 Thermoelectricity 10

1.3 Nanodevices 14

1.3.1 Graphene 15

1.3.2 Semiconductor heterostructures 22

1.3.2.1 Two-dimensional Electron Gas 27

1.3.2.2 Quantum Point Contact 30

1.3.2.3 Quantum dot 33

2 Thermoelectric effects in graphene 39

2.1 Theoretical model 39

2.2 Wave matching method 42

2.3 Electric Conductance 45

2.4 Thermoelectric conductance 50

2.5 Seebeck effect 53

2.6 Conclusions 58

3 Seebeck effects in 2D spin transistors 61

3.1 Theoretical model 62

3.2 Current 68

3.3 Charge and spin thermopower 71

3.4 Ferromagnetic contacts 74

3.5 Conclusions 83

4 Nonmagnetic spin transistors 85

4.1 Theoretical model 87

4.2 One-Dimensional case 89

4.3 Quasi-one dimensional case 97

4.4 Conclusions 105

5 Interacting quantum capacitor 107

5.1 Theoretical model 109

5.2 Decoupling scheme 113

5.3 Noninteracting case 115

5.4 Coulomb Blockade Regime 121

5.5 Conclusions 130

6 Concluding remarks 131

A Appendix Scattering approach 139

B Appendix Rashba spin-orbit coupling 145

C Appendix Dirac current 149

D Appendix Interfaces 151

E Appendix Heat transport 153

F Appendix Fourier transform 155

G Appendix Frequency expansion 157

G.1 Noninteracting case 157

G.1.1 Retarded and advanced Green's function 158

G.1.2 Lesser Green's function 159

G.2 Interacting case: Coulomb blockade regime 160

G.2.1 Retarded and advanced Green's function 160

G.2.2 Lesser Green's function 162

H Appendix Hartree approximation 165

References 186

Abstract

This thesis deals with electronic transport in nanodevices driven by temperature gradients or time-dependent potentials. Our emphasis is on both spintronic effects arising from the influence of inhomogeneous spin-orbit couplings and charging effects originated from strong electron-electron interactions in quantum dots.

Chapter 1 is a broad introduction aimed at nonspecialists. We discuss the history of the subject paying attention to the latest developments. We explain the general concepts employed in the rest of this thesis with the objective of offering a self-contained presentation of our research.

In Chapter 2 we investigate the transport properties of a graphene layer in the presence of Rashba spin-orbit interaction. We calculate within the scattering approach the linear electric and thermoelectric responses of a clean sample when the Rashba coupling is localized around a finite region. We find that the thermoelectric conductance, unlike its electric counterpart, is quite sensitive to external modulations of the Fermi energy. Furthermore, we find that the junction thermopower is largely dominated by an intrinsic term independently of the spin-orbit potential scattering.

In order to investigate whether the previous results are similar for a semiconductor heterostructure two-dimensional electron gas (2DEG), in Chapter 3 we consider a spin-orbit-coupled 2DEG under the influence of a thermal gradient externally applied to two attached reservoirs. We discuss the charge, spin and magneto-Seebeck effects also in the ballistic regime of transport at linear response. We find that the charge thermopower (S) is an oscillating function of both the spin-orbit strength and the quantum well width. We also observe that S is always negative for normal leads. When the contacts are ferromagnetic, we calculate the spin-resolved Seebeck coefficient and

investigate its sign changes by tuning the Fermi energy. Additionally, we determine the magneto-Seebeck ratio, which shows dramatic changes in the presence of the Rashba potential.

Because the spin-injection efficiency between dissimilar materials tends to be low, in Chapter 4 we investigate the transmission properties of a spin transistor coupled to two quantum point contacts acting as spin injector and detector. Interestingly, the Rashba interaction can be tuned in such a way that nonuniform spin-orbit fields can point along distinct directions in different points of the sample. We discuss both spin-conserving and spin-flipping transitions as the spin-orbit angle of orientation varies from parallel to antiparallel configuration. Spin precession oscillations are clearly seen as a function of the length of the central channel. Remarkably, we find that these oscillations combine with the Fabry-Perot motion giving rise to quasiperiodic transmissions in the purely one-dimensional case. Furthermore, we consider the more realistic case of a finite width in the transverse direction and find that the coherent oscillations become deteriorated for moderate values of the spin-orbit strength.

In Chapter 5 we consider an interacting quantum dot working as a coherent source of single electrons. The dot is tunnel coupled to a reservoir and capacitively coupled to a gate terminal with an applied ac potential. We investigate the quantized dynamics as a consequence of ac pulses with large amplitude. Within a Keldysh-Green function formalism we derive the time dependent current in the Coulomb blockade regime. We prove that the electron emission and absorption resonances undergo a splitting when the charging energy is larger than the tunnel broadening. Quantization of the charge emitted by the capacitor is reduced due to Coulomb repulsion and additional plateaus arise.

Finally, a summary and outlook of our results are included in Chapter 6.

Resum

En aquesta tesi estudiam les propietats de transport de dispositius electrònics que operen en presència de gradients de temperatura o potencials dependents del temps. Param més atenció als efectes espintrònics resultants d'acoblaments espín-òrbita inhomogenis i als de càrrega originats per la forta interacció entre electrons en punts quàntics.

El capítol 1 és una introducció adreçada a persones no especialitzades en el tema on se n'explica l'evolució històrica, sempre tenint en compte els últims descobriments. A més a més, per tal d'oferir una presentació autònoma de la nostra investigació, exposam els conceptes generals que utilitzam en la resta de la tesi.

En el capítol 2 investigam les propietats de transport d'una capa de grafè en presència d'una interacció espín-òrbita de tipus Rashba localitzada en una regió finita. Utilitzant el formalisme de dispersió, estudiam la resposta lineal elèctrica i termoelèctrica i obtenim que la conductància termoelèctrica, a diferència del seu equivalent elèctric, presenta variacions grans en funció de l'energia de Fermi (E_F). Sorprenentment, hem trobat que la termopotència, en funció de E_F, està dominada per un terme intrínsec que és independent del potencial espín-òrbita de dispersió.

Per tal d'investigar si els resultats anteriors són similars per a un gas d'electrons bidimensional (2DEG), en el capítol 3 consideram un sistema com el del capítol 2 però reemplaçant el grafè per un 2DEG. Estudiam l'efecte Seebeck de càrrega, espín i magnètic també en el règim balístic de transport en resposta lineal i obtenim que la termopotència de càrrega S és una funció oscil·lant de la intensitat espín-òrbita i de l'amplada del pou quàntic amb un valor sempre negatiu per a contactes normals. Quan introduïm contactes ferromagnètics, el coeficient Seebeck d'espín deixa de ser nul i mostra canvis de signe en variar E_F. Així mateix determinam el coeficient Seebeck magnètic, el qual també experimenta canvis de signe en presència del potencial de Rashba.

Pel fet que la injecció d'espín entre materials diferents té una eficiència baixa, en el capítol 4 investigam les propietats de transmissió d'un transistor d'espín en el qual els injectors i detectors magnètics venen donats per contactes de punt quàntic, no contactes ferromagnètics com en el capítol 3. Curiosament, la interacció de Rashba pot manipular-se de tal manera que el camp pot apuntar en diferents direccions al llarg del sistema. Llavors, modificant l'angle d'orientació del camp espín-òrbita des de la configuració paral·lela a l'antiparal·lela estudiam la conservació i el volteig de l'espín. Observam clarament oscil·lacions de precisió en funció de la longitud del canal central i, notablement, aquestes es combinen amb el moviment de Fabry-Perot i donen lloc a transmissions quasi periòdiques en el cas purament unidimensional. Finalment, consideram un cas més realista (amplada finita en la direcció transversal) i obtenim que aquestes oscil·lacions coherents, es deterioren per a valors moderats de la intensitat espín-òrbita.

En el capítol 5 consideram un punt quàntic interactuant que funciona com una font coherent d'electrons individuals. Aquest punt està acoblat mitjançant una barrera túnel a un contacte i es troba subjecte a un potencial ac aplicat a un terminal de porta. Utilitzant el formalisme de funcions de Keldysh-Green, investigam la dinàmica quàntica del sistema com a conseqüència de polsos ac de gran amplitud en el règim de bloqueig de Coulomb. Obtenim que el corrent dependent del temps mostra un desdoblament de les ressonàncies d'emissió i absorció d'electrons quan l'energia de càrrega és més gran que l'eixamplament de túnel. A més, la quantització de la càrrega emesa pel sistema es redueix com a conseqüència de la repulsió de Coulomb i sorgeixen *plateaux* addicionals.

Finalment, el capítol 6 conté les conclusions de la nostra tesi i algunes perspectives dels nostres resultats.

Resumen

En esta tesis estudiamos las propiedades de transporte de dispositivos electrónicos que operan en presencia de gradientes de temperatura o potenciales dependientes del tiempo. Prestaremos atención a los efectos espintrónicos debidos a acoplamientos espín-órbita inhomogéneos y a los de carga originados por la fuerte interacción entre electrones en puntos cuánticos.

El capítulo 1 es una introducción dirigida a personas no especializadas en el tema donde se explica su evolución histórica siempre teniendo en cuenta los últimos descubrimientos. Además, con el fin de ofrecer una presentación autónoma de nuestra investigación, exponemos los conceptos generales que utilizaremos en el resto de la tesis.

En el capítulo 2 investigamos las propiedades de transporte de una capa de grafeno en presencia de una interacción espín-órbita de tipo Rashba localizada en una región finita. Utilizando el formalismo de dispersión, estudiamos la respuesta lineal eléctrica y termoeléctrica, obteniendo que la conductancia termoeléctrica, a diferencia de su equivalente eléctrico, presenta grandes variaciones en función de la energía de Fermi (E_F). Sorprendentemente, hemos encontrado que la termopotencia, en función de E_F, está dominada por un término intrínseco que es independiente del potencial espín-órbita de dispersión.

A fin de investigar si los resultados anteriores son similares para un gas de electrones bidimensional (2DEG), en el capítulo 3 consideramos un sistema como el del capítulo 2 reemplazando el grafeno por un 2DEG. Estudiamos el efecto Seebeck de carga, espín y magnético también en el régimen balístico de transporte en respuesta lineal y obtenemos que la termopotencia de carga S es una función oscilante de la intensidad espín-órbita y del ancho del pozo cuántico con un valor

siempre negativo para contactos normales. Al introducir contactos ferromagnéticos, el coeficiente Seebeck de espín deja de ser nulo y muestra cambios de signo al variar E_F. También determinamos el coeficiente Seebeck magnético, el cual también experimenta cambios de signo en presencia del potencial de Rashba.

Debido a que la inyección de espín entre materiales diferentes tiene una eficiencia baja, en el capítulo 4 investigamos las propiedades de transmisión de un transistor de espín cuyos inyectores y detectores magnéticos vienen dados por contactos de punto cuántico, no contactos ferromagnéticos como en el capítulo 3. Curiosamente, la interacción de Rashba puede manipularse de tal forma que el campo puede apuntar en distintas direcciones a lo largo del sistema. Entonces, modificando el ángulo de orientación del campo espín-órbita desde la configuración paralela a la antiparalela estudiamos la conservación y el volteo del espín. Claramente observamos oscilaciones de precesión en función de la longitud del canal central y, notablemente, estas se combinan con el movimiento de Fabry-Perot dando lugar a transmisiones cuasiperiódicas en el caso puramente unidimensional. Finalmente, consideramos un caso más realista (anchura finita en la dirección transversal) y obtenemos que estas oscilaciones coherentes se deterioran para valores moderados de la intensidad espín-órbita.

En el capítulo 5 consideramos un punto cuántico interactuante funcionando como una fuente coherente de electrones individuales. Dicho punto está acoplado mediante una barrera túnel a un contacto y se halla sujeto a un potencial ac aplicado a un terminal de puerta. Utilizando el formalismo de funciones de Keldysh-Green, investigamos la dinámica cuántica del sistema como consecuencia de pulsos ac de gran amplitud en el régimen de bloqueo de Coulomb. Obtenemos que la corriente dependiente del tiempo muestra un desdoblamiento de las resonancias de emisión y absorción de electrones cuando la energía de carga es mayor que el ensanchamiento túnel. Además, la cuantización de la carga emitida por el sistema se reduce debido a la repulsión de Coulomb y surgen *plateaux* adicionales.

Finalmente, el capítulo 6 contiene las conclusiones de nuestra tesis y perspectivas de nuestros resultados.

1. Introduction

1.1 Spintronics

Spintronics is the branch of science that studies spin phenomena in metals, semiconductors and semiconductor heterostructures. Its goal is to determine the electric, optic and magnetic properties of solids in the presence of nonequilibrium spin populations. More specifically, spintronics aims at understanding spin-polarized transport phenomena in metals and semiconductors to find an effective way to control their electric properties through spin and magnetic fields or, inversely, to manipulate the spin and magnetic properties with electrical currents or gate voltages.

Mott, in 1936, pioneered the study of spin dependent transport in ferromagnetic (FM) metals [1, 2]. He proposed that the charge current could be separated into two independent spin currents. As a consequence, the conductivity could be written in terms of two independent, although spin dependent, conductivities. In 1976, Aronov, motivated by Mott's predictions, proposed the idea of creating a nonequilibrium spin distribution in nonmagnetic (NM) materials [3]. Stimulated by these studies, only a decade later, Johnson and Silsbee demonstrated the first spin injection transport process in aluminium [4]. As a result of these developments, new possible applications as for example devices based on the giant magnetoresistance [5] and tunnel magnetoresistance effects [6] emerged. Magnetoresistance effects are used to read and write nonvolatile information on magnetic disks due to their ability to detect different magnetic states as high or low voltage, depending on the magnetization direction. However, in metals the spin diffusion length is short and the charge carrier concentration is fixed. Thus, the next step was to use semiconductors for spintronic studies because of their variable concentration of carriers by doping, their response to electric field via gating and their long

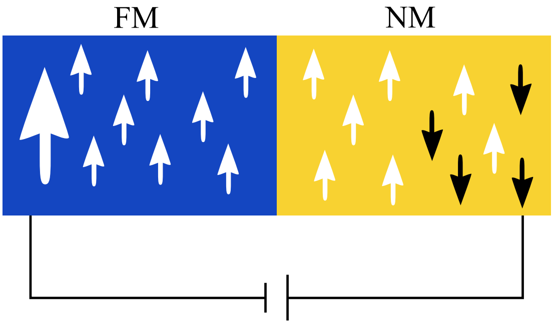

Figure 1.1: Schematic representation of a spin injection process where spin is electrically injected from a ferromagnetic material into a nonmagnetic material. Reproduced from Ref. [7].

spin coherence times.

There are different ways to create spin accumulations electrically. The most common one is using FM contacts to inject spin polarized currents into a NM material. In Fig. 1.1 we represent the simplest spin injector comprising a FM material attached to a NM material. When an electric current flows from the FM material, where the majority of electrons has the spin pointing in the same direction, to the nonmagnetic material, a nonequilibrium spin accumulation is created in the latter. In other words, the application of a charge current transforms the spin polarization in the FM metal into a spin polarized current that can be detected or manipulated [7]. This is the method which we will analyze in Chapter 3. However, the spin-injection efficiency between dissimilar materials tends to be low. In Chapter 4, we will use a pair of quantum point contacts (QPCs) as spin injectors and detectors [8, 9]. In the point constrictions, the electric confinement leads to an effective magnetic field that polarizes the electrons. Now, our system relies on a semiconductor-only structure and the problem mentioned above can be solved. Another important feature is that it is fully nonmagnetic. Hence, we do not need ferromagnetic contacts to polarize the electrons.

A key proposal in semiconductor spintronics is an analogue for electronic devices that improves the existing semiconductor technology: the spin transistor proposed by Datta and Das, in 1990 [10]. In Fig. 1.2 we sketch the Datta-Das spin transistor. Two FM electrodes

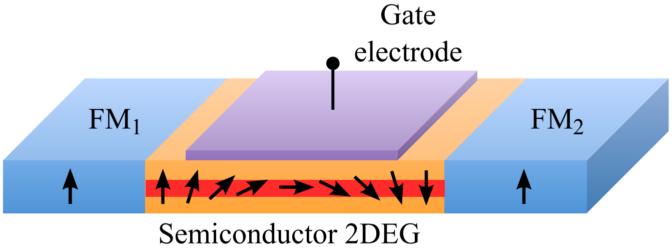

Figure 1.2: Schematic representation of a Datta-Das spin field effect transistor (sFET) where a two-dimensional electron gas semiconductor heterostructure is attached to two ferromagnetic contacts. The injected spins can be modulated by the gate electrode with an external electric field and, depending on the strength of the spin-orbit coupling, the spin transistor is ON (nonzero current) or OFF (zero current). In the same way, depending on whether the two electrodes have antiparallel or parallel magnetization for a fixed spin-orbit coupling strength one obtains the same effect.

are attached to a two-dimensional electron gas, which represents the transport channel. As described in Fig. 1.1, a current flows from the FM to the NM material and spins are injected in the NM material. Then, in the central region, using the spin properties of the spin-orbit coupling of the Rashba type (see Sec. 1.3.2.1), we can manipulate the electron spin direction with an external electric field. Consequently, the electrons feel an effective magnetic field perpendicular to the motion direction and the spins precess around this field with a single precession frequency, assuming that the transversal transport is ballistic and one-dimensional. Manipulating this strength with a capacitively coupled gate electrode the electrons can enter or bounce off the right FM electrode, in which case we can say that the spin transistor operation point is ON or OFF, respectively. The possibility for the electron to be transmitted into the right electrode depends on the relative orientation between the impinging spin and the FM magnetization. The Datta-Das transistor behavior has been partially confirmed due to a number of problems, as for instance the low conductivity mismatch between dissimilar materials (which we mentioned above), the presence of impurities in the two-dimensional electron gas that causes the transport to be no longer ballistic and interference effects arising from multiple reflections.

In Chapter 4 we will study the Datta-Das effect in a two-dimensional spin transistor where, as we have mentioned above, the spin injector and detector are QPCs. We will demonstrate that oscillations arise due to the Datta-Das effect in the transmission probability. The presence of these oscillations depends on the relative orientation between the QPC effective magnetic field and the spin-orbit interaction in the central region.

1.2 Thermoelectricity

One of the main goals in condensed matter physics is the study of waste-heat recovery systems [11] and here is where thermoelectricity plays an important role [12] since thermoelectric devices are basically solid-state devices that convert energy between the electric and thermal components of a system. Then, thermoelectricity studies the relation between the generation of electric currents, or voltage differences, due to thermal gradients and vice versa.

During the first half of the 19th century thermoelectric effects were primarily studied by Thomas Johann Seebeck, Jean-Charles Peltier, and William Thomson [13]. They found a coupling of the electric charge transport with the heat transport. However, it was not until the late 1950s when the use of semiconductor materials, which provide high performances, became popular, increasing the applicability of these devices.

In the present thesis, we will focus on thermoelectric effects in low-dimensional systems (e.g., two-dimensional electron gases and quantum point contacts). This kind of systems were first proposed by Hicks and Dresselhaus [14], who demonstrated that small conductors could be more efficient for thermoelectric applications. Another important characteristic lies in the fact that in low-dimensional systems at least one of the dimensions is restricted. This quantum confinement leads to discrete energy levels. At these scales, such electronic energy levels can be manipulated. This property provides great control over the device's thermopower, which determines its ability to generate a voltage difference due to a temperature bias.

The first thermoelectric effect was discovered by T. J. Seebeck in 1821 [16]. He observed that a circuit made of two dissimilar metals with junctions at different temperatures (see Fig. 1.3) deviated a

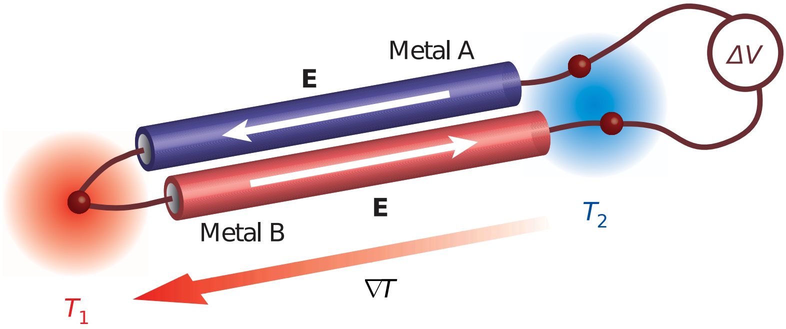

Figure 1.3: Pictorial representation of a thermocouple with two different metals, A and B, and junctions at different temperatures, T_1 and T_2. ΔV is the voltage generated due to $\Delta T = T_1 - T_2$. Reproduced from Ref. [15].

compass magnet. The first hypothesis was that there should be magnetism induced by the temperature difference, ΔT, maybe related to the Earth's magnetic field. However, he quickly realized that a "Thermoelectric Force" induced an electrical current, which by Ampere's law deflects the magnet. In other words, an electrical potential was created due to ΔT, driving an electric current in a closed circuit. Nowadays, this is known as the Seebeck effect. He also observed that the generated voltage ΔV, also called thermovoltage V_{th}, was proportional to ΔT. The proportionality constant is termed Seebeck coefficient or thermopower, S.

From a fundamental point of view, the generation of ΔV in a metal is due to the different carrier energies at the hot and cold ends. Indeed, the charge carriers in the hot side have higher thermal velocities than in the cold side and, as a consequence, they diffuse more quickly from the hot side to the cold side than in the opposite direction. If the thermal gradient is maintained, the flowing charge carriers accumulate on the cold side and this separation of charge create a ΔV. This voltage difference divided by the temperature difference across the material is precisely the Seebeck coefficient, S, which is material-dependent.

In 1834 a second thermoelectric effect was discovered by J. Peltier. He observed that when a current flows through a circuit made of two different metals a small cooling or heating effect appears in the junction depending on the current direction [16]. In metallic thermocouples the reversible thermoelectric effects are always accompanied by irreversible phenomena of Joule heating and thermal conduction. For this reason, the best way to demonstrate the Peltier effect is by comparing that, when a current flows in one direction, the heating is lower in the other direction. The proportionality constant between the heat absorbed or created and the electrical current is dubbed Peltier coefficient, Π. In 1838, Lenz showed that this heat could be used to freeze water or, reversing the current, to melt ice.

It turns out that both the Seebeck effect and the Peltier effect obey a reciprocity relation. In 1855 W. Thomson (who later became Lord Kelvin) suggested that the thermopower and the Peltier coefficient are indeed connected. A rigorous proof of this is due to L. Onsager, who applied the microreversibility principle to show reciprocal relations between a general class of thermodynamic forces and flows [17]. In 1945 Casimir discussed in detail the Onsager relations for the case of electric transport [18]. The Onsager-Casimir relations represent a cornerstone of modern transport theories [19] and are also verified in the quantum regime [20, 21].

It is worth noting that in order to obtain high values of thermopower we need that the transmission probability between the two sides of the system depends strongly on energy, i.e., it is necessary to have a system with asymmetric density of sates. If the density of states is symmetric we do not have any thermoelectric effects due to a perfect cancellation between electron- and hole-like fluxes, despite electrical transport effects do exist.

Very recently, a new field called spin caloritronics investigates the coupling between spin-dependent currents and temperature differences [22]. The spin Seebeck effect was recently discovered in a metallic ferromagnet [15], where a temperature difference generates a spin flux that can be electrically detected using the inverse spin Hall effect [23]. Therefore, in a spin caloritronic device heat is converted into a magnetic current, which may lead to exciting prospects for low-dissipation, fast electronic applications. Lately, the spin Seebeck effect has been also observed in spin ferromagnetic semiconductors [24] and even nonmagnetic materials [25].

Quite generally, consider a conductor coupled to external electrodes. These are described by electrochemical potentials and con-

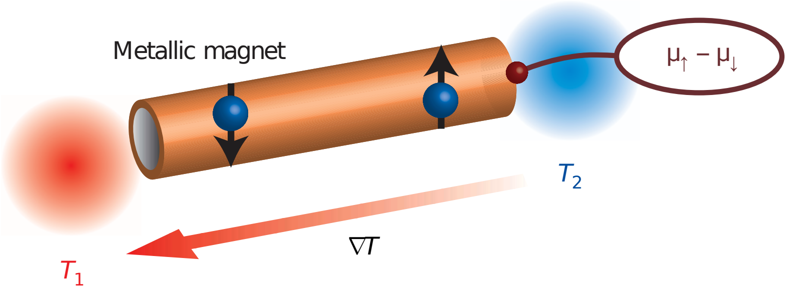

Figure 1.4: Sketch of the spin Seebeck effect, where the spin-up (↑) and spin-down (↓) conduction electrons of a metallic magnet have different Seebeck coefficients. Similarly to the Seebeck effect, when we apply a temperature gradient through the metallic magnet a spin voltage $(\mu_\uparrow - \mu_\downarrow)/e$ proportional to the temperature difference $\Delta T = T_1 - T_2$ appears. Reproduced from Ref. [15].

tact temperatures. In the absence of spin biases, an applied thermal gradient will create a bias voltage under open-circuit conditions (no charge current). This is the Seebeck coefficient as discussed earlier (see Fig. 1.4). The spin Seebeck coefficient, S_S, is defined in a similar way but assuming that the spin current vanishes in the conductor for a given thermal gradient. Therefore, a spin imbalance is created between electrons with opposite spins at the sides of the sample. A new effect shows up if we attach ferromagnetic electrodes to our system and measure the thermopower for parallel and antiparallel magnetization orientations. The difference between them is what we know as magneto-Seebeck ratio [26], S_{MS}. Then, the magneto-Seebeck effect quantifies changes in S of a magnetic junction upon switching the leads' magnetic moments.

For a two-dimensional spin transistor, we will demonstrate in Chapter 3 that the spin Seebeck coefficient and magneto-Seebeck ratio are strongly modulated with a Rashba spin-orbit coupling, whose strength can be externally tuned with a nearby gate contact. The effect is visible when the attached ferromagnetic electrodes have parallel or antiparallel magnetization orientations. This opens up the path to manipulate spin currents using a combination of applied electric fields and temperature biases in a low-dimensional system.

1.3 Nanodevices

We have already stressed the importance of nanoscale systems in spintronic and thermoelectric setups. We now discuss their general properties in more detail.

Nanodevices or mesoscopic systems are artificial structures of nanometer size. During the last decades mesoscopic physics has evolved into a rapidly progressing and exciting interdisciplinary field. Mesoscopic conductors belong to a class of systems between microscopic objects, such as atoms, and macroscopic bodies, e.g., traditional condensed-matter systems. The way to study macroscopic systems is involved because, on the one hand, the theoretical approaches applied to macroscopic systems need to account for quantum effects and, on the other hand, microscopic approaches are too sophisticated for mesoscopic systems due to their size and complexity. Then, nanodevices frequently exhibit both classical and quantum behaviors.

Due to the interdisciplinarity of mesoscopic physics, the systems that show a mesoscopic behavior can be found in different fields of physics. We will focus on two-dimensional electron systems as graphene or semiconductor heterostructures of reduced dimensionality.

Disordered metals were the first mesoscopic systems to be studied [27]. However, the confinement of electrons in nanostructures of controllable geometry was possible only with the appearance of high-mobility semiconductor heterostructures [28]. These form the basis of two-dimensional electron gases (2DEGs), and facilitate the development of lithographic techniques. In this kind of systems, impurity scattering is almost negligible and transport is ballistic. The only allowed scattering is from specular reflection at the boundaries.

Ballistic microstructures are very useful for studies on mesoscopic physics. The first reason is related to the Fermi wavelength λ_F, which is usually the lowest length scale. More precisely, λ_F is much shorter than the typical system size a (including the extreme limit of zero-dimensional systems, quantum dots). Another aspect to take into account is that mesoscopic systems are influenced by different effects such as temperature, weak disorder, and electron-electron and electron-phonon interactions. These introduce various characteristic length scales:

- Thermal length scale $L_T = \hbar v_F \beta/\pi$ with v_F the Fermi velocity and $\beta = 1/k_B T$. This represents the characteristic length over which the electron diffuses in the time scale corresponding to the thermal broadening of the Fermi distribution function $\hbar\beta$.

- Elastic mean free path l with respect to impurity scattering. It is the distance covered by an electron before losing its initial direction by impurity collisions. "Elastic" means that the energy is conserved during the process.
- Phase-coherence length l_ϕ, which takes into account inelastic processes. It is the scale over which an electron stays in a particular eigenstate and its phase coherence is maintained.

There are many methods developed to study quantum transport in mesoscopic systems. The scattering approach, which is explained in detail in App. A, is simple and elegant. We can solve with this approach a great variety of problems with great accuracy. In this thesis we use this approach in Chapter 2, 3 and 4. Another method widely used to treat interactions is the Green's function formalism. In Chapter 5 we explain this framework in more detail.

We now discuss a few representative nanostructures relevant to this thesis.

1.3.1 Graphene

Graphene is a monolayer of carbon atoms arranged in a two-dimensional honeycomb lattice, see Fig. 1.5. Theoretically, graphene has been studied during more than seventy years with the objective of analyzing its electric properties [29]. It was believed that all the bidimensional crystals were thermodinamically unstable and, for this reason, free graphene was believed to be a material impossible to grow. However, in 2004, the group of A. Geim and K. Novoselov was able to synthesize graphene layers and characterize its properties [30, 31]. Since then this material has caused an enormous interest in the scientific community [32–34].

Let us summarize the main properties of a single layer of graphene. First, graphene is a two-dimensional structure and as a result, electrons are strongly confined in the perpendicular direction. Then, electric conduction takes place only in the plane.

Graphene has four valence electrons, three of which form tight bonds with neighboring atoms in the plane. Their wave functions

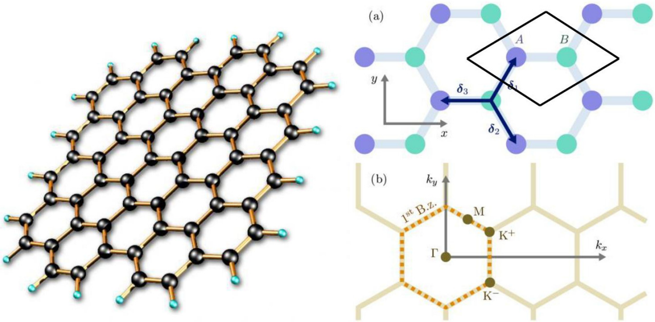

Figure 1.5: Left: Honeycomb structure in a two-dimensional graphene layer. Right: (a) Unit cell is shown as a rhombus; (b) first Brillouin zone and the two nonequivalent valleys, K^+ and K^-.

have the following form

$$\frac{1}{\sqrt{3}}\left(\psi_c(2s) + \sqrt{2}\psi_c(\sigma_i 2p)\right), \tag{1.1}$$

where $\psi_c(2s)$ is the $(2s)$ wave function for carbon and $\psi_c(\sigma_i 2p)$ are the $(2p)$ wave functions whose axes are in the direction σ_i with $i = 1, 2, 3$. In graphene the orbitals are sp^2-hybridized. This means that the orbitals $2p_x$ and $2p_y$, which lie in the graphene plane, mix with the $2s$ orbital to form three sp^2-hybrid orbitals. The different carbon atoms bind together via these three sp^2-hybrid orbitals forming σ-bonds in the plane. For this reason, these three localized electrons will not contribute to the conductivity. Only the fourth electron, which is free and occupies the $2p_z$ state (perpendicular to the plane), can contribute to the transport. When the $2p_z$ orbitals of the adjacent atoms in graphene overlap, they form π-bonds, leading to the π-band. Electronic states close to the Fermi level are described well by a model taking into account only the $2p_z$ orbitals. This is the main ingredient of the tight-binding model [see Eq. (1.6) below], in which there is only one electron per atomic site in a $2p_z$ state. The tight-binding model considers that the atomic orbitals remain intact because the atoms in the lattice are weakly interacting [35].

As stated before, the graphene structure is organized in a honeycomb lattice with carbon atoms in the hexagonal points. The unit cell is a rhombus (two equilateral triangles) that contains two carbon atoms. This is the reason why we have two sublattices A and B (see Fig. 1.5). The lattice vectors can be written as

$$\mathbf{a}_1 = \frac{a}{2}(3, \sqrt{3})\,, \quad \mathbf{a}_2 = \frac{a}{2}(3, -\sqrt{3})\,, \tag{1.2}$$

where $a \approx 1.42$ Å is the carbon-carbon distance and both vectors start from an atom of the sublattice A. The reciprocal lattice can be described from the first Brillouin zone (BZ), an hexagon with only two points that are not equal by symmetry, K^+ and K^-, see Fig. 1.5. The reciprocal-lattice vectors are

$$\mathbf{b}_1 = \frac{2\pi}{3a}(1, \sqrt{3})\,, \quad \mathbf{b}_2 = \frac{2\pi}{3a}(1, -\sqrt{3})\,. \tag{1.3}$$

The position of carbon atoms at the sublattice A is determined by the position vector $\mathbf{R}_A = n_1\mathbf{a}_1 + n_2\mathbf{a}_2$. In the same way, the position of carbon atoms at the sublattice B is given by the position vector $\mathbf{R}_B = n_1\mathbf{a}_1 + n_2\mathbf{a}_2 + \boldsymbol{\delta}_1$, where

$$\boldsymbol{\delta}_1 = \frac{a}{2}(1, \sqrt{3})\,, \quad \boldsymbol{\delta}_2 = \frac{a}{2}(1, -\sqrt{3})\,, \quad \boldsymbol{\delta}_3 = -a(1, 0)\,, \tag{1.4}$$

are the positions of the three nearest-neighbors in the real space, see Fig. 1.5.

As mentioned above, the graphene's BZ has two points at the corners that are not equivalent by symmetry. These points are named Dirac points because of the linear dispersion relation [see Eq. (1.9) below] and their positions in momentum space are given by

$$\mathbf{K}^+ = \left(\frac{2\pi}{3a}, \frac{2\pi}{3\sqrt{3}a}\right)\,, \quad \mathbf{K}^- = \left(\frac{2\pi}{3a}, -\frac{2\pi}{3\sqrt{3}a}\right)\,. \tag{1.5}$$

The tight-binding Hamiltonian for electrons in graphene reads [29]

$$H_{TB} = -t \sum_{\langle i,j \rangle, s} \left(a^\dagger_{s,i} b_{s,j} + b^\dagger_{s,j} a_{s,i} \right)\,, \tag{1.6}$$

where we have considered that the electrons can only hop to their first neighbors with hopping energy $t \approx 2.8$ eV. These hopping occur between sublattices because, as we can see in Figure 1.5, each atom is surrounded by atoms of the other sublattice. In this relation $a_{s,i}(a^\dagger_{s,i})$

annihilates (creates) an electron with spin s on site $\mathbf{R}_i$ of sublattice A. For $b_{s,j}(b^\dagger_{s,j})$ we follow the same definition but for the sublattice B.

The Bloch wave function can be built from a linear combination of atomic orbitals

$$\Psi^{\text{Bloch}}_{\mathbf{k}}(\mathbf{r}) = \frac{1}{\sqrt{N}} \sum_{\mathbf{R}} e^{i\mathbf{k}\mathbf{R}} \left[A\phi(\mathbf{r}-\mathbf{R}_A) + B\phi(\mathbf{r}-\mathbf{R}_B) \right] , \quad (1.7)$$

where $\mathbf{R} \equiv \mathbf{R}_A = \mathbf{R}_B - \boldsymbol{\delta}_1$ and A and B are unknown amplitudes. N is the number of lattice sites in the crystal and $\phi(\mathbf{r})$ describes the wave function of a p_z-orbital in a sp^2-hybridized carbon atom, as discussed above.

Solving the eigenvalue problem using the Schrödinger equation $H_{TB}\Psi^{\text{Bloch}} = E\Psi^{\text{Bloch}}$ we obtain the following dispersion relation [36, 37],

$$E_\pm(\mathbf{k}) = \pm t \sqrt{3 + 4\cos\left(\frac{3ak_x}{2}\right)\cos\left(\frac{\sqrt{3}ak_y}{2}\right) + 2\cos^2\left(\sqrt{3}ak_y\right)} \, , \quad (1.8)$$

where (k_x,k_y) are the momentum in the x- and y-direction respectively and the positive (negative) sign indicates conduction (valence) band.

If we plot Eq. (1.8) we obtain Fig. 1.6. We observe that near the K-points the gap between the conduction and valence bands is zero. This is the region in which we are interested since at low energies the dispersion relation can be simplified. If we make an expansion around one of the Dirac points [36], $\mathbf{k} = \mathbf{K}^+ + \mathbf{q}$ with $|\mathbf{q}| \ll |\mathbf{K}^+|$, we obtain

$$E_\pm(\mathbf{q}) = \pm\hbar v_F |\mathbf{q}| \, , \quad (1.9)$$

where $\mathbf{q}$ is the total momentum measured with respect to the Dirac points and v_F is the Fermi velocity which is given by $v_F = 3ta/(2\hbar) \simeq 1 \times 10^6$ m/s. A similar spectrum is obtained around $\mathbf{K}^-$.Here, at low energies, the electrons behave as massless fermions traveling at fixed velocity v_F. This is the main difference with respect to the electron free gas relation dispersion, $E_\pm = \hbar^2 q^2/(2m)$, where m is the electron effective mass, in which case the electron velocity, $v = \hbar q/m = \sqrt{2E/m}$, depends on energy [29]. The second difference is that Eq. (1.9) is linear with the total momentum.

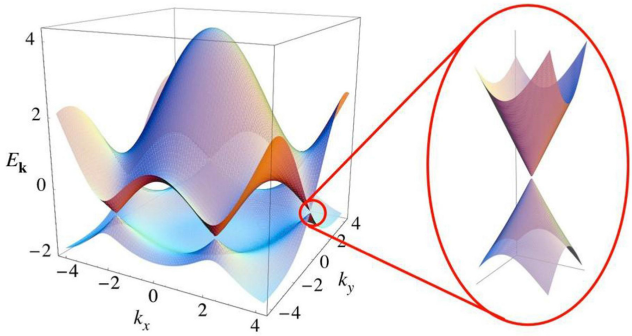

Figure 1.6: Graphene band structure. Reproduced from Ref. [29]

The next step is to find an effective Hamiltonian around the Dirac points. To do this we consider Eq. (1.6) and the following Fourier transform of the electron operators,

$$a_i = \frac{1}{\sqrt{N_c}} \sum_{\mathbf{k}} e^{-i\mathbf{k}\cdot\mathbf{R}_i} a(\mathbf{k}) \,, \tag{1.10}$$

where N_c is the number of unit cells. Using this transformation we can write the operator a_n as a sum of two new operators that result from Fourier expanding the sum around the two Dirac points, K^+ and K^-. This new way to represent the operator a_n can be written as

$$a_i \simeq e^{-i\mathbf{K}^+\cdot\mathbf{R}_i} a_1 + e^{-i\mathbf{K}^-\cdot\mathbf{R}_i} a_2 \,, \tag{1.11}$$

$$b_j \simeq e^{-i\mathbf{K}^+\cdot\mathbf{R}_j} b_1 + e^{-i\mathbf{K}^-\cdot\mathbf{R}_j} b_2 \,, \tag{1.12}$$

where the subindex 1(2) refers to the $\mathbf{K}^+(\mathbf{K}^-)$ point. These new fields are assumed to vary slowly over the unit cell. Now, using this representation in the tight-binding Hamiltonian, Eq. (1.6), and expanding the operators up to linear order in $\boldsymbol{\delta}$ we find the graphene Hamiltonian close to the Dirac points [38]. In the derivation, one uses the fact that $\sum_\delta e^{\pm i\mathbf{K}^+\cdot\boldsymbol{\delta}} = \sum_\delta e^{\pm i\mathbf{K}^-\cdot\boldsymbol{\delta}} = 0$. After some straightforward algebra we obtain

$$H \simeq -i\hbar v_F \int dx\, dy \left(\psi_1^\dagger(\mathbf{r})\boldsymbol{\sigma}\cdot\boldsymbol{\nabla}\psi_1(\mathbf{r}) + \psi_2^\dagger(\mathbf{r})\boldsymbol{\sigma}^*\cdot\boldsymbol{\nabla}\psi_2(\mathbf{r}) \right) \,, \tag{1.13}$$

where $\boldsymbol{\sigma} = (\sigma_x, \sigma_y)$, $\boldsymbol{\sigma}^* = (\sigma_x, -\sigma_y)$ and $\psi_n = (a_n, b_n)$ with $n = 1, 2$. We obtain that the effective Hamiltonian given by Eq. (1.13) consists of two copies of the massless Dirac-like Hamiltonian, one around K^+ and the other one around K^-. Then, close to the K^+ point, we infer that the two-component electron wavefunction $\psi_1(\mathbf{r})$ obeys an effective 2D Dirac equation

$$-i\hbar v_F \boldsymbol{\sigma} \cdot \boldsymbol{\nabla} \psi_1(\mathbf{r}) = E\psi_1(\mathbf{r})\,. \tag{1.14}$$

Then, the effective Hamiltonian near the K^+ point reads

$$H = v_F \boldsymbol{\sigma} \cdot \mathbf{k}\,, \tag{1.15}$$

where $\mathbf{k} = -i\hbar\boldsymbol{\nabla}$ and $\boldsymbol{\sigma}$ describes the pseudospin, i.e., gives the amplitude in the different places of the two sublattices.

Rashba spin-orbit interaction in graphene

The spin-orbit interaction is responsible for the coupling between the electron's spin and orbital degree of freedom. The interaction originates from a relativistic effect which can be derived from Dirac's model of the electron. In heavy ions the mixing is large. However, as we know, graphene is made of carbon atoms and these are light. Then, the intrinsic spin-orbit interaction is expected to be weak in graphene monolayers [39, 40].

The spin-orbit interaction of the Rashba type, which is the focus of this thesis book, arises from the breaking of the inversion symmetry of the honeycomb lattice. This breaking arises when an external electric field ($\mathcal{E}$) is applied perpendicular to the graphene monolayer or by interaction with a substrate. Recent works suggest large spin-orbit strengths in graphene layers under the influence of metallic substrates [41–46]. This finding is interesting in view of recent studies that relate spin-orbit coupling of the Rashba type [47, 48] to topological insulating behavior [49, 50]. Importantly, the Rashba coupling strength can be externally tuned by modifying the electric field applied to a nearby gate [51]. This type of interaction leads to band splittings and enriched spintronic effects [52, 53].

To obtain the Rashba Hamiltonian we have to take into account the intra-atomic spin-orbit coupling (SOC) Hamiltonian given by

$$H_{SO} = \xi\, \mathbf{L} \cdot \mathbf{S}\,, \tag{1.16}$$

where **S** is the Pauli matrix vector that represents the real spin, **L** the angular momentum operator and ξ the intra-atomic SOC strength [54, 55]. Expressed Eq. (1.16) in second quantization language, the SOC exists only among the $2p$ orbitals [39]. To obtain the Rashba term, we also have to consider the Hamiltonian corresponding to the perpendicular electric field: $H_{\mathcal{E}} = e\mathcal{E}z$. This represents an atomic single-particle Stark effect and couples s-orbitals with p_z-orbitals within the same atom.

Now, using a second order perturbation theory, we obtain, at leading order in ξ, the Rashba term [39, 40, 55]

$$H_R^{\text{graphene}} = \lambda(\sigma_x \otimes s_y - \sigma_y \otimes s_x)\,, \tag{1.17}$$

where the electron spin and pseudospin (sublattice) degrees of freedom are taken into account with the Pauli s and σ matrices, respectively. The interaction strength is given by λ [49] which depends linearly with the electic field and the SOC strength [39]. We take λ as a slowly varying function in a length scale larger than the graphene lattice constant. Thus, the continuum model we consider remains valid.

Combining Eq. (1.15), including the spin degree of freedom, and Eq. (1.17) we obtain the total Hamiltonian of a graphene monolayer in the x-y plane with the presence of a Rashba spin-orbit interaction.

$$\mathcal{H} = -i\hbar v_F(\sigma_x \partial/\partial x + \sigma_y \partial/\partial y) \otimes s_o + \lambda(\sigma_x \otimes s_y - \sigma_y \otimes s_x)\,. \tag{1.18}$$

We now make a change of notation. Let k (q) be the wavevector component along the x- (y-) direction. Then, the eigenenergies are given by

$$E_{l,n} = l\sqrt{\lambda^2 + \hbar^2 v_F^2(k^2 + q^2)} + n\lambda\,, \tag{1.19}$$

where $l = \pm$ labels states with positive or negative energies and $n = \pm$ is the subband index. For $\lambda = 0$ we recover the Eq. (1.9) which, in this new notation, can be written as

$$E_l = l\hbar v_F \sqrt{k^2 + q^2}\,. \tag{1.20}$$

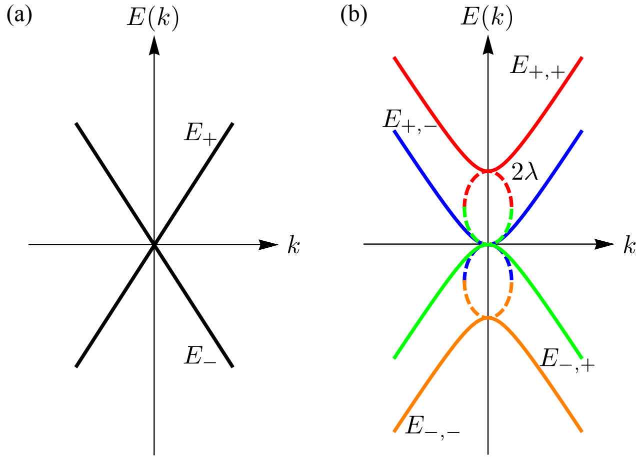

Figure 1.7: Sketch of the energy bandstructure of a graphene layer without (a) and with (b) spin-orbit interaction of the Rashba type. Solid lines indicate propagating states while dashed lines depict the energy associated to evanescent states.

The band structure for bare graphene and $q = 0$ is plotted in Fig. 1.7(a) (projection of band structure of Fig. 1.6 for $k_y = 0$). We observe two branches, one for positive energies (E_+) and another one for negative energies (E_-). As we can observe, there is no gap between the conduction and valence band and the energies are spin degenerate.

The energy spectrum for a finite value of the spin-orbit strength λ and $q = 0$ is plotted with solid lines in Fig. 1.7(b). Here we can see how the energy bands split with a splitting given by 2λ for both the positive and negative branches of the spectrum. The labels and the difference between solid and dashed lines will be clarified in Chapter 2.

1.3.2 Semiconductor heterostructures

The fundamental properties of semiconductors are determined by their band structure. At zero temperature the valence band is completely filled and the conduction band is completely empty. They also exhibit a band gap that separates the conduction and valence bands while the Fermi energy level, E_F, lies in the middle.

The most important reason why semiconductors are ideal materials for the implementation of nanodevices is due to the possibility of changing their electronic properties via doping. Doping is achieved by introducing very small amounts of atoms with a number of valence electrons different from those found in the pure crystal. With this process we can, for example, improve the conductivity.

The band structure of a perfect semiconductor can be analyzed by solving the Schrödinger's equation. In the single-particle picture, electrons are noninteracting but feel the presence of the periodic potential of the crystal lattice.

$$\left[-\frac{\hbar^2}{2m}\Delta + V(\mathbf{r})\right]\psi(\mathbf{r}) = E\psi(\mathbf{r})\,, \tag{1.21}$$

where the potential $V(\mathbf{r}) = V(\mathbf{r}+\mathbf{R})$ has the period $\mathbf{R}$, a translation vector. Moreover, m is the free electron mass and E defines the band structure.

The most relevant parts of the band structure in semiconductor nanostructures are close to the lowest minimum of the conduction band or close to maxima of the valence band. The best way to calculate the band structure close to these points is by using the method known as $\mathbf{k}\cdot\mathbf{p}$ perturbation theory.

We will use the following wavefunction that satisfies the Bloch's theorem,

$$\psi_{n\mathbf{k}}(\mathbf{r}) = \sum_{\mathbf{k}} e^{i\mathbf{k}\cdot\mathbf{r}} u_{n\mathbf{k}}(\mathbf{r})\,, \tag{1.22}$$

with

$$u_{n\mathbf{k}}(\mathbf{r}) = \sum_{\mathbf{G}} c_{\mathbf{k}-\mathbf{G}} e^{-i\mathbf{G}\cdot\mathbf{r}}\,, \tag{1.23}$$

where $u_{n\mathbf{k}}(\mathbf{r}) = u_{n\mathbf{k}}(\mathbf{r}+\mathbf{R})$ fulfills periodic boundary conditions at the boundaries of the primitive cell and the subindex n labels different bands.

Inserting Eq. (1.22) into Eq. (1.21) we obtain,

$$\left\{\left[\frac{\mathbf{p}^2}{2m} + V(\mathbf{r})\right] + \left[\frac{\hbar}{m}\mathbf{k}\cdot\mathbf{p} + \frac{\hbar^2 k^2}{2m})\right]\right\} u_{n\mathbf{k}}(\mathbf{r}) = E_n u_{n\mathbf{k}}(\mathbf{r})\,, \tag{1.24}$$

where $\mathbf{p} = -i\hbar\nabla$ is the momentum operator. Now we assume that we can solve Eq. (1.24) for the special case $\mathbf{k} = 0$ and find the energies

E_n. These energies correspond to functions $u_{n0}(\mathbf{r}) \equiv |n\rangle$ which form a complete set of states. Then, we can use these functions to expand $u_{n\mathbf{k}}(\mathbf{r})$ for arbitrary $\mathbf{k}$

$$u_{n\mathbf{k}}(\mathbf{r}) = \sum_n c_n(\mathbf{k}) u_{n0}(\mathbf{r}) \,. \tag{1.25}$$

Finally, introducing this expansion into Eq. (1.24) we obtain the equations that determine the coefficients $c_n(\mathbf{k})$:

$$\sum_n \left[\left(E_n + \frac{\hbar^2 k^2}{2m} \right) \delta_{n,n'} + \frac{\hbar}{m} \mathbf{k} \cdot \left\langle n' | \mathbf{p} | n \right\rangle \right] c_n(\mathbf{k}) = E c_{n'}(\mathbf{k}) \,. \tag{1.26}$$

Now we apply the $\mathbf{k} \cdot \mathbf{p}$ perturbation theory. When $|\mathbf{k}|$ is small we can treat the $\mathbf{k}$-dependence in Eq. (1.26) as a perturbation and calculate the eigenvalues using perturbation theory. As we shall see, there will be no terms linear in $\mathbf{k}$ at the band extrema indicating that the corrections of E_n (the solution for $\mathbf{k} = 0$) vanish to first order. In contrast, for nondegenerate E_n, we obtain the following expression

$$E_n(\mathbf{k}) = E_n + \frac{\hbar^2 k^2}{2m} + \frac{\hbar^2}{m^2} \sum_{n', n' \neq n} \frac{|\mathbf{k} \cdot \mathbf{p}_{n'n}|^2}{E_n - E'_n} \,, \tag{1.27}$$

which has second order corrections. The last term of Eq. (1.27) can be simplified considerably if we take into account that many of the matrix elements $\mathbf{p}_{n'n}$ nullify. Now, we can join the two last terms and write

$$E_n(\mathbf{k}) = E_n + \frac{\hbar^2 k^2}{2m^*} \,, \tag{1.28}$$

where m^* is an effective mass which includes the band structure details. As we can see, the dispersion relation takes the same form as for free electrons. However, the curvature of the parabola is modified by m^*.

Once we understand a pure crystal, let us see what happens if the periodic lattice potential is perturbed. This perturbation can occur because of the presence of lattice defects, impurities, or doping atoms. Additionally, other sources of perturbations are due to the interfaces between different materials, external electric or magnetic fields. Here, we will restrict ourselves to small static perturbations with a spatial range much larger that the lattice constant of the material, i.e., weak and long-range perturbations. In this way, we can treat these perturbations to the lowest order in perturbation theory. We will use Bloch states to solve the problem and focus on a perturbation of a parabolic conduction band with minimum at Γ.

The Schrödinger equation takes the following form

$$[H_0 + U(\mathbf{r})]\Psi(\mathbf{r}) = E\Psi(\mathbf{r})\,, \tag{1.29}$$

where H_0 is the unperturbed Hamiltonian, Eq. (1.21), which we know how to treat. The dispersion relation is $E_n(\mathbf{k})$, Eq. (1.28), and the Bloch functions are $\psi_{n\mathbf{k}}(\mathbf{r}) = e^{i\mathbf{k}\cdot\mathbf{r}}u_{n\mathbf{k}}(\mathbf{r})$. $U(\mathbf{r})$ is the perturbing potential and the wave function $\Psi(\mathbf{r})$ can be expanded on the basis of Bloch states:

$$\Psi(\mathbf{r}) = \sum_{n,\mathbf{k}} F_n(\mathbf{k})\psi_{n\mathbf{k}}(\mathbf{r})\,. \tag{1.30}$$

If we substitute Eq. (1.30) into Eq. (1.29), multiply by $\psi^*_{n'\mathbf{k}'}(\mathbf{r})$ and integrate over $\mathbf{r}$ we obtain

$$\sum_{n,\mathbf{k}}[(E_n(\mathbf{k}) - E)\delta_{n\mathbf{k},n'\mathbf{k}'} + U_{n'\mathbf{k}',n\mathbf{k}}]F_{n\mathbf{k}} = 0\,, \tag{1.31}$$

where $U_{n'\mathbf{k}',n\mathbf{k}}$ are the matrix elements of the perturbing potential. Using the following assumptions about the perturbation, we can simplify these matrix elements. The first assumption considers that U is relevant only on the scale of the lattice constant, i.e., for momenta much smaller than π/a. The second is related to the magnitude of the perturbation which is taken small compared to typical energy separations of bands in the crystal. The last one gives us information about the coefficients $F_n(\mathbf{k})$, which are significant parameters only for small values of $\mathbf{k}$.

Then, using these approximations we find that $U_{n'\mathbf{k}',n\mathbf{k}} \approx U(\mathbf{k}' - \mathbf{k})\delta_{nn'}$. This indicates that the perturbation does not mix states of different bands. However, it does mix states with different momentum near the band minimum. Introducing this simplification and Eq. (1.28) into Eq. (1.31) and transforming the resulting equation into the real space we arrive at

$$\left[-\frac{\hbar^2}{2m^*}\Delta + E_n + U(\mathbf{r})\right] F_n(\mathbf{r}) = EF_n(\mathbf{r})\,, \tag{1.32}$$

where $F_n(\mathbf{r})$ is a function of long range compared to the lattice period and is termed the envelope function of the wave function. Observing Eq. (1.32) we note that it represents an effective Schrödinger equation [cf. Eq. (1.29)] where the periodic lattice potential $V_{\mathbf{r}}$ included in H_0 has disappeared and, instead, we have replaced the free electron mass with the effective electron mass. The two last terms in the left side of Eq. (1.32) give rise to the local band edge energy, $E_n(\mathbf{r}) = E_n + U(\mathbf{r})$, which acts as an effective potential where the n-band's electrons move.

We have thus far studied the band properties of semiconductors alone. But what happens if we combine different semiconductors in a semiconductor heterostructure? Interestingly, the band structure can be tailored with these structures.

Nowadays, different methods of growing materials with very different composition exist. One of them is by growing atomic layers with molecular beam epitaxy. Using this method we can vary the band structure in the growth direction and adapt it according to the needs of our device. To grow a material on top of each other without creating strain we require that both materials have the same lattice constant and crystal structure. Then, the question is how the band structure is changed at the interface.

The simplest way to answer the above question is to use a theory based on the electron affinities χ_A and χ_B of the two materials A and B to be combined, see Fig. 1.8(a). By definition, the electron affinity is the maximum energy that one can obtain when we add an electron at rest from a region far away from the crystal to an undoped semiconductor. The energy of the electrons far away from the crystal is called the vacuum level and it is the same for the two materials which we want to combine. The electron gains the maximum energy if it is filled into the bottom of the conduction band. Then, at the interface of both materials, the difference of the electron affinities gives the relative position of their conduction band minima. In other words, a step appears in the conduction band edge. This is the conduction band offset, of size $\Delta E_c = |\chi_A - \chi_B|$.

We can distinguish three different types of heterointerfaces depending on the relative position of the conduction and valence band edges is both sites of the interface, see Fig. 1.8(b).

Another way to change the properties of semiconductor materials is by means of the incorporation of relatively small concentrations

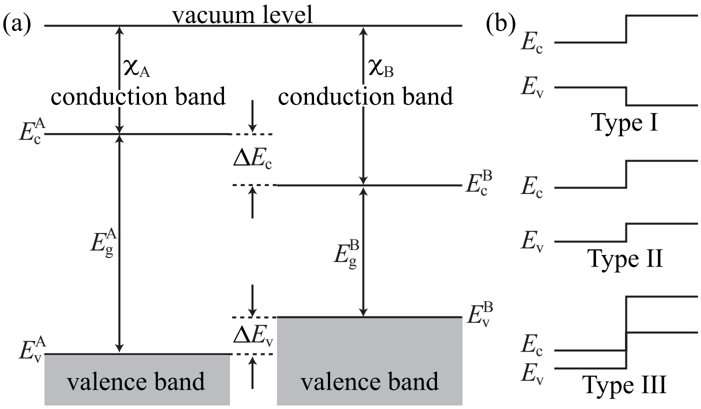

Figure 1.8: (a) Relative position of the band edges at a heterointerface between two materials, A and B. (b) Band line-up of conduction and valence band edges for the three different heterointerfaces. Reproduced from Ref. [37].

of doping atoms on specific lattice sites. There are two big groups of doping atoms: donors and acceptors atoms. The first ones are atoms that have one valence electron more than the atom which they replace. In contrast, the acceptor atoms have one electron less than the atom which they replace. Another characteristic is that this kind of dopants can release electrons (holes) through thermal activation into the conduction band via n-doping (p-doping).

The way how the dopants are distributed is important. For example, in volume doping the dopant atoms are equally distributed in the crystal. In contrast, in the sheet doping or δ-doping technique the dopants are incorporated in a plane. The method in which we are interested is the remote doping. It is a combination of δ-doping and a heterointerface and is the method that is used to generate a two-dimensional electron gas.

1.3.2.1 Two-dimensional Electron Gas

In the remote doping technique, a doped layer is placed at a certain distance from a type I heterointerface, see Fig. 1.9. This doped layer is deposited on the wider band gap material. As we know, the donor electrons (acceptor holes) move to the material with the smaller band gap due to the conduction (valence) band offset. Then, the positively

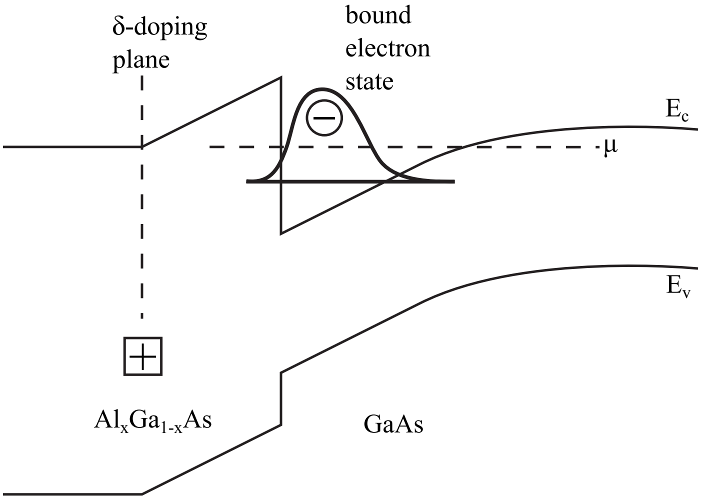

Figure 1.9: Pictorial representation of conduction band edge along the growth direction of type I heterostructure with remote doping. A two-dimensional electron gas forms at the interface. Reproduced from Ref. [37].

charged donors (negatively charged acceptors) and electrons (holes) attract themselves electrostatically and keep the charge carriers close to the interface. Consequently, a two-dimensional electron gas forms. In this kind of systems, the electrons are confined in the normal direction to the interface but are free to move along the interface. Similarly to the quantum well case, in this region quantum confined states exist along the growth direction. Then, the Hamiltonian for these electrons which can move freely in the x and y plane and are strongly confined in the z-direction takes the simple form

$$H = -\frac{\hbar^2}{2m^*}\left(\frac{\partial^2}{\partial x^2} + \frac{\partial^2}{\partial y^2}\right) , \tag{1.33}$$

where m^* is the conduction-band effective mass of the electrons in the 2DEG.

The corresponding eigenvalues take the general form [c.f. Eq. (1.28)]:

$$E = \frac{\hbar^2 \mathcal{K}^2}{2m^*} = \frac{\hbar^2}{2m^*}\left(k^2 + q^2\right) , \tag{1.34}$$

where k and q are the wave numbers along x (longitudinal) and y (transverse) directions, respectively. As we can see, this dispersion relation is parabolic and independent of the electron spin. However, this simple picture can be modified by the spin–orbit interaction and its modifications depend on the particular semiconductor heterostructure where the 2DEG is realized. We can distinguish two kinds of spin–orbit effects: one due to the lack of inversion symmetry of the crystal structure (Dresselhaus term) and the other one due to the confinement potential created by the epitaxially grown structure (Rashba term) which does not show inversion symmetry [48].

In this thesis, we will focus on the Rashba coupling since its strength can be electrically tunable with an external gate. The combined action of the structure inversion asymmetry and the mixture of valence band states to conduction band states results in a net electric field in the z-direction (normal to the 2DEG plane). The strength of this electric field can be modified applying another external electric field E_z in the same direction (e.g. with a capacitively coupled gate). Then, to lowest order in $\mathbf{k}$ we can write the Rashba Hamiltonian (see App. B) as

$$H_R^{\mathrm{2DEG}} = -i\alpha(\sigma_x\partial_y - \sigma_y\partial_x)\,, \tag{1.35}$$

where σ_x and σ_y are the Pauli's spin matrices and α is the Rashba strength which can be separated in a constant part that depends on the 2DEG material and another part which is proportional to the average of the external electric field in the z-direction. The interested reader can find in Ref. [56] a more detailed discussion about how this averaging is performed.

Finally, the dispersion relation given by Eq. (1.34) is modified as follows

$$E_\pm = \frac{\hbar^2\mathcal{K}^2}{2m^*} \pm \alpha\mathcal{K}\,, \tag{1.36}$$

where $\mathcal{K} = \sqrt{k^2+q^2}$ and the signs ± indicate that now we have two branches. In the two-dimensional model, the spin is not a good quantum number and, for this reason, the two branches are not associated with a well defined spin. Only in the one-dimensional case, where the band structure are two parabolas displaced by a quantity $m^*\alpha/\hbar^2$ with respect to the origin, each branch has an associated spin. In

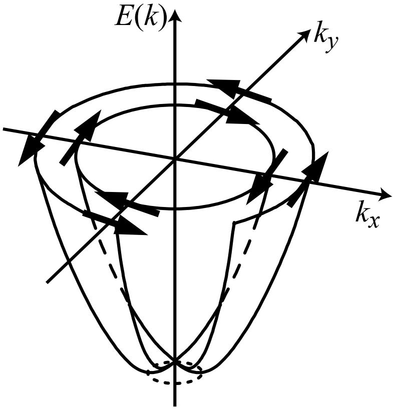

Figure 1.10: Sketch of the energy bandstructure of a 2DEG with spin-orbit interaction of the Rashba type. The arrows on circles of constant energy give the directions of the spin states on each branch. Reproduced from Ref. [56].

Fig. 1.10 we depict Eq. (1.36) and we can observe how at a given energy the direction of the spin state is different for each k, q point. Therefore, the Rashba coupling induces a spin splitting but no net polarization in general.

1.3.2.2 Quantum Point Contact

In order to further confine the electrons one introduces quantum point contacts (QPC). These are formed in a nanoscale short and narrow constriction, with a width of the order of the Fermi wave length ($d \sim \lambda_F$), between two large conducting regions which act as source and drain electrons reservoirs, see Fig. 1.11. A well known method to fabricate QPCs is the split-gate technique where two metallic gate fingers are evaporated on the surface of the wafer leaving a narrow channel in between. When we apply a negative voltage on the gate electrodes, the 2DEG is depleted underneath the gates over a range that depends on the applied gate voltage. Then, a narrow quantum channel for electrons is built on the basis of a 2DEG with tunable width, d. Importantly, when we apply a voltage difference, $eV = \mu_\ell - \mu_r$, between the reservoirs, electrons are forced to pass through the constriction.

In Fig. 1.12(left) we show a schematic of a GaAs/AlGaAs semi-

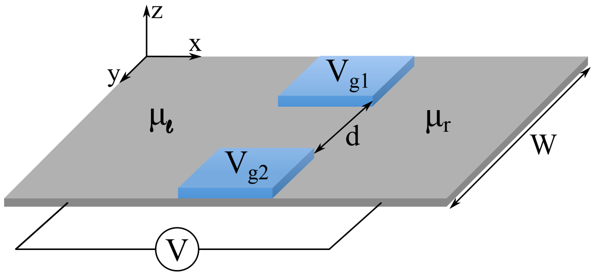

Figure 1.11: Pictorial representation of a QPC which consists of a 2DEG (grey area) with two metal gates (blue areas) deposited on top. The voltage bias V is needed to drive electrons through the constriction. With the gate voltage V_{g1} and V_{g2} we can tune the number of modes active in the QPC. The transversal 2DEG width is given by W while d is the QPC width of the constriction.

conductor heterostructure where the different layers are grown using molecular beam epitaxy. Next, using the split-gate technique, two metal gates (black region) are deposited on the heterostructure surface and a QPC channel is formed by applying a negative voltage to the gates, as indicated in Fig. 1.12(right). Due to the potential felt by the electrons in this region the energy levels will be quantized in the transverse direction.

The resulting system is confined in the z and y direction and is translationally invariant in the x-direction. The system can thus be seen as an electronic waveguide. Then, we can consider the Schrödinger's equation in the x- and y-direction separately and, as a consequence, the total wave function will be written as

$$\Psi_{n\mathbf{k}}(x,y) = \chi_n(y)e^{ikx}\,, \tag{1.37}$$

where we have a plane wave in the longitudinal direction, e^{ikx}, and $\chi_n(y)$ represents the wave function of the one-dimensional modes (labelled by $n = 1, 2\ldots$) in the waveguide. We do not take into account the z-direction because the confinement in the direction perpendicular to the 2DEG plane is much larger and typically only a single energy level is populated.

Finally, the corresponding total energy for the asymptotic modes

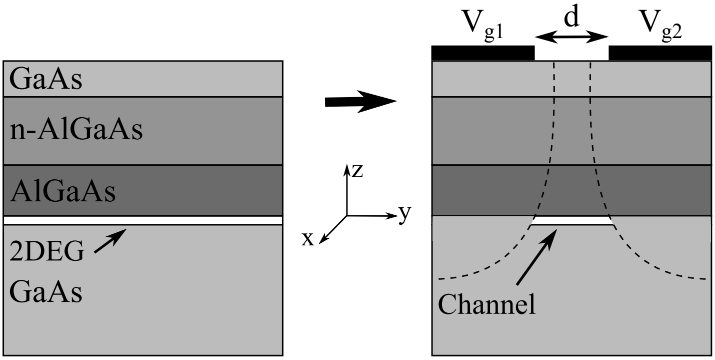

Figure 1.12: Left: Scheme of a GaAs/AlGaAs heterostructure where different material layers are deposited in order to obtain a 2DEG. Right: The same heterostructure with two metal gates on the top. Thus, the 2DEG is confined in the y-direction and a QPC channel thus forms.

is given by

$$E_n(k) = E_n + \frac{\hbar^2 k^2}{2m^*}\,, \tag{1.38}$$

where the second term in the right-hand side is the single-particle kinetic energy for motion along the propagation direction and the first one represents the quantized energy levels in the transversal direction. We assume that the confinement potential can be modelled as an infinite quantum well. Then, $E_n = \hbar^2\pi^2 n^2/(2m^* W^2)$ where W is the width of the waveguide.

The transport properties of our QPC device can be described with the linear conductance, $G = (dI/dV)_{V=0}$. Then, we start from the expression of the current in the scattering approach (see App. A for details):

$$I = \frac{e}{h}\sum_{n=1}^{N}\int_{-\infty}^{\infty} dE\, T_n(E)[f_\ell(E) - f_r(E)]\,, \tag{1.39}$$

where $T_n(E)$ is the transmission probability for one electron to cross the constriction from the left to the right contact in mode n at energy E. $f_c(E) = 1/[1 + e^{(E-\mu_c)/k_B T_c}]$ with $c = \ell, r$ is the electron's Fermi distribution in the reservoirs where T_c and μ_c are the contact temperature and chemical potential. Finally, N is the number of open modes at a given energy in the quasi-one dimensional system and is given by $N = \text{Int}\left[\mathcal{K}_F W/\pi\right]$, where $\mathcal{K}_F = \sqrt{2m^* E_F}/\hbar$.

To obtain the linear conductance we need to apply a small voltage difference between the reservoirs, $V = \mu_\ell - \mu_r$, keeping the same background temperature $T_\ell = T_r = T_0$. Then, we can Taylor expand up to first order in V

$$f_\ell(E) - f_r(E) = -\frac{\partial f(E)}{\partial E} eV\,. \tag{1.40}$$

Inserting this expansion into Eq. (1.39) and performing the energy integration at zero temperature, we obtain

$$I = \frac{e^2}{h} V \sum_{n=1}^{N} T_n(E_F)\,. \tag{1.41}$$

Hence, the linear conductance becomes

$$G = \frac{e^2}{h} \sum_{n=1}^{N} T_n(E_F)\,. \tag{1.42}$$

When the transmission for a given mode n at energy E_F is close to one, this mode contributes with one full conductance quantum (e^2/h) per electron. We have to note that each mode is spin degenerate. This means that each mode can be doubly occupied and it will contribute with conductance $2e^2/h$. Ideally, the transmission for given mode is zero until the mode is open. Then, G in Eq. (1.42) would show perfect quantization $G = \frac{2e^2}{h} N$. Deviations from this quantization can be attributed to temperature, adiabatic openings, quantum tunnelling, etc. [57, 58].

1.3.2.3 Quantum dot

Finally, a full confinement of the electrons is possible using quantum dots (QDs). In the same way as in the fabrication of QPCs, a QD device can be built by evaporating six gate fingers on top of a GaAs/AlGaAs heterostructure, 2DEG, see Fig. 1.13. Then, as in the QPC case, applying a negative voltage on the outer metal gates, the 2DEG is depleted and the electrons will be confined. In Fig. 1.13 we

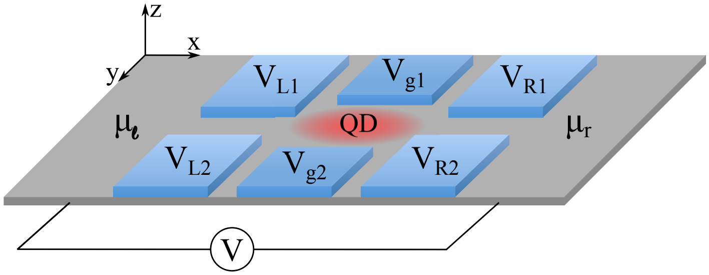

Figure 1.13: Pictorial representation of a QD formed in a 2DEG (grey area) with six metal gates (blue areas) deposited on top. As in the QPC case (Fig. 1.11), the voltage bias V drives electrons through the different constrictions. Applying a negative voltage to the finger gates $V_{L/R1}$ and $V_{L/R2}$ one creates the QD (red area). V_{g1} and V_{g2} are employed to control the position of the quantum dot energy levels.

observe how the separation between the central gate fingers, called plunger gates, is greater than that between the two pairs of exterior gate fingers. Due to this, the electrons can be localized on an island between the gates and the electrons become confined to the three spatial directions, obtaining effectively a 0-dimensional system. With the plunger gates one manipulates the electron density in the region between the outer QPCs. The coupling between the island and the two reservoirs are determined by these two outer pairs of electrodes. This kind of systems acts as an artificial atom with discrete energy states.

Until now we have neglected the role of electron–electron interactions. Nevertheless, in quantum dots the Coulomb interaction is dominant because of their small dimensions, of the order of 100 nm. In Chapter 5 we will focus on the Coulomb blockade effect, which is one of the fundamental transport phenomena in semiconductor nanostructures. This effect is visible only if the Coulomb energy, or charging energy U, is large in comparison with the other energy scales. U is the energy required to add one electron to the dot when the dot is not empty. A classical electrostatic reasoning leads to the expression

$$U = e^2/C\,, \tag{1.43}$$

where $C = 8\varepsilon\varepsilon_0 r$ is the dot self-capacitance. For a dot of radius

$r = 100$ nm fabricated on top of as GaAs heterostructure, relative dielectric constant is $\varepsilon = 13$, the charging energy is $U \sim 1.7$ meV. If we compare U with the mean spacing between successive energy levels

$$\Delta = \frac{\hbar^2}{m^* r^2} \sim 110\ \mu\text{eV}\,, \tag{1.44}$$

where $m^* = 0,067 m_0$ for GaAs (we have used parabolic dispersion relation), we can see that U is one order by magnitude larger than Δ. Then, the Coulomb blockade effect should be observable. More generally, to have $U \gg \Delta$ in GaAs heterostructures, we need a QD with a radius,

$$r \gg \frac{8\varepsilon\varepsilon_0\hbar^2}{m^* e^2} \sim 7\ \text{nm}\,. \tag{1.45}$$

Another important quantity is the temperature, which has to be smaller than the charging energy, $U \gg k_B T$. In order to fulfill this condition we need that the dimensions of the quantum dot should be small since $U \sim 1/r$, or equivalently one should use low temperatures. However, if the temperature is also smaller than the single-particle level spacing, $k_B T < \Delta$, only one quantized energy level contributes to the transport through the QD and this is the regime in which we will work in this thesis. This implies, using the above parameters, that $T < 1$ K.

Finally, if the broadening $\hbar\Gamma$ of the energy levels in the dot due to the coupling to the leads is much smaller than $k_B T$, we can neglect quantum fluctuations and charge is well defined. In other words, only first order tunnelling processes are in this way taken into account.

Once we have defined the regime in which Coulomb blockade effect is observable, we can explain one of its consequences, namely, the conductance resonances as a function of plunger gate voltage. In Fig. 1.14 we show the linear conductance reported in Ref. [59] when a small bias voltage is applied across the quantum dot showed in the left top inset. The linear conductance, and as a consequence the current through the quantum dot, can be controlled with a plunger gate voltage since the gate can tune the quantum mechanical energy states in the quantum dot via capacitive coupling.

In Fig. 1.14 we observe sharp resonances at certain values of V_g. This phenomenon can be explained taking into account that in QDs

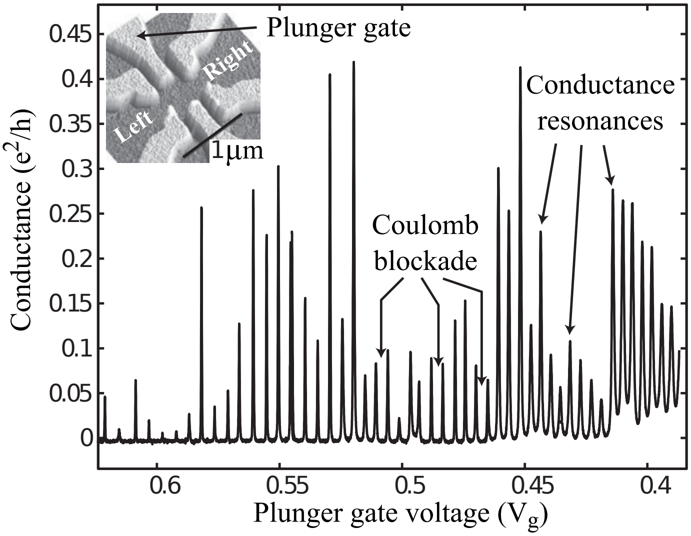

Figure 1.14: Linear conductance as a function of the plunger gate voltage V_g. Inset: Quantum dot fabricated by split-gate technique. Reproduced from Ref. [59]

the electron-electron interaction plays an important role. As discussed above, if a new electron is added into the dot, we have to pay an extra energy U (charging energy). Only when V_g takes an specific value for which the dot electrochemical potential is in resonance with the reservoirs electrochemical potentials, the electron can tunnel through the dot. In contrast, for intermediate values the electrons in the reservoirs do not have enough energy to overcome the Coulomb repulsion and transport is blockaded.

Now, if the voltage between reservoirs is larger, the current present nonlinearities and we can measure the differential conductance, $G_{dc} = dI/dV$, in addition to the linear conductance. The measurements of the differential conductance as a function of V and V_g can be combined to obtain the so-called Coulomb blockade diamonds. In Fig. 1.15 we show these Coulomb blockade diamonds for the simplest model in which there is only one dot energy level, ε_0. Due to the spin degree of freedom, this dot energy level can be occupied by two electrons. However, as we have mentioned before, the energy required for the second

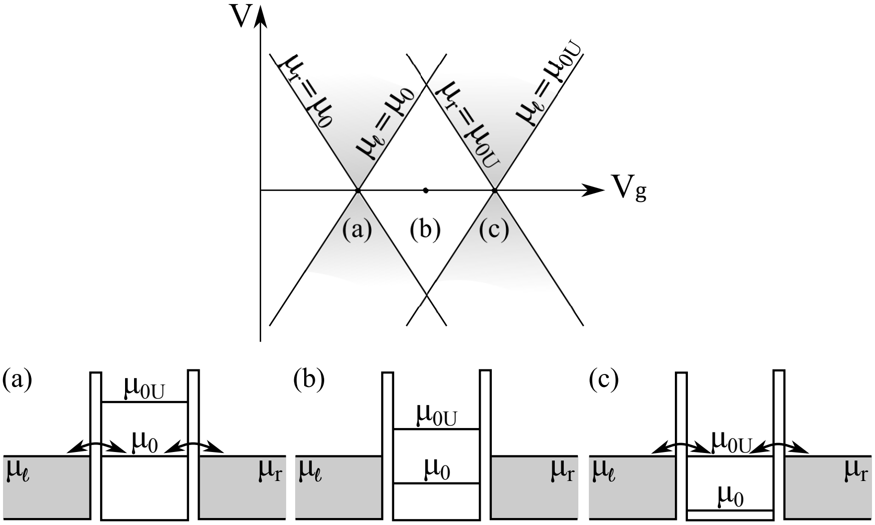

Figure 1.15: Schematic Coulomb blockade diamonds of a single-level quantum dot. The current is only differs from zero in the grey areas. The black lines indicate for which values of V (voltage difference between reservoirs) and V_g (plunger gat voltage) the electrochemical potentials of reservoirs (μ_ℓ and μ_r) and quantum dot (μ_0 and μ_{0U}) are aligned. Insets (a), (b) and (c) represents the energy diagram of the above points in the main panel.

electron to hop into the dot is ε_0+U due to Coulomb repulsion. In the top panel of Fig. 1.15, we show a color plot of the differential conductance as a function of the voltage difference between reservoirs and the plunger gate voltage, where white and grey areas represent respectively zero and finite positive values. Black lines indicate alignment between one of the reservoirs electrochemical potentials, μ_ℓ or μ_r, and one of the dot electrochemical potentials, μ_0 or μ_{0U}. The position of reservoirs and dot electrochemical potentials are modified by V and V_g respectively. The energy diagrams corresponding to points (a) and (b), represented schematically in the insets are the conductance peaks of linear transport ($V = 0$) showed in Fig. 1.14. In between there is a diamond shaped white region where due to the Coulomb blockade effect the electron transport is forbidden. To better understand this phenomenon let us see with more detail the inset in Fig. 1.15(a). μ_ℓ, μ_0 and μ_r are aligned and the electrons can flow through the QD.

However, when we increase V_g the position of μ_0, and consequently μ_{0U}, decreases and the electrons can tunnel on the dot but not off the dot, see Fig. 1.15(b). Subsequently, a second electron can not enter the dot since it has to surpass the Coulomb repulsion and does not have enough energy. This is the Coulomb blockade effect, because transport becomes blockaded due to the Coulomb interaction. If we continue increasing the plunger gate voltage until μ_ℓ, μ_{0U} and μ_r become aligned, the transport is again permitted through the dot, see Fig. 1.15(c).

2. Thermoelectric effects in graphene

In this chapter, we will study the influence of local Rashba spin-orbit interaction on the electric and thermoelectric properties of graphene (see Sec. 1.3.1)[1]. In graphene's systems with an inhomogeneous spin-orbit interaction previous studies have considered Fano lineshapes in graphene junctions [60, 61], spin densities in nanoribbons [62] and superlattice [63], spin dependent transmissions [64] and Klein (chiral) tunneling [65]. Here, we are mainly concerned with the voltages generated in response to a temperature difference (the Seebeck effect) [35] (see Sec. 1.2). Interestingly, recent results indicate enhanced thermopower in graphene monoloyers [66–68], which paves the way for promising applications to achieve efficient heat-to-energy converters [69]. We here discuss the possibility of manipulating the thermopower with a local spin-orbit interaction. In fact, we find that a spin-orbit graphene monolayer is more sensitive to temperature biases than to voltage differences. Furthermore, since the Rashba coupling splits the graphene electronic bandstructure, the transmission thus depends on the subband index. In analogy with spin caloritronic devices [22], where a thermal gradient induces a spin-polarized voltage bias [15, 24], we propose to use the Seebeck effect to generate a difference between occupations with different subband indices.

2.1 Theoretical model

We consider a graphene layer in the xy plane with spatially varying spin-orbit interaction along the x-direction, see Figure 2.1. Within the

---

[1] The contents of this chapter are based on M. I. Alomar and David Sánchez, Phys. Rev. B **89**, 115422 (2014) and M. I. Alomar and David Sánchez, in *Dynamical Systems, Differential Equations and Applications*, AIMS Proceedings, pp. 1–9 (2015).

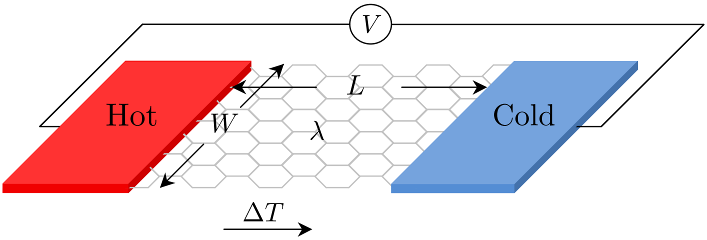

Figure 2.1: Pictorial representation of a graphene layer with a central region of length L under the influence of a spin-orbit interaction of the Rashba type. The system is invariant along the y-direction (width W). Electronic transport is induced along the x-direction with a bias voltage V applied to nearby contacts or with a temperature difference ΔT between hot and cold terminals.

continuum limit, the total Hamiltonian is given by Eq. (1.18) where the spin-orbit coupling strength takes a constant value in each region: 0 for $x < 0$ and $x > L$ and λ for $0 < x < L$. As we have mentioned in Sec. 1.3.1, this model is valid when inter-valley scattering can be safely neglected.

The energy spectrum is showed in Fig. 2.2 where in the central region, $0 < x < L$, we have plotted the dispersion relation given by Eq. (1.19) for a finite value of the spin-orbit strength λ and $q = 0$. Here, the energy bands become parabolic for energies small compared to the spin-orbit strength. In contrast, the energy spectra in the contacts, $x < 0$ and $x > L$, is given by Eq. (1.20) which is linear with a constant slope.

The eigenstates of Eq. (1.18) are

$$\Psi_{l,n}^{m}(x) = \frac{e^{imkx}e^{iqy}/2}{\sqrt{\hbar^2 v_F^2(k^2+q^2)+E_{l,n}^2}} \begin{pmatrix} -in\hbar v_F(mk-iq) \\ E_{l,n} \\ -inE_{l,n} \\ \hbar v_F(mk+iq) \end{pmatrix}, \quad (2.1)$$

where we explicitly indicate the propagation direction with the aid of the index $m = \pm$, which determines the sign of the momentum along x. Since the scattering potential is invariant in the y-direction we take q as a real quantity. However, the k momentum can be real or

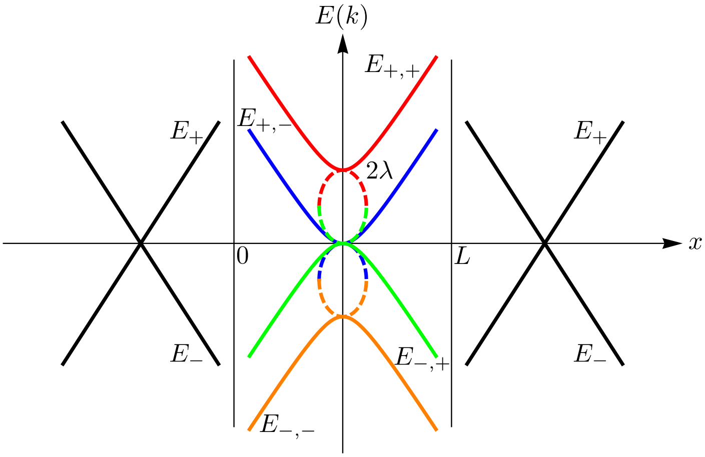

Figure 2.2: Pictorial representation of a graphene layer with a central region of length L where spin-orbit interaction is active. We take x as the propagation direction. We show the energy spectra both inside and outside the central region. Solid lines indicate propagating states while dashed lines depict the energy associated to evanescent states.

purely imaginary depending on whether one deals with traveling or evanescent waves. A systematic method of finding evanescent states in quantum wires with Rashba interaction is presented in Ref. [70]. Here, we notice that the energy of evanescent waves emerges from the subband spectra and coalesces for $E = \pm\lambda$ (see the dashed lines in Fig. 2.2).

In the absence of spin-orbit interaction the eigenstates take the following form

$$\Psi^m_{l,n}(x,y) = \frac{e^{imkx}e^{iqy}}{2}\begin{pmatrix} -inme^{-im\phi} \\ l \\ -inl \\ me^{im\phi} \end{pmatrix}, \tag{2.2}$$

where ϕ is the wavevector angle defined as $\phi = \tan^{-1} q/k$. Therefore, the states given by Eq. (2.1) [Eq. (2.2)] will be appropriate for $0 < x < L$ ($x < 0$ and $x > L$).

2.2 Wave matching method

We investigate the scattering problem sketched in Fig. 2.2 with three distinct regions. While the side regions (left and right) are bare graphene, the central region of length L is subjected to spin-orbit interaction of the Rashba type. Since the problem is invariant in the direction perpendicular to x, the y-component of the momentum does not change and we can write it in terms of the wavevector angle,

$$q = \frac{E}{\hbar v_F} \sin\phi \,. \tag{2.3}$$

We consider electrons with fixed energy $E > 0$. From Eqs. (1.20) and (2.3), we obtain the wavevector component parallel to the transport direction,

$$k = E\sqrt{(1 - \sin^2\phi)}/\hbar v_F \,, \tag{2.4}$$

valid for $x < 0$ and $x > L$. For $0 < x < L$, k can be determined from Eqs. (1.19) and (2.3):

$$k_n = \sqrt{E(E - 2n\lambda - E\sin^2\phi)}/\hbar v_F \,. \tag{2.5}$$

In the central region, we have two possible values for k_n, one for subband with $n = +$ and one for subband with $n = -$, although a more careful analysis is needed in terms of the subband index. First, we notice that, in general, for any energy, the momentum is always real if $E - 2n\lambda - E\sin^2\phi > 0$, i.e.,

$$\sin\phi < \sqrt{\frac{E - 2n\lambda}{E}} \,. \tag{2.6}$$

Now, for $E > 0$ and $n = -$, Eq. (2.6) is always satisfied since $\sin\phi$ is bounded between 0 and 1. In contrast, for $n = +$ we have a critical angle at which the momentum becomes pure imaginary. For angles higher than the critical angle we have an evanescent wave. Then, for $0 < E < 2\lambda$ and $n = +$ the momentum becomes pure imaginary since Eq. (2.6) is never satisfied and the wave is evanescent for any value of the angle ϕ. Similar critical angles have been invoked to discuss total internal reflection effects in semiconductor interfaces with spin-orbit interaction [71].

We are now in a position to solve the scattering problem in Fig. 2.2. We focus on the case $E > 0$ since our system exhibits particle-hole symmetry, even in the presence of Rashba coupling. Therefore, we take $l = +1$. We consider a most simple inhomogeneity, namely, $\lambda = 0$ for $x < 0$ and $x > L$, and λ nonzero and uniform for $0 < x < L$. This is not contradictory with the assumption that λ is a slowly varying function in an atomic level because the scale over which this change takes place is much bigger than the graphene lattice constant. The matching method allows us to calculate all reflection and transmission amplitudes for a given electron, which we take as impinging from the left. In the following, we express the wave function at each region as $\Psi^m_{+,n}(x,y) = \psi^m_n e^{imkx} e^{iqy}$ where k and q are the x and y moment's module. We first specify left (ℓ) wave function for $x < 0$:

$$\Psi^{(\ell)}_n(x,y) = \psi^+_n e^{ikx} e^{iqy} + r_{-,n}\psi^-_- e^{-ikx} e^{iqy} + r_{+,n}\psi^-_+ e^{-ikx} e^{iqy}\,, \quad (2.7)$$

where the incident subband n can be taken as $+$ or $-$. The reflection amplitudes $r_{-,n}$ and $r_{+,n}$ describe back scattering into $-$ and $+$ modes, respectively. Then, we have an incident wave with positive group velocity, $v = k > 0$, and two reflected waves with $v = -k < 0$, the latter belonging to the doubly degenerate E_+ branch in Fig. 2.2.

In the central (c) region we have four coexisting waves,

$$\Psi^{(c)}_n(x,y) = a_{-,n}\psi^+_- e^{ik_-x} e^{iqy} + b_{+,n}\psi^+_+ e^{ik_+x} e^{iqy} + c_{-,n}\psi^-_- e^{-ik_-x} e^{iqy} + d_{+,n}\psi^-_+ e^{-ik_+x} e^{iqy}\,, \quad (2.8)$$

where the coefficients a, b, c, and d are labeled with the incident subband n and the wavevector with the index $\pm$ defined in Eq. (2.5). Note that the propagating or evanescent character of the partial waves is determined by the real or imaginary value of $k_\pm$. Equation (2.8) is valid for $E > \lambda$, but for $0 < E < \lambda$ we need to take into account the evanescent states taking ψ^+_+ and ψ^-_+ for $l = -1$.

Finally, in the right (r) region we only have transmitted waves with positive group velocity and positive and negative n:

$$\Psi^{(r)}_n(x,y) = t_{-,n}\psi^+_- e^{ikx} e^{iqy} + t_{+,n}\psi^+_+ e^{ikx} e^{iqy}\,, \quad (2.9)$$

where $t_{\pm,n}$ denotes the transmission amplitude from the n-th incident subband toward the $\pm$ mode.

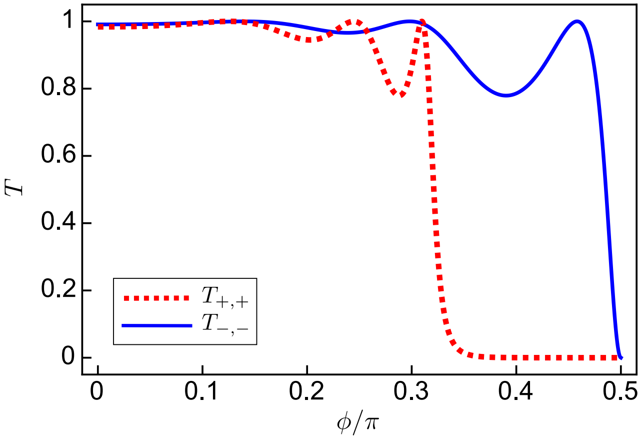

Figure 2.3: Transmission probability as a function of the incident angle ϕ for $E > 2\lambda$. The dotted curve represents the trasmision from $n = +$ to $n = +$ and the solid curve the trasmision from $n = -$ to $n = -$. Parameters: $\lambda = 10$ meV, $E = 80$ meV and $L = 100$ nm.

At the boundaries $x = 0$ and $x = L$ we impose continuity of the wave function,

$$\Psi_n^{(\ell)}(0, y) = \Psi_n^{(c)}(0, y)\,, \tag{2.10}$$

$$\Psi_n^{(c)}(L, y) = \Psi_n^{(r)}(L, y)\,, \tag{2.11}$$

from which the eight coefficients $r_{\pm,n}$, $a_{-,n}$, $b_{+,n}$, $c_{-,n}$, $d_{+,n}$ and $t_{\pm,n}$ are determined.

In elastic scattering, the probability current is conserved. Since our system shows scattering along x only, the current conservation condition is obtained from $J_x^{(\ell)} = J_x^{(r)}$ with $J_x = v_F \Psi^\dagger \sigma_x \Psi$ (see App. C) and leads to

$$1 = R_{+,n} + R_{-,n} + T_{+,n} + T_{-,n}\,, \tag{2.12}$$

where $R_{\pm,n} = |r_{\pm,n}|^2$ ($T_{\pm,n} = |t_{\pm,n}|^2$) is the reflection (transmission) probability. Due to the spin-chiral nature of the carriers [63], the off-diagonal probabilities $T_{+,-}$ and $T_{-,+}$, vanish altogether and the spin-orbit interaction does not couple states with opposite subband indices. Figure 2.3 shows $T_{+,+}$ and $T_{-,-}$ for $E > 2\lambda$ as a function of the incident angle. At low angles ($\phi \simeq 0$) the transmission is close to unity. This is a manifestation of Klein tunneling in graphene for incident wave vectors parallel to the transport direction [72]. When ϕ rotates from 0, the transmission departs from 1 due to scattering at the boundaries. The situation is akin to a single-barrier potential [72] but in our case the effect originates from a purely spin-orbit field.

Interestingly, in Fig. 2.3 we can see the emergence of a critical angle for $T_{+,+}$ beyond which the transmission probability vanishes (dotted line). It occurs because when we surpass the critical angle given by Eq. (2.6), the wave into the central region becomes evanescent and the transmission drops. The transition is not abrupt since there are tunneling contributions to $T_{+,+}$ but this effect is very weak. Note that $T_{-,-}$ (solid line) does not show any critical angle, as predicted by Eq. (2.6). Additionally, we also observe in Fig. 2.3 transmission resonances which we attribute to central waves interfering constructively for specific values of the incident angles.

2.3 Electric Conductance

Within the scattering approach (see App. A) the electric current carried by electrons in subband n is obtained from the transmission probabilities integrated over the injecting energies E and the wave vector angle ϕ,

$$I_n = \frac{2eW}{\pi h} \int_0^{\pi/2} \cos\phi \, d\phi \int_{-\infty}^{\infty} T_{n,n}(E,\phi)\, \mathcal{K}(E) \times [f_\ell(E) - f_r(E)]\, dE\,, \quad (2.13)$$

where W is the sample width in the y direction and $f_c(E)$ with $c = \ell, r$ are Fermi-Dirac distribution functions that describe the electronic population in the left and right side, asymptotically far from the scattering (central) region, as defined after Eq. (1.39):

$$f_c(E) = \frac{1}{1 + e^{(E-\mu_c)/k_B T_c}}\,, \quad (2.14)$$

where $\mu_c = E_F + eV_c$ is the contact electrochemical potential with V_c a small voltage bias and $T_c = T_0 + \theta_c$ the contact temperature with θ_c a small temperature. The 2 factor in Eq. (2.13) is due to the valley degeneracy and $\mathcal{K}(E) = E/\hbar v_F$ is obtained from the graphene dispersion relation, Eq. (1.20). We also note that we do not need a

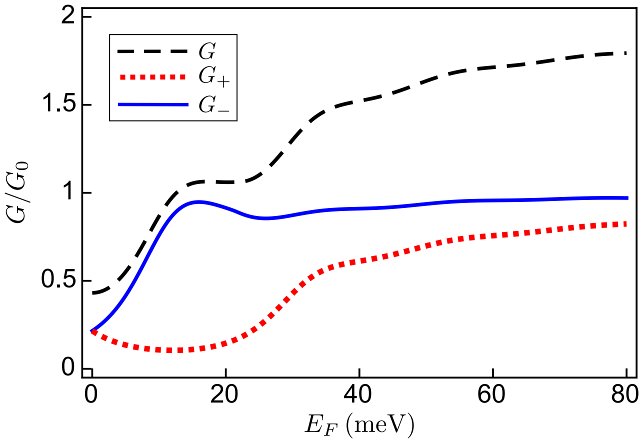

Figure 2.4: Conductance as a function of Fermi energy. Parameters: $\lambda = 10$ meV and $L = 100$ nm.

sum over the transmitted subband index n' because the off-diagonal probabilities transmissions are zero. The total current is thus $I = \sum_n I_n$.

To obtain the linear conductance $G = (dI/dV)_{V=0}$, a small voltage bias is applied across the junction, $\theta_r = \theta_\ell = 0$, $V_r = 0$ and $V_\ell = V$. Then, we shift the left Fermi-Dirac distribution $f_\ell = f(E - eV)$ fixing the right one $f_r = f(E)$ where $f(E) = 1/[1 + e^{(E-E_F)/k_B T_0}]$ is the equilibrium Fermi distribution function. After Taylor expanding Eq. (2.13) up to first order in V, we obtain

$$I_n = \frac{2e^2 W V}{h\pi} \int_0^{\pi/2} \cos\phi \, d\phi \int_{-\infty}^{\infty} T_{n,n}(E,\phi)\, \mathcal{K}(E) \left(-\frac{\partial f}{\partial E}\right) dE \,. \tag{2.15}$$

At zero temperature we find $G = \sum_n G_n$, where

$$G_n = G_0 \int_0^{\pi/2} T_{n,n}(E_F,\phi) \cos\phi \, d\phi \,, \tag{2.16}$$

and $G_0 = 2e^2 W \mathcal{K}_F/\pi h = 4e^2 W E_F/h^2 v_F$ is the maximum conductance of an ideal two-dimensional conductor since $\mathrm{Int}\,(W\mathcal{K}_F/\pi)$ is the number of open channels of a sample with Fermi wave number $\mathcal{K}_F = \mathcal{K}(E_F)$ (see Sec.1.3.2.2 and Ref. [73]).

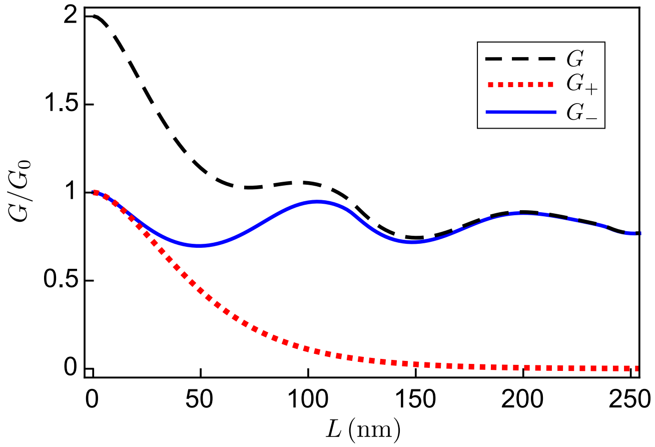

Figure 2.5: Conductance as a function of L. Parameters: $E_F = 15\,\mathrm{meV}$ and $\lambda = 10\,\mathrm{meV}$.

Figure 2.4 shows the conductance as a function of E_F. We choose the Fermi energy as the changing parameter since it can be easily tuned in an experimental setup [30]. The conductance G_+ (dotted line) is small for energies between 0 and 2λ. This is because in this energy range electrons from subband + can be transmitted only via conventional tunnelling effect due to the center energy splitting. The transmission probability is thus small. For E_F higher than 2λ, G_+ increases since travelling waves are now permitted in the central region. However, the increase is slow due to the persistence of the critical angle above which the transmission probability is zero. The conductance for the $-$ subband (G_-) is always close to the maximal value G_0 because for this mode there always exists a travelling wave in the central region. In general, the total conductance $G = G_+ + G_-$ (dashed line) is a monotonically increasing function of the Fermi energy and tends to $2G_0$ at large energies where spin-orbit scattering is less efficient.

The transmission probability, and therefore the conductance, depends on the length of the central region, L, and the parameter of the Rashba coupling, λ. Then, in Fig. 2.5 we show the electric conductance, G, as a function of L for a fixed Fermi energy. We find that both G_+ and the G_- are trivially equal to unity if $L = 0$ because the

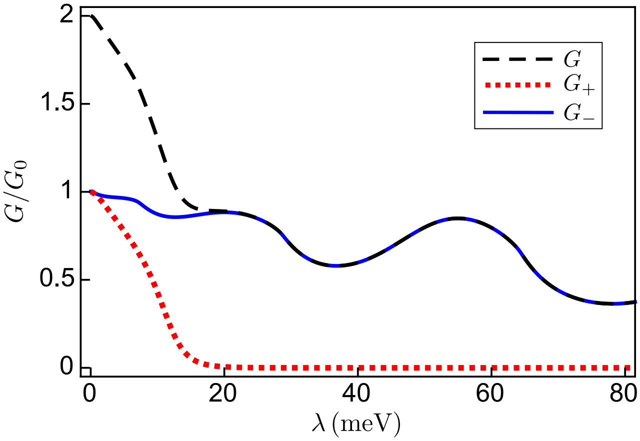

Figure 2.6: Conductance as a function of λ. Parameters: $E_F = 30\,\text{meV}$ and $L = 100\,\text{nm}$.

wave is completely transmitted. When L increases, we observe that G_+ decreases quickly. This is due to the fact that we are considering the case $E_F < 2\lambda$, for which the states in the central region are evanescent (see red dashed line in Fig. 2.2). The transmitted part is due to electron tunneling, with a probability that quickly decreases as L increases and becomes negligible for long spin-orbit regions. On the contrary, the electric conductance with negative subband index, G_-, is always close to unity since the wave functions corresponding to $E_{+,-}$ (see blue solid line in Fig. 2.2) are propagating states for any incident energy $E > 0$. Our conclusion is reinforced by the oscillations seen in G_-, which typically arise in scattering problems with wave interference even for energies above the potential threshold.

In Fig. 2.6 we represent G as a function of λ for a fixed Fermi energy and observe a similar behavior but in this case the nonzero part of G_+ is mainly due to states with $E_F > 2\lambda$, which are propagating. The transition is not abrupt since, although the states for $E_F < 2\lambda$ are evanescent, they also contribute to transmission via tunneling. Independently of the value of λ the conductance term G_- is close to one because there always exists an available channel for any $\lambda > 0$.

Clearly, our results show that by tuning the Fermi energy, the spin-orbit region length or coupling strength, a subband polarization

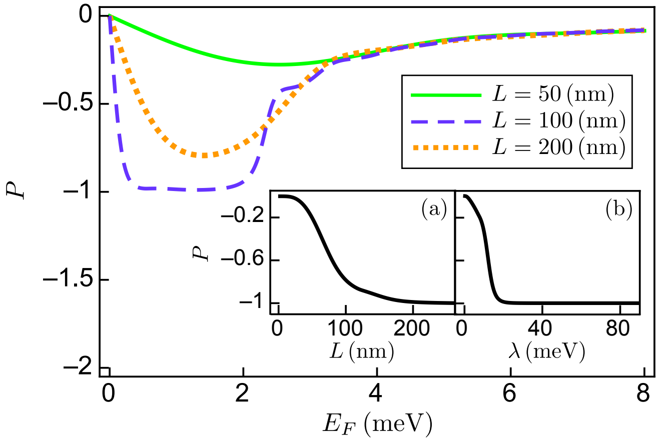

Figure 2.7: Subband polarization of the conductance as a function of Fermi energy for $\lambda = 10$ meV and different values of the spin-orbit region length. The subband polarization of the conductance as a function of L and λ is plotted in the insets (a) and (b) respectively. Parameters inset (a): $E_F = 15\,\text{meV}$ and $\lambda = 10\,\text{meV}$. Parameters inset (b): $E_F = 30\,\text{meV}$ and $L = 100\,\text{nm}$.

of the outgoing electronic states can be achieved for certain values of E_F, L or λ. To quantify this effect, we define the subband polarization as

$$P = \frac{G_+ - G_-}{G_+ + G_-} \,. \tag{2.17}$$

In Fig. 2.7 we represent the subband polarization as a function of E_F. Here, we can see that for $\lambda < E_F < 2\lambda$ most of the electrons have negative polarization because for those energies the wave with positive n becomes evanescent inside the central region and the transmission probability is very small. This effect is more visible for wider regions of the spin-orbit stripe. As we increase the Fermi energy, there are more electrons with positive polarization since for $E_F > 2\lambda$ the states with $n = +$ are travelling waves and their transmission probability is larger. Clearly, in the limit $E_F \gg \lambda$ electron scattering is insensitive to the spin-orbit potential and the distinction between $+$ and $-$ subbands vanishes, yielding $P \to 0$.

If we now plot P as a function of L, we obtain the inset in

Fig. 2.7(a). It shows that at low L the electron wave is unpolarized because the tunneling probability is close to one for small L. As we increase the width of the central region, less waves with $n = +$ are transmitted and the outgoing wave is negatively polarized. Figure 2.7(b) presents the subband polarization as a function of Rashba coupling strength for fixed E_F and L. When λ is small the outgoing wave is not polarized because we have propagating states for each subband index ($E_F > 2\lambda$ in Fig. 2.2). As we increase λ the states with positive n becomes evanescent inside the central region and the transmission probability is vanishingly small. Thus, for $E_F < 2\lambda$ most electrons have negative polarization.

2.4 Thermoelectric conductance

The current generated in the linear regime in response to a small temperature difference applied across the junction can be obtained from Eq. (2.13) taking $V_r = V_\ell = 0$, $\theta_r = 0$ and $\theta_\ell = \Delta T$, see Eq. (2.14):

$$\begin{aligned} I_n = \frac{2eW}{h\pi}\frac{\Delta T}{T_0}\int_0^{\pi/2}\cos\phi\, d\phi \int_{-\infty}^{\infty} T_{n,n}(E,\phi) \\ \times \mathcal{K}(E)(E-E_F)\left(-\frac{\partial f}{\partial E}\right) dE\,. \quad (2.18) \end{aligned}$$

We are interested in the low temperature regime. Then, to leading order in a Sommerfeld expansion, the thermoelectric conductance reads $\mathcal{L} = I/\Delta T = \sum_n \mathcal{L}_n$, where

$$\begin{aligned} \mathcal{L}_n = \mathcal{L}_0 \Bigg(\int_0^{\pi/2} T_{n,n}(E_F,\phi)\cos\phi\, d\phi \\ + E_F \frac{\partial}{\partial E_F}\int_0^{\pi/2} T_{n,n}(E_F,\phi)\cos\phi\, d\phi \Bigg)\,, \quad (2.19) \end{aligned}$$

where $\mathcal{L}_0 = k_B^2 eWT_0/3\hbar^2 v_F$.

In Fig. 2.8, we represent the thermoelectric conductance as a function of the Fermi energy. Surprisingly, we observe strongly modulated oscillations with a decreasing amplitude as we increase E_F. This implies that the thermocurrent is more sensitive than the electric current

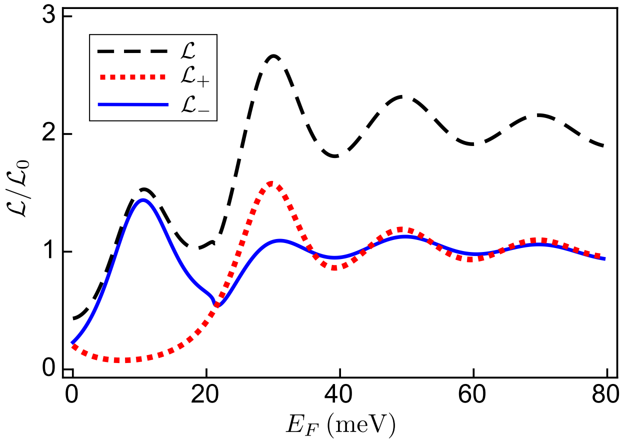

Figure 2.8: Thermoelectric conductance as a function of Fermi energy. Parameters: $\lambda = 10$ meV and $L = 100$ nm.

to small variations of E_F. Furthermore, we find that the position difference between consecutive peaks in $\mathcal{L}$ is approximately given by the spin-orbit strength λ. Therefore, thermoelectric measurements can be rather useful in the detection of local spin-orbit fields in graphene single layers.

In Fig. 2.9 we show the thermoelectric conductance as a function of L for fixed Fermi energy and Rashba strength. At zero L we find that the two components of $\mathcal{L}$ are close to unity since all electrons are transmitted. For larger L, $\mathcal{L}_+$ slowly decreases to zero. The effect is similar to the conductance discussed above: for $E < 2\lambda$ the states with $n = +$ are transmitted solely by conventional tunneling. As expected, the thermoelectric conductance with $n = -$ is larger because the states with $n = -$ are propagating but we also observe a strong variation with the central region length. $\mathcal{L}(\lambda)$, see Fig. 2.10, shows a strong dependence with the value of the Rashba strength. Interestingly, when we increase λ sufficiently we can even obtain a negative thermoelectric conductance for a fixed L and E_F. This means that for those high values of the Rashba strength electrons will travel from the cold to the hot side. These strong variations are a consequence of the dependence of $\mathcal{L}$ on the transmission derivative [see second term in the right-hand side of Eq. (2.19)] unlike the conductance, which depends on the transmission only.

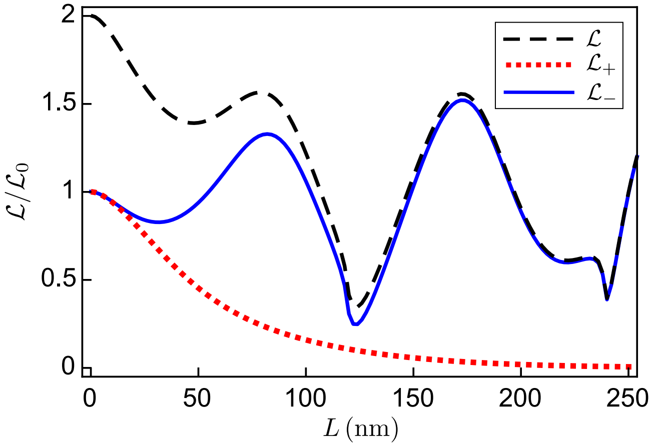

Figure 2.9: Thermoelectric conductance as a function of L. Parameters: $E_F = 15\,\mathrm{meV}$ and $\lambda = 10\,\mathrm{meV}$.

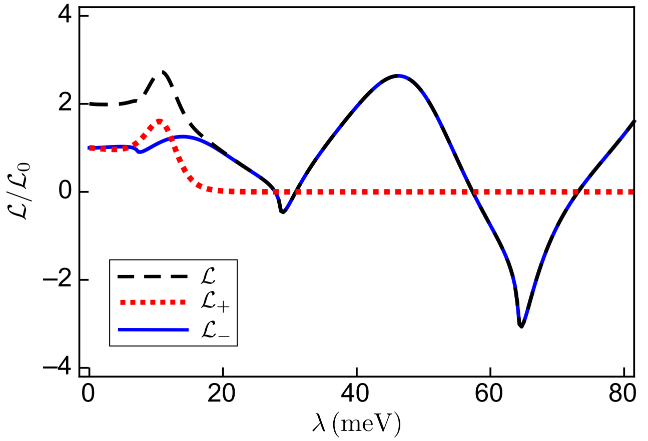

Figure 2.10: Thermoelectric conductance as a function of λ. Parameters: $E_F = 30\,\mathrm{meV}$ and $L = 100\,\mathrm{nm}$.

2.5 Seebeck effect

By virtue of the Seebeck effect, we expect that a thermovoltage will be generated when the junction is in the presence of a temperature gradient under open circuit conditions (see Sec. 1.2). To keep our discussion general, we consider different electrochemical potentials $\mu_{cn} = E_F + eV_{cn}$ for each subband, where $c = \ell, r$. Both sides of the junction are maintained at different temperatures, T_c, independently of n. Then, the current flowing in the n mode in response to small shifts $\mu_{\ell n} - \mu_{rn}$ and $T_\ell - T_r$ at low temperature is

$$I_n = \frac{\mu_{\ell n} - \mu_{rn}}{e} G_n + (T_\ell - T_r)\mathcal{L}_n \,, \tag{2.20}$$

where the transport coefficients G_n and $\mathcal{L}_n$ are given by Eqs. (2.16) and (2.19), respectively.

We define [74]:

$$\Delta T = T_\ell - T_r \tag{2.21a}$$

$$\mu_c = \frac{1}{2}(\mu_{c+} + \mu_{c-}) \tag{2.21b}$$

$$eV = \mu_\ell - \mu_r \tag{2.21c}$$

$$eV_\mathcal{S} = (\mu_{\ell+} - \mu_{\ell-}) - (\mu_{r+} - \mu_{r-}) \,, \tag{2.21d}$$

where ΔT is the temperature difference, V the bias voltage and $V_\mathcal{S}$ the subband voltage that takes into account possible voltage differences in the same lead between different subbands [75]. Using Eqs. (2.21) in Eq. (2.20), we find the total current $I \equiv I_+ + I_-$,

$$I = (G_+ + G_-)V + \frac{1}{2}(G_+ - G_-)V_\mathcal{S} + (\mathcal{L}_+ + \mathcal{L}_-)\Delta T \,, \tag{2.22}$$

and the subband current $I_\mathcal{S} \equiv I_+ - I_-$,

$$I_\mathcal{S} = (G_+ - G_-)V + \frac{1}{2}(G_+ + G_-)V_\mathcal{S} + (\mathcal{L}_+ - \mathcal{L}_-)\Delta T \,. \tag{2.23}$$

We note that $I_\mathcal{S}$ is a polarization current in the subband space. It then plays the role analogous to a spin or pseudospin current since n can take on two values only.

In Eqs. (2.22) and (2.23), the transport coefficients are given by Eqs. (2.16) and (2.19). We define $\mathcal{T}_n$ as the the subband transmission summed over all transverse momenta. Since we consider transport along the longitudinal (x) direction, we include the projection factor $\cos\phi$,

$$\mathcal{T}_n(E_F) = 2\int_0^{\pi/2} T_{n,n}(E_F,\phi)\cos\phi\, d\phi\,. \tag{2.24}$$

We do not include the sum over the transmitted subbands since, as we have mentioned earlier, the off-diagonal transmissions are zero.

Then, Eqs. (2.16) and (2.19) can be recast in the form

$$G_n = \left(\frac{e}{\pi\hbar}\right)^2 \frac{WE_F}{2v_F}\mathcal{T}_n(E_F)\,, \tag{2.25a}$$

$$\mathcal{L}_n = \frac{ek_B^2}{3\hbar^2}\frac{WT_0}{2v_F}\left(\mathcal{T}_n(E_F) + E_F\frac{\partial\mathcal{T}_n}{\partial E_F}\right)\,, \tag{2.25b}$$

where $\partial\mathcal{T}_n/\partial E_F$ is the energy derivative of $\mathcal{T}_n$ evaluated at E_F.

Interestingly, the low-temperature conductance is given by the integrated transmission, in agreement with the Landauer picture of transport, but the thermoelectric conductance contains an additional term. This can be seen more clearly in the calculation of the charge thermopower or Seebeck coefficient $S = (V/\Delta T)_{I=0,I_S=0}$, which determines the voltage generated in the junction in response to a temperature shift when both total and subband currents are set to zero. From Eqs. (2.22) and (2.23) we find

$$S = -\frac{1}{2}\left(\frac{\mathcal{L}_+}{G_+} + \frac{\mathcal{L}_-}{G_-}\right)\,. \tag{2.26}$$

Inserting Eqs. (2.25) in Eq. (2.26), we obtain the low-temperature thermopower

$$S = -S_0\frac{k_BT_0\pi^2}{6E_F}\left(1 + E_F\sum_n\frac{\partial\mathcal{T}_n/\partial E_F}{\mathcal{T}_n(E_F)}\right)\,, \tag{2.27}$$

where $S_0 = k_B/e$.

We notice two contributions in Eq. (2.27). The second term in brackets is the transport term S_{tr}. It is a single-particle result which is satisfied in low dimensional systems such as quantum dots [76] and quantum point contacts [77, 78], for which a sizable thermopower is detected only if the transmission strongly depends on energy. It is thus a pure transport contribution. However, Eq. (2.27) shows an additional term which is insensitive to transmission modulations, the intrinsic term S_{in}. In fact, for a constant transmission probability or when $\mathcal{T}_n$ shows a weak variation with energy on the scale of E_F, Eq. (2.27) reduces to

$$S \simeq -\frac{\pi^2 k_B}{6e}\frac{k_B T_0}{E_F} = S_{in}\,. \tag{2.28}$$

This intrinsic contribution is independent of the sample details and, more importantly, survives in the purely ballistic limit. It simply states that in the highly degenerate limit ($E_F \gg T_0$, i.e., the range of validity of the Sommerfeld approximation), the thermopower is given by the entropy per unit charge (k_B/e) associated to the fraction of the electron density which is thermally excited ($k_B T_0/E_F$). Therefore, Eq. (2.28) is completely general and does not depend on the nature of the scattering potential. For $E_F = 1$ meV and $T_0 = 1$ K, a typical value for the intrinsic thermopower yields $S = 10$ μV/K, a value detectable with present techniques [67].

Using the G_n function defined in Eqs. (2.25a) we can rewrite Eq. (2.28) as a Mott-like formula,

$$S = -S_0 \frac{k_B T_0 \pi^2}{6} \sum_n \frac{\partial \ln G_n(E_F)}{\partial E_F}\,. \tag{2.29}$$

The difference with the formula discussed in Ref. [79] is that our Eq. (2.29) is valid in the ballistic regime of quantum transport.

We thus expect a competition between the intrinsic and the transport terms in the Seebeck coefficient. We plot S in Fig. 2.11 as a function of E_F for a nonzero value of the Rashba strength. We observe that the junction thermopower is always negative, indicating that when the left side is hotter than the right side, the system generates a negative bias to compensate the excess of thermally activated electrons. Furthermore, S is quite robust to variations of the spin-orbit region size L. This fact can be explained taking into account that at high energies the Rashba interaction is not effective and the transmissions are weak functions of energy, as discussed in Sec. 2.3. Then, the transport contribution to the Seebeck coefficient, $S \propto \partial \ln G/\partial E_F$,

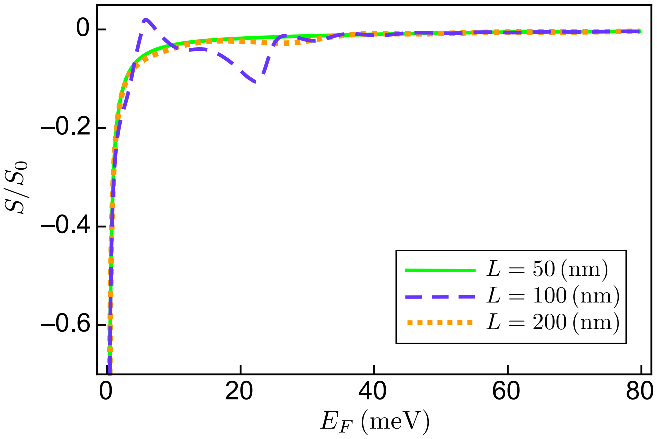

Figure 2.11: Seebeck coefficient as a function of Fermi energy for different values of the spin-orbit region length. Parameters: $\lambda = 10$ meV and $T_0 = 1$ K.

is negligible and S tends to zero as $1/E_F$. In contrast, at low energies the constant term exceeds the transport contribution due to the k_BT_0/E_F term[2]. Therefore, the transport term is relevant only at intermediate energies, as shown in Fig. 2.11.

In Figs. 2.12 and 2.13 we present the Seebeck coefficient as a function of L and λ, respectively. In both cases the intrinsic part of the thermopower is constant since the Fermi energy is a fixed parameter. In Fig. 2.12 we observe that $S(L)$ never changes sign because λ, which controls this effect, is fixed. However, we observe a strong modulation of the thermopower with L, which may serve as a useful tool for tuning S in a graphene layer. In Fig. 2.13 we show $S(\lambda)$, which can now change sign as a function of λ. Therefore, the generated voltage can be tuned with the Rashba strength.

As we have mentioned in Sec. 1.2, applied temperature gradients can also lead to spin accumulations in the attached leads, as recently demonstrated in systems driven by spin Seebeck effects [15, 24]. Then, it is natural to ask whether a local spin-orbit interaction in graphene

---

[2] The $1/E_F$ divergence at very low energies below k_BT_0 is just an artifact of our Sommerfeld expansion, which is exact up to $(k_BT_0/E_F)^4$. Near the charge neutrality point, E_F is of the order of K_BT_0 and the Sommerfeld expansion breaks down.

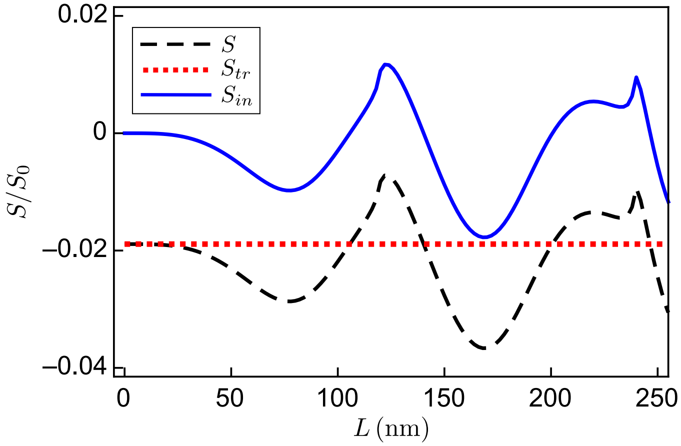

Figure 2.12: Seebeck coefficient as a function of L. Parameters: $E_F = 15\,\text{meV}$, $\lambda = 10\,\text{meV}$ and $T_0 = 1$ K.

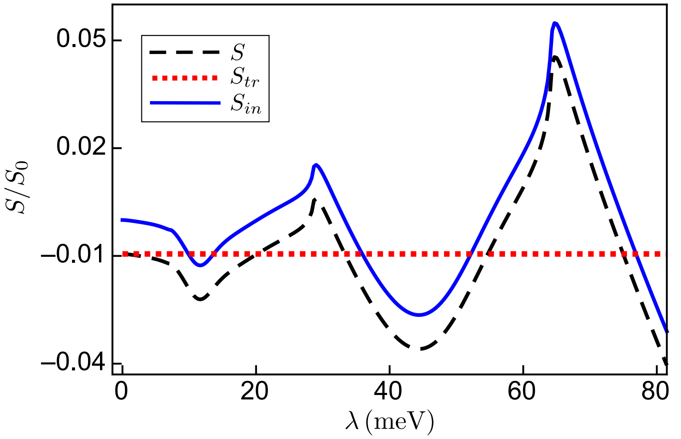

Figure 2.13: Seebeck coefficient as a function of λ. Parameters: $E_F = 30\,\text{meV}$, $L = 100\,\text{nm}$ and $T_0 = 1$ K.

leads to different *subband* populations. We address this question by calculating from Eqs. (2.22) and (2.23) the subband bias $V_{\mathcal{S}}$ generated when $I = 0$ and $I_{\mathcal{S}} = 0$ but $\Delta T \neq 0$. The subband thermopower $S_{\mathcal{S}} = (V_{\mathcal{S}}/\Delta T)_{I=0,I_{\mathcal{S}}=0}$ then follows,

$$S_{\mathcal{S}} = -\left(\frac{\mathcal{L}_+}{G_+} - \frac{\mathcal{L}_-}{G_-}\right) . \tag{2.30}$$

Notice that to obtain this result, we need to apply a bias voltage:

$$V = -\frac{1}{2}\left(\frac{\mathcal{L}_+}{G_+} + \frac{\mathcal{L}_-}{G_-}\right)\Delta T \, . \tag{2.31}$$

At low temperature, we can substitute Eqs. (2.25) in Eq. (2.30), yielding

$$S_{\mathcal{S}} = -S_0 \frac{k_B T_0 \pi^2}{3} \left(\frac{\partial \mathcal{T}_+/\partial E_F}{\mathcal{T}_+} - \frac{\partial \mathcal{T}_-/\partial E_F}{\mathcal{T}_-}\right) , \tag{2.32}$$

where $S_0 = k_B/e$.

Notably, the intrinsic thermopower of Eq. (2.28) drops out from the subband Seebeck coefficient in Eq. (2.32). $S_{\mathcal{S}}$ depends only on the transmission probabilities to cross the spin-orbit region and is thus a purely transport property. Therefore, we expect a stronger energy dependence of the subband thermopower as compared with its charge analog, Eq. (2.27). This is confirmed in our numerical simulations. In Fig. 2.14 we represent $S_{\mathcal{S}}$ as a function of E_F. The energy variation of the subband thermopower becomes more pronounced for wider spin-orbit regions because the subband resolved transmissions differ strongly as the region size enhances. In addition, we observe a sign change of $S_{\mathcal{S}}$, implying that for a positive difference of temperatures a positive or negative subband potential is generated depending on the Fermi energy. As expected, for high energies electrons are insensitive to the Rashba scattering potential and the subband thermopower tends to zero.

2.6 Conclusions

In this chapter we have investigated the thermoelectric properties of a graphene system formed with a junction with a Rashba interaction potential localized around a central region where the spin-orbit

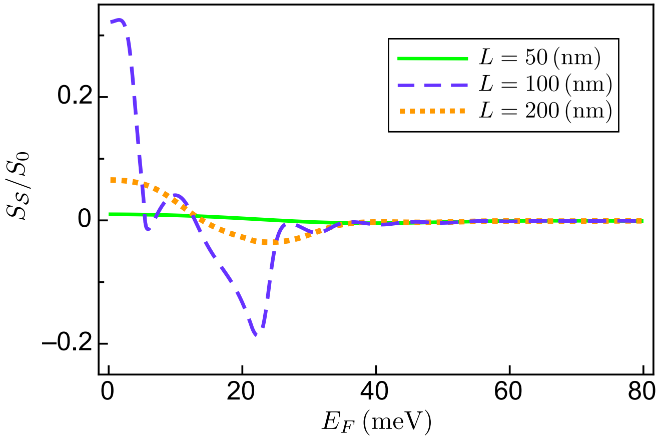

Figure 2.14: Subband-Seebeck coefficient as a function of Fermi energy for different values of the spin-orbit region length. Parameters: $\lambda = 10$ meV and $T_0 = 1$ K.

strength is nonzero and constant. Using matching methods for wave functions with four components, we have found that the transmission probabilities shows, for a given subband index, a critical angle beyond which electrons cannot be transmitted across the junction. We also have calculated the electric conductance and the subband polarization. We have obtained that the polarization rapidly changes in the energy scale of the Rashba strength for sufficiently wide spin-orbit regions. Finally, we have calculated the thermocurrent in response to a small temperature shift and have obtained strong modulations when the Fermi energy is tuned even to values much larger than the spin-orbit strength. Surprisingly, the Seebeck coefficient is a smooth function of energy, an effect which we attribute to a background intrinsic thermopower which is dominant for a wide range of Fermi energies. We then have determined the subband thermovoltage generated in response to a temperature bias and recover the strong variation with energy, yielding positive or negative population imbalances depending on the value of the externally tuned Fermi energy.

Now, in order to determine if these results are similar for a 2DEG based on semiconductor heterostructure we will analyze in Chapter 3 the thermoelectric properties replacing the graphene monolayer with a two-dimensional semiconductor layer. One of the results that we will find is the necessity to introduce ferromagnetic contacts in order to obtain spin Seebeck effect.

3. Seebeck effects in 2D spin transistors

We recall (Sec. 1.2) that an external applied temperature difference can generate a bias voltage (charge Seebeck effect), a spin imbalance (spin Seebeck effect) of a thermovoltage that depends on the magnetization (magneto-Seebeck effect). Our aim in this chapter is to examine these three Seebeck effects in a two-dimensional system (2DES) spin transistor[1]. We consider a quantum well laterally coupled to two ferromagnetic reservoirs kept at different temperatures ΔT, as sketched in Fig. 3.1. Thermocurrent-induced spin polarization effects in Rashba 2DES are discussed in Refs. [80–84] using semiclassical approaches. In the same way as in Chapter 2 we consider the quantum (ballistic) regime of transport and formulate a theoretical model based on the scattering approach. We observe clear oscillations in the charge Seebeck coefficient when the Rashba strength is varied even when the 2DES is coupled to nonmagnetic reservoirs. Importantly, in this case the transmission for up spins and down spins are equal and hence the spin Seebeck coefficient is identically zero. This result agrees with Ref. [84], which finds an absence of thermospin effects in spin-orbit coupled 2DES. However, we below show that spin imbalances can be created in response to temperature differences when the electrodes are ferromagnetic. The effect is more prominent for larger Rashba splittings.

Remarkably, the Seebeck coefficient shows sign changes as a function of the Fermi energy for the case of magnetic leads. This is one of the main findings of this chapter, as it suggests the possibility of controlling the thermoelectric current direction by varying the Fermi energy with a nearby gate. Furthermore, the thermopower depends on the relative orientation of the leads' magnetization. Since the spin-

---

[1] The contents of this chapter are based on M. I. Alomar, Llorenç Serra and David Sánchez, Phys. Rev. B **91**, 075418 (2015).

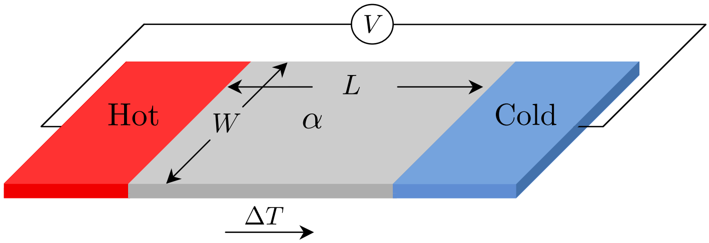

Figure 3.1: Pictorial representation of our system. A two-dimensional semiconductor layer is formed inside a quantum well subjected to a Rashba spin-orbit interaction of strength α. The length of the central region where the Rashba coupling is constant is L (gray area) and W the sample width. Then, α decays smoothly to vanish in the contacts (colored areas). Electronic transport is induced with a bias voltage V which is applied across the junction or with a temperature difference ΔT between the two contacts, hot and cold.

orbit field randomizes the spin direction of current-carrying states, one would expect a quench of the magneto-Seebeck ratio when Rashba interaction is turned on. However, we find significant changes in the presence of spin-orbit coupling.

3.1 Theoretical model

We consider a two-dimensional semiconductor layer in the xy-plane with a central region of width L subjected to a Rashba spin-orbit interaction. This 2DES can be formed with the techniques discussed in Sec. 1.3.2.1. In Fig. 3.1 we show a sketch of our system. The Rashba coupling is spatially varying along the x-direction, which we take as the transport direction. The Hamiltonian reads

$$\mathcal{H} = H_0 - i\left(\alpha(x)\sigma_x\partial_y - \frac{1}{2}\sigma_y\left\{\alpha(x),\partial_x\right\}\right), \tag{3.1}$$

where H_0 is given by Eq. (1.33) and the second term is the Rashba spin-orbit interaction depending on the Pauli matrices σ_x and σ_y, see App.B.

When the Rashba strength $\alpha(x)$ takes a constant value Eq. (3.1) reduces to Eq. (1.35). In the left and the right contacts $\alpha(x)$ is equal to zero while in the central region, of width L, $\alpha(x)$ takes a uniform value $\alpha(x) = \alpha$. In our numerical simulations, the variation of this parameter at the interfaces is almost abrupt with a minor numerical smoothing. We refer the reader to App. D for details of our smoothing model.

The eigenfunctions in the leads are plane waves since the reservoirs are assumed to be metallic with good screening properties. In those asymptotic regions, the band structure takes the general form given by Eq. (1.34).

The transversal q momentum is constant throughout the system since the Hamiltonian of Eq. (3.1) remains invariant after translation along y. Thus, the wave function in the central region can be written in terms of the product of a plane wave in y-direction and an x-dependent amplitude $\psi_{qs}(x)$ for each channel labeled with (q, s). If we sum over spins s and over all the transverse momenta the total wave function reads

$$\Psi(x, y, \eta) = \sum_{s=\pm} \int dq\, \psi_{qs}(x) e^{iqy} \chi_s(\eta)\,, \tag{3.2}$$

where s is a spin index that characterizes the spin function $\chi_s(\eta) \equiv \langle \eta | s \rangle$, with $\eta =\uparrow, \downarrow$ the usual basis of the Pauli matrices.

To determine the channel amplitude equations we project the Schrödinger equation $(\mathcal{H} - E)\Psi = 0$ on a particular channel (q, s),

$$\begin{aligned} &\left(-\frac{\hbar^2}{2m^*}\frac{d^2}{dx^2} + \frac{\hbar^2 q^2}{2m^*} - E \right) \psi_{qs}(x) \\ &+ \sum_{s'=\pm} \left[\left(\alpha(x) q \left\langle s | \sigma_x | s' \right\rangle + \frac{i}{2}\alpha'(x) \left\langle s | \sigma_y | s' \right\rangle \right) \psi_{qs'}(x) \right. \\ &\qquad\qquad \left. + i\, \alpha(x) \left\langle s | \sigma_y | s' \right\rangle \frac{d}{dx}\psi_{qs'}(x) \right] = 0\,. \end{aligned} \tag{3.3}$$

These channel equations show coupling between different spins due to the spin-orbit interaction (the terms $\langle s | \sigma_{x,y} | s' \rangle$). However, channels with different q remain uncoupled due to the translational invariance along y-direction. This is a unique feature of 2DES devices since in quantum wires the coupled channel method does connect adjacent modes with opposite spins [85].

In the contacts, the Rashba coupling vanishes and the wave functions can be expressed with the aid of input $a_{qs}^{(c)}$ and output $b_{qs}^{(c)}$ amplitudes,

$$\psi_{qs}^{(c)}(x) = a_{qs}^{(c)} e^{is_c kx} + b_{qs}^{(c)} e^{-is_c kx}\,, \tag{3.4}$$

where $c = \ell$ ($c = r$) for the left (right) lead and we take $s_\ell = +$ ($s_r = -$). Within scattering theory the output amplitudes are determined from the input ones via reflection $r_{s's}^{(c)}$ and transmission $t_{s's}^{(c)}$ amplitudes,

$$b_{qs'}^{(c)} = \sum_s r_{s's}^{(c)}\, a_{qs}^{(c)} + t_{s's}^{(c)}\, a_{qs}^{(\bar{c})}\,. \tag{3.5}$$

Here, $\bar{c}$ denotes the opposite contact to c. We note that the matrices $t^{(c)}$ and $r^{(c)}$ of Eq. (3.5) depend on q and they are found after discretizing Eq. (3.3) on a grid and imposing the boundary conditions given by Eq. (3.4) with the quantum-transmitting-boundary algorithm [86]. This method gives us a simple and robust way to obtain the reflection and transmission amplitudes since the boundary conditions allow us to rewrite a discretized version of Eq. (3.3) as a tridiagonal system of equations. Due to this, the numerical simulations are very fast.

We define the transmission probabilities

$$T_{s's}(q,E) = \left|t_{s's}^{(r)}\right|^2, \tag{3.6a}$$

$$T'_{s's}(q,E) = \left|t_{s's}^{(\ell)}\right|^2, \tag{3.6b}$$

where $T_{s's}(q,E)$ represents the probability that an incident electron in the left lead with spin s is transmitted to the right lead with spin s'. Analogously, $T'_{s's}(q,E)$ is the transmission probability for an electron injected from the right contact with spin s to arrive at the left contact with spin s'. Figure 3.2 shows the total transmission, $T = \sum_{ss'} T_{s's}$, as a function of the Fermi energy for the case $q = 0$ at fixed α and different lengths of the Rashba region. The $q = 0$ mode is interesting since it corresponds to normal incidence, thus dominating the total transmission as we will demonstrate below.

We observe in Fig. 3.2 that T quickly reaches a maximum and then oscillates. This behavior can be nicely understood from the one-dimensional problem of electrons scattering off a square well where L

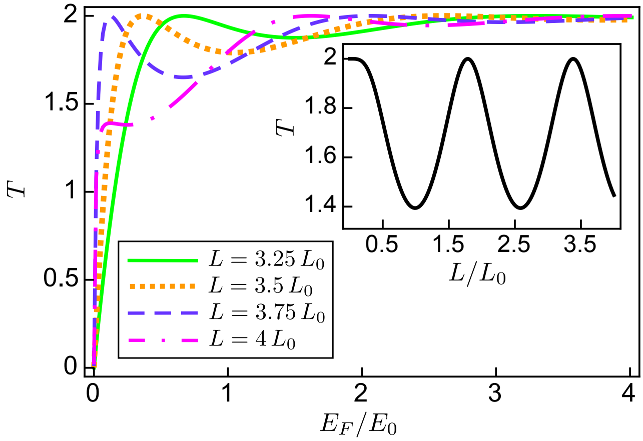

Figure 3.2: Total transmission probability as a function of the Fermi energy for transverse momentum $q = 0$, Rashba coupling $\alpha = 1.7\alpha_0$ and different lengths of the central region L's. Inset: Total transmission probability as a function of L for $q = 0$, $\alpha = 1.7\alpha_0$ and $E_F = 0.5E_0$. We take $L_0 = 60\,\text{nm}$. Hence, $E_0 = \hbar^2/(m^* L_0^2) = 0.92\,\text{meV}$ and $\alpha_0 = \hbar^2/(m^* L_0) = 55.2\,\text{meV nm}$ for $m^* = 0.023 m_e$ as in InAs. For InAs the spin-orbit strength can be as larger as ~ 100 meVnm [56].

is its width and α is proportional to its depth. To see this, we set $q = 0$ in Eq. (3.3),

$$\left(-\frac{\hbar^2}{2m^*}\frac{d^2}{dx^2} - E\right)\psi_{0s}(x) + \frac{i}{2}\alpha'(x)\, s\, \psi_{0s}(x) + i\,\alpha(x)\, s\,\frac{d}{dx}\psi_{0s}(x) = 0\,, \quad (3.7)$$

where we choose the quantization axis of the spin $s = \pm$ in the y-direction. Clearly, the two spins are uncoupled. We now make the gauge transformation

$$\psi_{0s}(x) = e^{is\frac{m^*}{\hbar^2}\int^x \alpha(x')dx'}\,\widetilde{\psi}_{0s}(x)\,. \quad (3.8)$$

Then, Eq. (3.7) is written in terms of $\widetilde{\psi}_{0s}(x)$

$$-\frac{\hbar^2}{2m^*}\widetilde{\psi}''_{0s}(x) + (V_0(x) - E)\,\widetilde{\psi}_{0s}(x) = 0\,, \quad (3.9)$$

where $V_0(x) = -m^*\alpha^2(x)/(2\hbar^2)$. For a piecewise constant $\alpha(x)$, Eq. (3.9) corresponds to the Hamiltonian of a square well of depth $V_0 = m^*\alpha^2/(2\hbar^2)$. We can readily write the total transmission (summed over spins) as [87]

$$T = \frac{2}{1 + \frac{V_0^2}{4E_F(E_F+V_0)} \sin^2\left(L\frac{\sqrt{2m^*(E_F+V_0)}}{\hbar}\right)}, \tag{3.10}$$

where L is the width of the square well (the spin-orbit region length in our case). Then, T is maximum whenever

$$\frac{L}{\hbar}\sqrt{2m^*(E_F + \frac{m^*\alpha^2}{2\hbar^2})} = n\pi\,, \tag{3.11}$$

where $n = 1, 2, \ldots$. The first maximum of T for $E_F > 0$ corresponds to $n = 1$. As we increase the width of the spin-orbit region the first maximum shifts to lower energy, in perfect agreement with Fig. 3.2. The maximum displacement occurs because E_F should decrease to maintain the condition of Eq. (3.11) as L increases. In the inset of Fig. 3.2, we represent the total transmission as a function of L for fixed values of α and E_F. T presents maxima at equidistant values of L. This can also be simply understood from the resonant condition derived from Eq. (3.11).

In Fig. 3.3 we plot T as a function of the Fermi energy for $q = 0$ at fixed length L and different Rashba magnitudes. Similarly to Fig. 3.2, as α increases the first maximum shifts to lower energies. In this case, the analogy with the problem of the square well is based on α, which is proportional to the potential depth. Thus, as we increase the value of α, the Fermi energy should decrease to fulfill the maxima condition of Eq. (3.11). The inset of Fig. 3.3 shows T as a function of α for fixed E_F and L. Notice that the spacing between maxima increases smoothly because the resonant condition

$$\alpha_{\max} = \sqrt{\frac{2\hbar^2}{m^*}\left(\frac{1}{2m^*}\left(\frac{n\pi\hbar}{L}\right)^2 - E_F\right)}\,, \tag{3.12}$$

shows a nonlinear dependence with n.

The transmission probabilities for $q \neq 0$ cannot be expressed in closed analytical form because the spins become coupled as illustrated

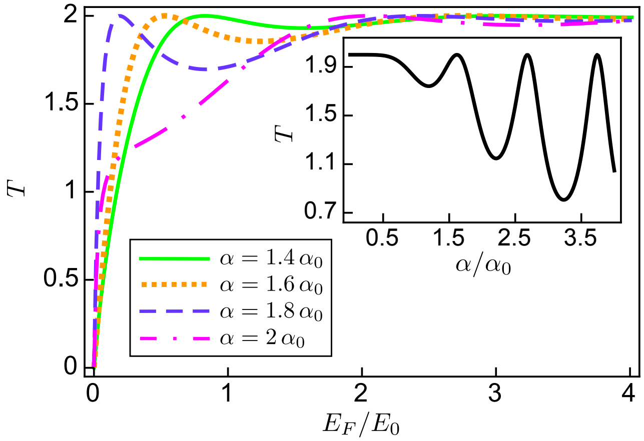

Figure 3.3: Total transmission probability as a function of the Fermi energy for $q = 0$, $L = 3.5L_0$ and different values of the Rashba strength α. Inset: Total transmission probability as a function of α for $q = 0$, $L = 3.5L_0$ and $E_F = 0.5E_0$.

in Eq. (3.3). It turns out that the contribution of these modes to the total transmission for a given energy is small as electrons are more likely to be refracted from the junction interfaces if $q \neq 0$. To verify this, let us define $\mathcal{T}_s$ as in Eq. (2.24) where we have replaced the subband index n by the spin index s and introduced a sum over the transmitted spin index $\sum_{s'}$,

$$\mathcal{T}_s(E) = 2\sum_{s'}\int_0^{\pi/2} T_{s's}(E,\phi)\cos\phi\, d\phi\,. \tag{3.13}$$

The total projected transmission is thus $\mathcal{T} = \sum_s \mathcal{T}_s$. In Fig. 3.4 we compare $\mathcal{T}$ from Eq. (3.13) with its $q = 0$ contribution. Clearly, the $q = 0$ mode contributes more than 75% to the full transmission for most energies. This confirms that with the mode $q = 0$ we can understand the basic dynamics of the transmission through our system. For completeness, however, in our calculations we take into account all channels to carefully assess the transport coefficients.

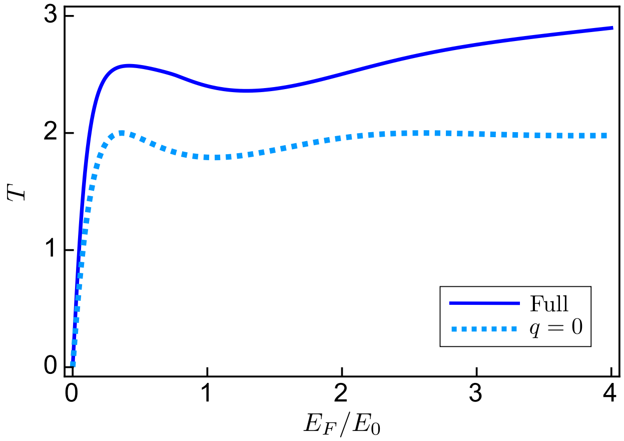

Figure 3.4: Total transmission probability as a function of the Fermi energy for $q = 0$ (dotted line) and integred over all q's (solid line). Parameters: $L = 3.5L_0$ and $\alpha = 1.7\alpha_0$.

3.2 Current

To calculate the current, we proceed as in Chapter 2 and employ the scattering approach for mesoscopic transport (see App. A). Then, the current I_s in the x direction for a fixed spin s is given by Eq. (2.13) which can be written in terms of the transmission found in Sec. 3.1 [see Eq. (3.13)]:

$$I_s = \frac{eW}{2\pi h} \int_{-\infty}^{\infty} dE\, \mathcal{T}_s(E)\, \mathcal{K}(E)\, \left[f_{\ell s}(E) - f_{rs}(E) \right] \,, \tag{3.14}$$

where $\mathcal{K}(E)$ is the momentum in the contacts derived from Eq. (1.34). To keep Eq. (2.13) more general we introduce a spin dependence in the Fermi distribution functions $f_{cs}(E) = f_{cs}(E - \mu_{cs}, T_c)$ with $c = \ell, r$ [see Eq. (2.14)] where the spin dependence is through the electrochemical potentials $\mu_{cs} = E_F + eV_{cs}$. The main difference between Eq. (2.13) and (3.14) is the absence of the 2 factor that comes from the graphene valley degeneracy. The total current is, finally, $I = \sum_s I_s$.

Following the same procedure as in Sec. 2.4, from Eq. (2.20) to Eq. (2.23), we obtain the total current I and the polarization current I_S in linear response as a function of the electric and thermoelectric conductances.

The electric conductance is given by

$$G_s = G_0 \frac{1}{2\pi} \int_{\infty}^{\infty} dE \; \mathcal{K}(E) \left(-\frac{\partial f}{\partial E} \right) \mathcal{T}_s(E) \,, \tag{3.15}$$

where $G_0 = e^2 W/h$ is the unit of conductance for a 2DES of width W along y. We note that this G_0 is different from that obtained for graphene [cf. Eq. (2.16)], because for ferromagnetic contacts (see Sec. 3.4) $\mathcal{K}(E)$ will be spin dependent and we need this dependence outside the scaling factor. Physically, G_s/G_0 is thus a spin-resolved conductance per unit of transverse length. Hence, the total conductance is $G = \sum_s G_s$. In the zero temperature limit, the conductance per spin reads

$$G_s = G_0 \frac{\mathcal{K}_F}{2\pi} \, \mathcal{T}_s(E_F) \,, \tag{3.16}$$

where $\mathcal{K}_F = \mathcal{K}(E_F) = \sqrt{2m^* E_F}/\hbar$.

The linear thermoelectric conductance reads

$$\mathcal{L}_s = \mathcal{L}_0 \frac{1}{k_B T_0 2\pi} \int_{\infty}^{\infty} dE \, \mathcal{K}(E)(E - E_F) \left(-\frac{\partial f}{\partial E} \right) \mathcal{T}_s(E) \,, \tag{3.17}$$

where $\mathcal{L}_0 = e k_B W/h$ is the natural scale of the thermoelectric response of a 2DES of width W. For the same reason as before this scaling factor is different from the $\mathcal{L}_0$ obtained in Chapter 2 [cf. Eq. (2.19)]. The total thermoelectric conductance is $\mathcal{L} = \sum_s \mathcal{L}_s$. At very low temperature, a Sommerfeld expansion [35] yields

$$\mathcal{L}_s = \mathcal{L}_0 \frac{k_B T_0 \pi}{6 E_F} \mathcal{K}_F \left(\frac{1}{2} \mathcal{T}_s(E_F) + E_F \frac{\partial \mathcal{T}_s}{\partial E_F} \right) \,, \tag{3.18}$$

where the derivative is defined as $\frac{\partial}{\partial E_F} \equiv \frac{\partial}{\partial E}\Big|_{E=E_F}$.

Figure 3.5 presents the total electric and thermoelectric conductances as a function of the Fermi energy from a calculation of Eqs. (3.16) and (3.18), respectively. The transmission is determined from a full evaluation of Eq. (3.13). We find that the electric conductance (solid line) is a monotonically increasing function of E_F. At sufficiently large energy values, G goes as $E_F^{1/2}$ because the transmission approaches its maximum value when $E_F \gg E_0$ (see Figs. 3.2 and 3.3). Only at low energies G presents a small deviation from this behavior, which is much more visible when we calculate the thermoelectric

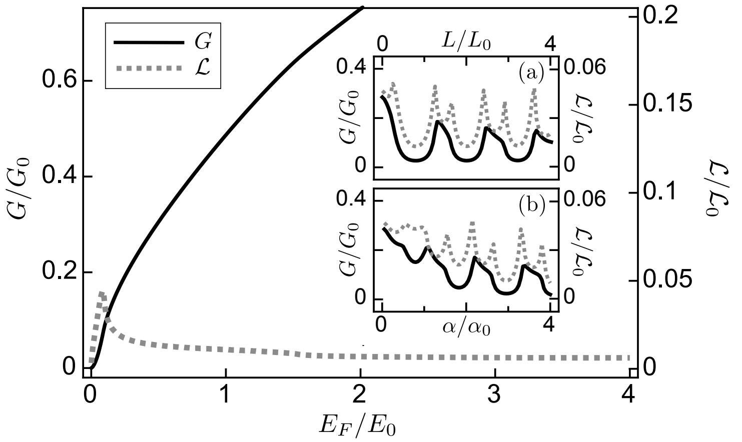

Figure 3.5: Electric conductance (left axis) and thermoelectric conductance (right axis) as a function of the Fermi energy at low temperature. Parameters: $k_BT_0 = 0.01E_0$, $L = 2.9L_0$ and $\alpha = 2.6\alpha_0$. The electric conductance as a function of $L(\alpha)$ is plotted in the left axis of the inset (a)[(b)]. In the right axis of the same inset the thermoelectric conductance is depicted. Parameters of inset (a)[(b)]: $k_BT_0 = 0.01E_0$, $E_F = 0.1E_0$ and $\alpha = 2.6\alpha_0(L = 2.9L_0)$.

conductance (dotted line). While at high energies $\mathcal{L}$ approaches zero as $E_F^{-1/2}$ as dictated by Eq. (3.18), the thermoelectric conductance shows a peak at low values of E_F.

The insets of Fig. 3.5 depict G and $\mathcal{L}$ as a function of the spin-orbit region width (top panel) and the Rashba coupling intensity (bottom panel). We observe that both responses are strongly modulated and present maxima at fixed values. This originates from the transmission oscillations discussed in Sec. 3.1 as a function of α or L. Interestingly, our device works as a current modulator in response to voltage or temperature biases applied to normal leads. This is in contrast with the spin transistor proposal of Ref. [10]. Our system (both the leads and the 2DES channel) is entirely nonmagnetic. It is precisely due to this reason that $G_+ = G_-$ and $\mathcal{L}_+ = \mathcal{L}_-$ and no spin polarization is possible.

3.3 Charge and spin thermopower

In Eq. (3.18) we find that the thermoelectric conductance comprises two terms at low temperature, in contrast to the electric conductance, Eq. (3.16), which consists of a single term. With the aim at understanding more clearly this additional contribution we calculate the charge thermopower or Seebeck coefficient, $S = (V/\Delta T)_{I=0,I_S=0}$, given by Eq. (2.26). Inserting Eqs. (3.16) and (3.18) in Eq. (2.26), we obtain the low-temperature thermopower,

$$S = -S_0 \frac{k_B T_0 \pi^2}{6E_F} \left(\frac{1}{2} + E_F \sum_s \frac{\partial \mathcal{T}_s / \partial E_F}{\mathcal{T}_s(E_F)} \right) . \tag{3.19}$$

The Seebeck coefficient is measured in units of $S_0 = k_B/e$. We observe two contributions in Eq. (3.19). The first term $S_{in} = -S_0 k_B T_0 \pi^2 /(12E_F)$ is constant and represents an intrinsic contribution to the entropy per unit charge of thermally excited electrons. We already found this factor in Chapter 2 [Eq. (2.27)]. Like graphene, the intrinsic term is independent of the scattering potential and the sample details. This suggest that S_{in} is unique to 2DES since in quasi-1D systems (quantum point contacts) and quasi-0D systems (quantum dots) this contribution is absent. Therefore, the intrinsic term can be explained as a dimensionality effect. The only difference is that in graphene S_{in} is doubled because its energy dispersion is linear, $E \sim \mathcal{K}$, unlike the quadratic dependence in our semiconductor 2DES [Eq. (1.34)]. The second term, $S_{tr} = -(S_0 k_B T_0 \pi^2/6) \sum_s (\partial \mathcal{T}_s \;/\partial E_F)/\mathcal{T}_s$, is a purely transport contribution that arises from the energy dependence of the transmission function.

In fact, as in Sec. 2.5, using the G_s function defined in Eq. (3.16) we can write Eq. (3.19) as a Mott-like formula. The obtained expression takes the same form as Eq. (2.29) but replacing G_n by G_s given by Eq. (3.16).

We analyze the relative importance between the intrinsic and the transport terms. To visualize this, Fig. 3.6 shows the different contributions as a function of the Fermi energy. In general, both have comparable strengths and should then be treated on equal footing. Note that S is always negative because the generated voltage tends to counteract the thermal bias. Below, we will show deviations of this behavior when the sample is attached to ferromagnetic contacts. In Fig. 3.6 S_{in} grows as $1/E_F$ and quickly goes to zero. On the other

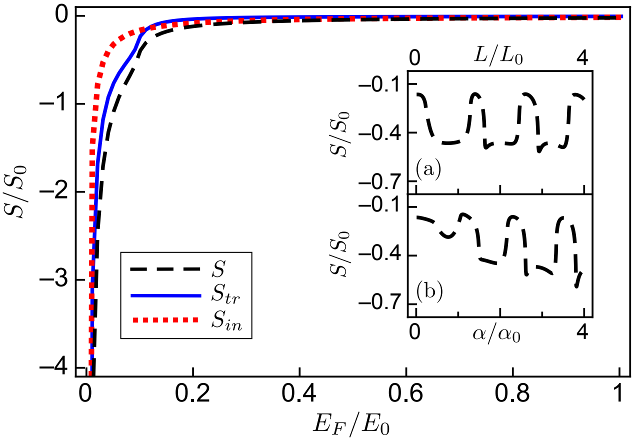

Figure 3.6: Seebeck coefficient at low temperature as a function of the Fermi energy. Parameters: $k_BT_0 = 0.01E_0$, $L = 2.9L_0$ and $\alpha = 2.6\alpha_0$. The two insets, (a) and (b), show S as a function of L and α, respectively. Parameters of inset (a)[(b)]: $k_BT_0 = 0.01E_0$, $E_F = 0.1E_0$ and $\alpha = 2.6\alpha_0$ ($L = 2.9L_0$).

hand, although the overall trend of S_{tr} is similar to the intrinsic term, we observe in S_{tr} a stronger effect due to the potential scattering at low energy. Finally, we recall that both G and $\mathcal{L}$ present oscillations as a function of L and α, see insets (a) and (b) of Fig. 3.5. The thermopower, which is the ratio between the thermoelectric and electric conductances, also presents these oscillations as seen in the insets (a) and (b) of Fig. 3.6. Importantly, the oscillations are due to the transport term since S_{in} is independent of α and L.

We note in passing that the main properties of S discussed above can be also detectable in heat current measurements. Due to Onsager reciprocity, the electrothermal conductance (Peltier effect) is directly connected to the thermoelectric conductance (Seebeck effect), see App. E. Moreover, we show in App. E that the Wiedemann-Franz law holds at low temperature. Then, it is natural to ask to what extent the Sommerfeld approximation is valid. To do so, we compare the results of Eqs. (3.15) and (3.17), i.e., the exact calculation at $k_BT_0 = 0.01E_0$, with Eqs. (3.16) and (3.18), which are valid at very low temperature. The difference between the exact and Sommerfeld calculation of the thermoelectric conductance is shown in the inset of

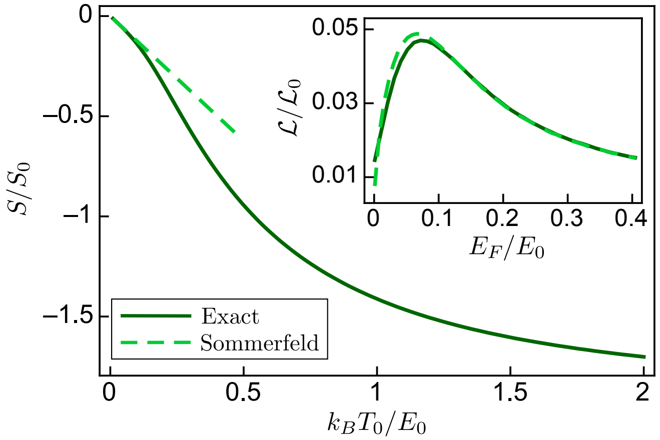

Figure 3.7: Thermopower as a function of the base temperature for both the exact calculation and the lowest order Sommerfeld approximation. Parameters: $E_F = E_0$, $L = 3.5L_0$ and $\alpha = 1.7\alpha_0$. The inset presents a comparison between the exact calculation of the thermoelectric conductance and the Sommerfeld result as a function of the Fermi energy. Parameters of the inset: $k_BT_0 = 0.01E_0$, $L = 3.5L_0$ and $\alpha = 1.7\alpha_0$.

Fig. 3.7. At low energies, $E_F/E_0 < 0.1$, there exists a small deviation between the exact curve and the Sommerfeld result. This confirms that the Sommerfeld expansion is no longer valid when $E_F \sim k_BT_0$. The main panel of Fig. 3.7 presents the deviation of the Sommerfeld calculation (dashed line) for the Seebeck coefficient compared with the exact value (solid line) as a function of the background temperature. In the Sommerfeld expansion, S depends linearly with T_0 as shown in Eq. (3.19). Therefore, for high temperatures such that $k_BT_0/E_F > 0.1$ the Sommerfeld approximation is not valid.

We end this section considering the spin Seebeck coefficient $S_\mathcal{S}$ given by Eq. (2.30). For normal leads the spin Seebeck is identically zero since the system is nonmagnetic and the spin polarization is not possible. We consider in the next section a 2DES coupled to ferromagnetic leads, a system where $S_\mathcal{S}$ does not necessarily vanish.

3.4 Ferromagnetic contacts

The case of ferromagnetic contacts is relevant for spin-injection problems in ferromagnet-semiconductor junctions (see Sec. 1.1). We describe the contacts with the Stoner-Wohlfarth model for itinerant ferromagnetism. The electronic bands for opposite spins become split due to exchange interaction between carriers. Then, the Hamitonian reads

$$\mathcal{H}_\Delta(x) = \Delta(x)\,\hat{n}\cdot\vec{\sigma} + |\Delta(x)|\,, \tag{3.20}$$

where $\hat{n}$ is the magnetization direction in which the leads are polarized, $\vec{\sigma}$ is the spin vector and $\Delta(x)$ is the Stoner splitting, which is finite in the x-positions of the leads only. For metallic electrodes, Δ is of the order of a few eV, introducing serious conductivity mismaches at the junction [88], a problem which can be mitigated using tunnel barriers [89]. For the present discussion, it is more convenient to consider spin injectors made of diluted magnetic semiconductor compounds, which show giant Zeeman splittings Δ up to 20 meV for moderate values of external magnetic fields [90]. For definiteness, we consider in Eq. (3.20) an energy shift $|\Delta(x)|$ that eases the spin transport analysis. In particular, this shift eliminates the effect of a potential mismatch and can be experimentally implemented with a potential gating of the central region.

In the same way of the piecewise constant function $\alpha(x)$ in Sec. 3.1, we take a uniform $\Delta(x)$ in each of the three parts of our system: nonzero Δ_c in the contacts and vanishingly small Δ in the 2DES. For the numerical implementations, the interfaces are described with slightly smoothed functions, as explained in App. D. We investigate two different orientation schemes: parallel (P) and antiparallel (AP) configurations as sketched in the insets of Fig. 3.8. The case of parallel polarization corresponds to $\Delta_\ell = \Delta_r \equiv \Delta$ whereas the antiparallel case results from $\Delta_\ell = -\Delta_r \equiv \Delta$, where Δ is half of the absolute Zeeman splitting. In what follows, we take the polarization in the x-direction: $\hat{n}\cdot\vec{\sigma} = \sigma_x$. Thus, we define a potential in the leads,

$$v_s(x) = s\Delta(x) + |\Delta(x)|\,, \tag{3.21}$$

where $s = \pm$ labels the spin in the x-direction. Then, for the P configuration the electrons with $s = +$ (minority spins) are confined by a potential well of width d (the separation between contacts, see App. D) while those with $s = -$ feel no potential as they travel (majority spins). In the AP configuration, both types of carrier experience a potential step but localized in opposite contacts. Due to the differing potential landscapes, we expect strong changes as compared with the nonmagnetic case treated in the previous sections.

The dispersion relation on the contacts generalizes Eq. (1.34) conveniently modified to account for the Stoner field:

$$E = \frac{\hbar^2 \mathcal{K}_{cs}^2}{2m^*} + s\Delta_c + |\Delta_c| \,. \tag{3.22}$$

Importantly, the total momentum $\mathcal{K}_{cs}$ now depends on both the contact and the spin. As a consequence, since the q-momentum remains invariant, we find

$$\mathcal{K}_{cs}^2 = k_{cs}^2 + q^2 = \frac{2m^*}{\hbar^2}\left(E - s\Delta_c - |\Delta_c|\right) \,. \tag{3.23}$$

The channel amplitude equation expressed in Eq. (3.3) keeps the same form, with the only addition of the spin dependent potential $v_s(x)$ and the replacement $k \to k_{cs}$ in the asymptotic conditions Eq. (3.4). From the resulting expression we calculate the new probability transmissions and obtain, finally, the total current in the propagation direction which is the same as Eq. (3.14) replacing $\mathcal{K}(E) \to \mathcal{K}_{\ell s}(E)$. Here $\mathcal{K}_{\ell s}(E)$ follows from Eq. (3.23) with $c = \ell$ taken for convenience (the current conservation condition $I_\ell + I_r = 0$ is always fulfilled). The electric and thermoelectric conductances in the limit of linear response are obtained in the same manner as in Sec. 3.2. At very low temperature, they read

$$G_s = G_0 \frac{1}{2\pi}\, \mathcal{K}_{\ell s}(E_F)\, \mathcal{T}_s(E_F) \,, \tag{3.24a}$$

$$\mathcal{L}_s = \frac{k_B^2 T_0 \pi^2}{3e}\, \frac{\partial G_s}{\partial E_F} \,, \tag{3.24b}$$

In Fig. 3.8 we present the total electric conductance, $G = G_+ + G_-$, as a function of E_F. We distinguish between P (a) and AP (b) polarizations of the magnetic leads. Consider first the case without spin-orbit interaction ($\alpha = 0$). For parallel orientation the majority electrons are not scattered back while the minority electrons feel

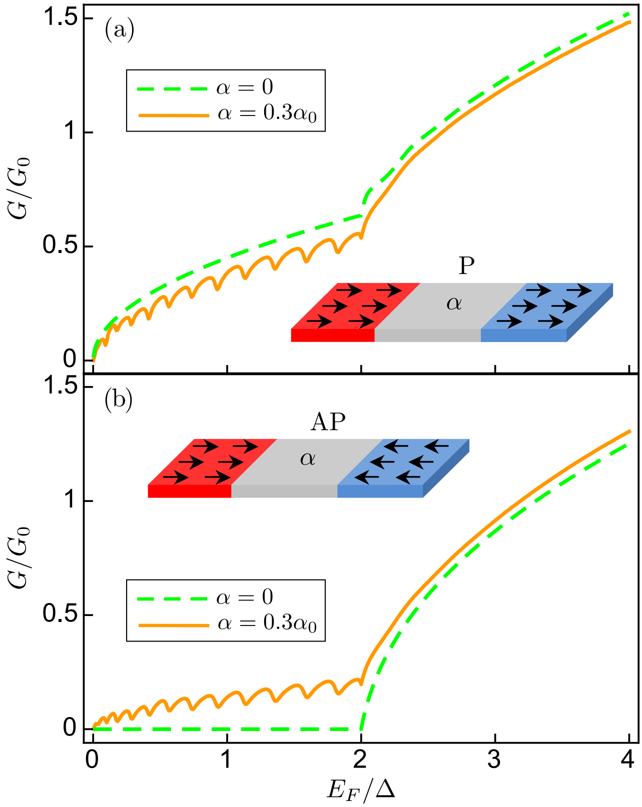

Figure 3.8: Electric conductance as a function of the Femi energy for P (a) and AP (b) polarizations along the x-direction at low temperature. Solid and dashed curves represent the case with or without spin-orbit interaction in the central region, respectively. The Stoner field splitting $\Delta = 10\,\text{meV}$ is taken as the energy unity. This way $L_0 = \sqrt{\hbar^2/(m^*\Delta)} = 18.2\,\text{nm}$ and $\alpha_0 = \sqrt{\hbar^2\Delta/m^*} = 182\,\text{meV nm}$. Parameter: $L = 8L_0$.

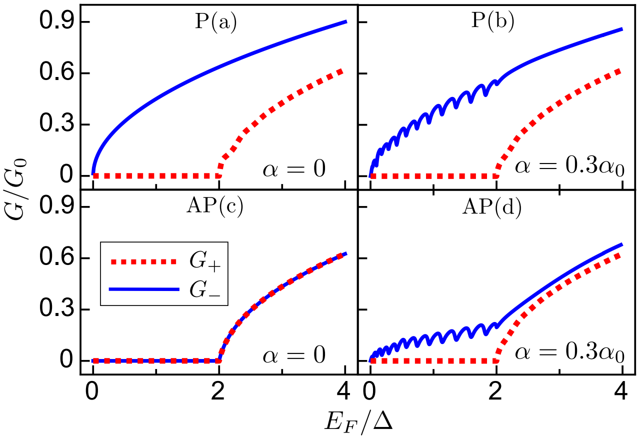

Figure 3.9: Spin components of the electric conductance for parallel, (a) and (b), and antiparallel, (c) and (d), configurations as a function of the Fermi energy at low temperature. Parameter: $L = 8L_0$.

a potential well of depth 2Δ. Then, when $E_F < 2\Delta$ we only have one propagating spin channel, $s = -$, and the conductance is given simply by the number of open channels, which scales $\propto E_F^{1/2}$ as discussed in Sec. 3.2. For $E_F > 2\Delta$ the $s = +$ propagating mode becomes active. Thus, the v_+ potential causes the transmission to oscillate with energy. These oscillations are akin to the Ramsauer oscillations in electron scattering [91]. This can be more clearly seen in Fig. 3.9(a), which depicts the behavior separately for G_+ and G_-. The majority spins contributes to G with a $E_F^{1/2}$-dependent function while the minority spins do not attain a nonzero G until $E_F > 2\Delta$. Above this energy threshold, the electrons with spin $s = +$ lead to smooth oscillations of G due to the Ramsauer effect. In the antiparallel case [Fig. 3.8(b)], the conductance is zero below the energy threshold $E_F = 2\Delta$ for both spin indices, see Fig. 3.9(c), since $s = -$ electrons are reflected back from the step potential at the right junction according to Eq. (3.21) while electronic channels with $s = +$ are not active for $E_F < 2\Delta$ due to the step potential at the left contact.

Turning on the spin-orbit potential alters the previous picture. For energies below the threshold, Fig. 3.8 shows a different type of oscillation independently of the leads' magnetic orientation. These are due to resonant Fano interference between the propagating spins and the quasibound states of opposite spins trapped between the polarized contacts [85, 92]. Figure 3.9(b) shows that the Fano oscillations in the P case are only possible for electrons with spin $s = -$ since for $E_F < 2\Delta$ the electrons $s = +$ are evanescent states. At higher energies the two modes become propagating states and the Fano oscillations vanish. In the AP case, the oscillations also appear for $E_F < 2\Delta$ but these are now due to electrons with $s = -$ undergoing multiple reflections between the junctions since minority electrons are inactive for transport until $E_F = 2\Delta$ [92].

Figure 3.10 shows the thermoelectric conductance as a function of Fermi energy for both P and AP configurations. According to Eq. (3.24b), $\mathcal{L}$ can be written as a function of the energy derivative of the electric conductance. As a consequence, the Rashba induced oscillations for $\alpha \neq 0$ become largely amplified for $E_F < 2\Delta$. Remarkably, the $\mathcal{L}$ curves cross the horizontal axis, taking positive and negative values, whereas the case $\alpha = 0$ always gives $\mathcal{L} > 0$. Therefore, the combined influence of ferromagnetic leads and spin-orbit interaction can drive the electronic current either from the hot to the cold reservoir (as in the normal case, see Fig. 3.5) or, notably, from the cold to the hot reservoir. The latter phenomenon is independent of the relative magnetic orientation (parallel or antiparallel), the main difference being that below the energy threshold the thermoelectric conductance vanishes in the AP case $\alpha = 0$, similarly to the electric conductance [Fig. 3.8(b)]. Finally, for high energies $\mathcal{L}$ smoothly decays to zero since the transmission becomes weakly energy dependent for $E_F \gg \Delta$. This demonstrates that the spin-orbit interaction in 2D spin transistors leads to stronger effects for energies lower than the Zeeman splitting.

We depict in Fig. 3.11 the spin-resolved thermoelectric conductances. As expected, the large amplitude oscillations in the P case arise in the majority spin channel only [Fig. 3.11(a)]. For $\alpha = 0$ the Ramsauer-like oscillations are visible above the energy threshold in the minority channel [Fig. 3.11(c)]. In the antiparallel case, the thermoconductances obey $\mathcal{L}_+ = \mathcal{L}_-$ and attain their highest value when E_F reaches Δ because the transmission variation is largest at that point, as both spin channels become propagating [Fig. 3.11(d)]. In Fig. 3.11(b) the Ramsauer-like oscillations are also visible for $E_F >$

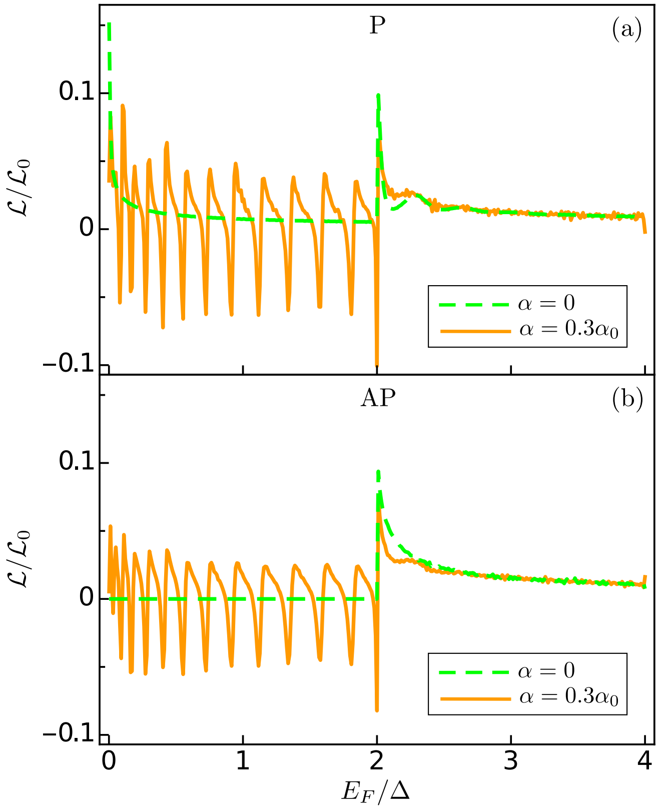

Figure 3.10: Thermoelectric conductance as a function of the Femi energy for P (a) and AP (b) polarizations along the x-direction at low temperature. Parameters: $L = 8L_0$ and $k_BT_0 = 0.01E_0$.

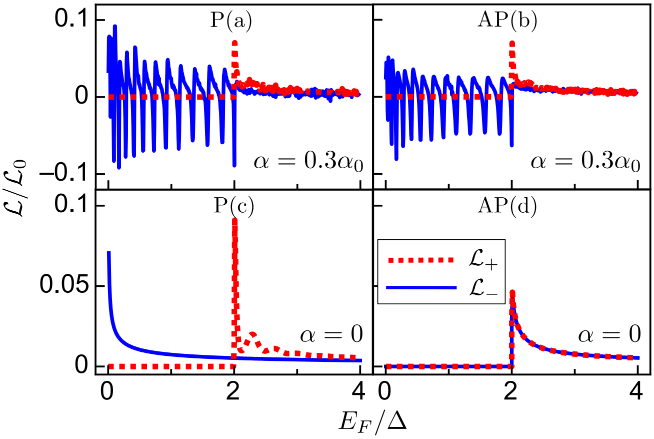

Figure 3.11: Spin components of the thermoelectric conductance for parallel, (a) and (c), and antiparallel, (b) and (d), configuration as a function of the Fermi energy at low temperature. Parameters: $L = 8L_0$ and $k_BT_0 = 0.01E_0$.

2Δ.

The thermopower obeys Eq. (2.29) but now G_n is replaced by the G_s function calculated from Eq. (3.24a). In Fig. 3.12 we plot the charge Seebeck coefficient S, for both P (a) and AP (b) configurations. For $\alpha = 0$, S is almost zero. Only for energies slightly higher than 2Δ we observe a dip that correlates with the thermoelectric conductance peak observed in Fig. 3.10. In contrast to the normal case depicted in Fig. 3.6, here S oscillates and changes its sign for $E_F < 2\Delta$. This indicates that at given temperature difference, depending on the value of E_F we can generate positive or negative thermovoltages. This is a very interesting effect since without ferromagnetic contacts the thermopower is always negative. We need to introduce both a Zeeman spliting and a spin-orbit interaction to generate the sign oscillations in S, which are more intense for AP configurations. We emphasize that although thermopower sign changes can be detected in quantum dots [93, 94] or molecular transistors [95], the effect discussed here occurs in an *extended* 2D system.

To determine the spin Seebeck coefficient S_S at low temperature,

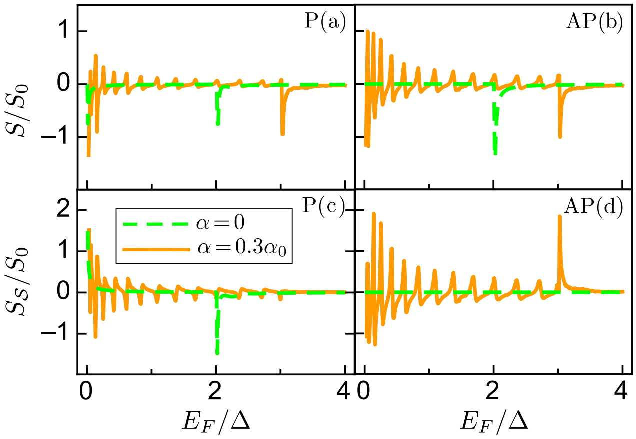

Figure 3.12: Seebeck, (a) and (b), and spin-Seebeck, (c) and (d), coefficient as a function of the Fermi energy for both P and AP configurations of leads' magnetic moments pointing along the x direction. Solid and dashed curves represent the cases with and without Rashba coupling in the central region, respectively. Parameters: $L = 8L_0$ and $k_BT_0 = 0.01E_0$.

we introduce Eq. (3.24) in Eq. (2.30), obtaining

$$S_{\mathcal{S}} = -S_0 \frac{k_B T_0 \pi^2}{3} \left(\frac{\partial \ln G_+}{\partial E_F} - \frac{\partial \ln G_-}{\partial E_F} \right) , \tag{3.25}$$

where the G_s function is given by Eq. (3.24a). Here, the spin indices ± follow the quantization axis established by the leads' magnetization, i.e., the x-direction. Unlike the normal case, we now expect nonzero values of $S_{\mathcal{S}}$ since, quite generally, $G_+ \neq G_-$. Figure 3.12(c) shows the results for the parallel configuration in the case with (solid line) and without (dashed line) Rashba interaction. We observe that for $\alpha = 0$ the spin Seebeck coefficient presents a smooth behavior and only at energies slightly larger than 2Δ the Ramsauer-like oscillations arise.

When the Rashba coupling is active, $S_{\mathcal{S}}$ changes its sign alternatively for $E_F < 2\Delta$. This indicates that at fixed value of ΔT depending on E_F we can generate a positive or negative spin voltage $V_{\mathcal{S}}$. The case for the AP configuration is plotted in Fig. 3.12(d). For zero Rashba coupling $S_{\mathcal{S}} = 0$ since the spin components of the elec-

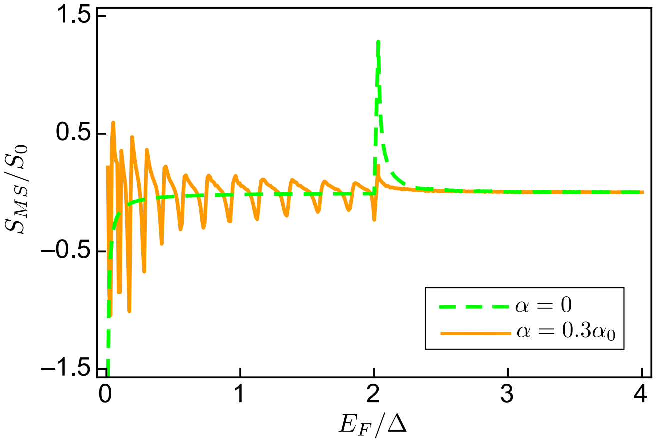

Figure 3.13: Magneto-Seebeck coefficient as a function of the Fermi energy at very low temperature. The solid and dashed curves represent the cases with and without spin-orbit interaction in the central region, respectively. Parameters: $L = 8L_0$ and $k_BT_0 = 0.01E_0$.

tric and thermoelectric conductance are equivalent, see Figs. 3.9(c) and 3.11(d). With nonzero value of α we recover the oscillations for $E_F < 2\Delta$, with an amplitude larger than for the charge case [Figure 3.12(b)]. The oscillations in $S_{\mathcal{S}}$ are more intense for the AP than for the P configuration. It is due to a spin valve effect, i.e., for $E_F < 2\Delta$ we do not find any active channel for the AP configuration, while for the P configuration the mode $s = -$ is open. Hence, for $E_F < 2\Delta$ the electric conductance takes lower values for the AP configuration than for the parallel one. As a consequence, $S_{\mathcal{S}}$, which is inversely proportional to G, attains higher values.

As we have mentioned in the introduction (Sec. 1.2) the magneto-Seebeck effect is a spintronic phenomenon that gives rise to changes in the thermopower of a magnetic junction upon switching the leads' magnetic moments [26]. In Fig. 3.12(a) and (b) we found that the thermopower significantly changes during the transition from P to AP configurations. Then, it is natural to quantify this departure by defining the magneto-Seebeck coefficient S_{MS} as

$$S_{MS} = S_P - S_{AP}\,, \tag{3.26}$$

where S_P and S_{AP} are the thermopower in the parallel and antiparallel configuration, respectively. Figure 3.13 shows the magneto-Seebeck coefficient as a function of the Fermi energy for $\alpha = 0$ (dashed line) and $\alpha \neq 0$ (solid line). When the Rashba coupling is absent, S_{MS} is closer to zero and only for energies slightly exceeding 2Δ a peak arises since the two spin channels are open and we have an increase of the electric conductance. Conspicuously, for a finite value of α the magneto-Seebeck coefficient presents oscillations and sign changes, much like the thermopower oscillations discussed above. This supports the suggestion that the charge thermopower can be controlled by changing the relative magnetization orientation. While the experiment reports sign changes of S_{MS} as a function of the base temperature [26], we here predict a similar effect by tuning the Fermi energy of the 2DES device.

3.5 Conclusions

In this chapter we have found that for nonferromagnetic contacts the charge Seebeck coefficient behaves similarly to the graphene device studied in Chapter 2. The thermopower is always negative and only at low energies the transport term S_{tr} shows a stronger effect due to potential scattering. Additionally, we have observed thermopower oscillations when we tune the Rashba strength or the length of central region. However, in contrast to graphene (Chapter 2), we have not observed spin polarization in the electric or thermoelectric conductance because of the different naature of the spin-orbit coupling in both systems. Only for ferromagnetic contacts we obtain spin polarizations in a 2DES. Further, when we introduce ferromagnetic contacts, the charge thermopower is an oscillating function of the Fermi energy and change its sign. These sign changes suggest the possibility of controlling the thermocurrent direction using a gate that tunes the Fermi energy. Moreover, we have observed that S depends on the relative orientation of the leads' magnetization and, as a consequence, we have studied the magneto-Seebeck ratio which also shows sign changes.

Although the injection and detection of spin polarized currents is possible attaching ferromagnetic terminals to the semiconductor channel and employing nonlocal voltage detection, the spin-injection efficiency between dissimilar materials tends to be low. An interesting alternative is presented in Chapter 4 where we will use a pair of quantum point contacts (QPCs) working as spin injectors and detectors.

4. Nonmagnetic spin transistors

As we have mentioned in Chapter 3, here we will study the transport properties of a really interesting system which is fully nonmagnetic (neither ferromagnetic contacts nor external magnetic fields are needed for its operation principle) and relies on a semiconductor-only structure[1]. We consider a semiconductor layer with a Rashba spin-orbit interaction in the central region and a pair of quantum point contacts (see Sec. 1.3.2.2) that works as spin injectors and detectors [8, 9]. The electric confinement in the point constrictions leads to an effective magnetic field that polarizes the electrons in directions perpendicular to the spin-orbit field present in the central channel. Nonmagnetic spin transistors are attractive devices and have been pursued in different proposals [96–101].

We are interested in observing the interplay between Fabry-Perot and Datta-Das oscillations. We consider the case when the conductance of both quantum point contacts is set below the value corresponding to a fully open mode. Then, the waveguide potentials can be described as tunnel barriers and transport across them occurs via evanescent states [70, 102]. Effectively, the system electronic potential is globally seen as a double barrier with a quantum well of variable depth. It is well known that these potential landscapes in general support the presence of resonant scattering due to Fabry-Perot-like oscillations arising from wave interference between the tunnel barriers. But at the same time we have spin-orbit induced oscillations due to the precession of spins traveling between the barriers. Therefore, one would naturally expect a competition between resonant tunneling and spin precession oscillations in a system comprising two serially coupled QPCs. Below, we show that this is indeed the case and that the combination of both oscillation modes leads to rich physics not only in the strictly one-dimensional case but also when more realistic samples with a finite transversal width are studied.

---

[1] The contents of this chapter are based on M. I. Alomar, Llorenç Serra and David Sánchez, Phys. Rev. B **94**, 075402 (2016).

The subject of resonant tunneling effects and spin-orbit fields has been investigated in a number of works giving rise to interesting predictions. For instance, Voskoboynikov *et al.* find that the transmission probability significantly changes in the presence of the Rashba coupling [103] while de Andrada e Silva *et al.* obtain spin polarizations for an unpolarized beam of electrons impinging on a double-barrier nanostructure [104]. Koga *et al.* analyze spin-filter effects in triple barrier diodes [105] whereas Ting and Cartoixà examine the double barrier case [106]. The dependence of the electronic tunneling on the spin orientation is treated by Glazov *et al.* [107]. These structures suffer from phase-breaking effects, as shown by Isić *et al.* [108].

As in previous chapters we consider a purely ballistic system where scattering is elastic and the transmission probabilities are determined within the quantum scattering approach. Scattering can take place at the interfaces between the quantum point contacts and the quantum well or due to interaction between the spins and the spin-orbit interaction. Importantly and in contrast to previous works investigating spin transistor transport properties, the spin-dependent transmission depends on the relative angle between the spin-orbit fields in the QPCs. This is an excellent property that allows us to tune the spin direction of the electrons impinging on the quantum well [109]. For a null relative angle, within a pure one dimensional model we find that whereas the spin-conserving transmission shows resonant tunneling peaks as a function of the spin-orbit strength the spin-flip transmission always vanishes.

Furthermore, for both types of transmissions the spin precession oscillations as a function of the spin-orbit strength in the quantum well appear only when the QPCs have effective spin-orbit magnetic fields with an angle that differs from the spin-orbit coupling in the well. This effect can be also seen when the quantum well length is varied. However, we point out that the QPCs have an additional effect as tunnel barriers that lead to Fabry-Perot resonances which can compete with the Datta-Das oscillations in the transmission curves yielding quasiperiodic patterns. Now, since a realistic sample has a finite width, we also consider a quasi-one dimensional system, in

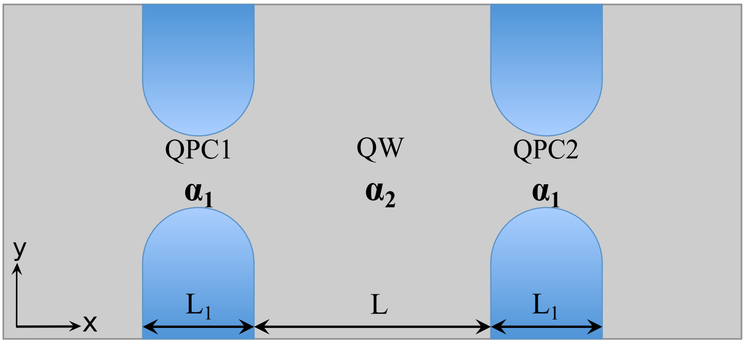

Figure 4.1: Pictorial representation of our system. A semiconductor layer (light gray) with metallic electrodes (blue) shows two quantum point contacts in a series (QPC1 and QPC2) and a two-dimensional cavity in between (QW). The spin-orbit coupling differs in each area (α_1 and α_2) due to distinct electric fields applied to the electrodes (lateral in the metallic electrodes, perpendicular in the QW). L_1 and L correspond to the width of QPCs and central region, respectively.

which case the spin-orbit intersubband coupling potential must be also taken into account. Remarkably, we find that our results derived from the one-dimensional model are also observable in two dimensions for moderately low values of the spin-orbit strength. This implies that the oscillation interplay discussed here can be probed with today's experimental techniques.

4.1 Theoretical model

We consider a semiconductor layer partitioned into five different regions as in Fig. 4.1: two reservoirs, two QPCs and a quantum well (QW). The blue areas are gate electrodes that form constrictions in the QPC1 and QPC2 between the left and right reservoir and the central well. We take x as the transport direction. The spin-orbit potentials acting on the QPCs (both with strength α_1) and the QW (strength α_2) are in general different [109]. Thus, our Hamiltonian reads

$$\mathcal{H} = \mathcal{H}_0 + \mathcal{H}_{SO1} + \mathcal{H}_{SO2} \,, \tag{4.1a}$$

$$\mathcal{H}_0 = \frac{p_x^2 + p_y^2}{2m^*} + V(x,y) \,, \tag{4.1b}$$

$$\mathcal{H}_{SO1} = \frac{\alpha_1}{\hbar} \Big((\vec{\sigma} \times \vec{p})_z \cos\phi + (\vec{\sigma} \times \vec{p})_y \sin\phi \Big) \ , \tag{4.1c}$$

$$\mathcal{H}_{SO2} = \frac{\alpha_2}{\hbar} \left(\vec{\sigma} \times \vec{p}\right)_z \ , \tag{4.1d}$$

where $\mathcal{H}_0$ represents the free part of the total Hamiltonian $\mathcal{H}$, with $p_i = -i\hbar\partial/\partial_i$ $(i = x, y)$ the linear momentum operator and m^* the conduction-band effective mass of the electrons in the semiconductor heterostructure. $V(x,y)$ confines electrons in the (transversal) y direction and includes in x two identical constrictions that define an intermediate region (the cavity or well) of length L. The spin-orbit terms of $\mathcal{H}$ are $\mathcal{H}_{SO1}$ and $\mathcal{H}_{SO2}$, where the first (second) is active on the QPCs (QW) only. Here, $\vec{\sigma} = (\sigma_x, \sigma_y, \sigma_z)$ and $\vec{p} = (p_x, p_y, 0)$ are the Pauli matrices and the momentum vector, respectively. In the central region, the α_2 spin-orbit field [Eq. (4.1d)] arises from the confining electric field perpendicular to the QW plane (the z-direction see our discussion in Sec. 1.3.2.1). In the constrictions, there exists in the α_1 spin-orbit potential [Eq. (4.1c)] an additional contribution from the lateral electric field applied to the QPCs along y. This field couples asymmetrically to the electrodes in Fig. 4.1 (blue areas) and, as a consequence, a high spin-orbit interaction emerges in the QPCs, as experimentally demonstrated in Refs. [8, 109]. The spin-orbit strength can be further enhanced by electron-electron interactions, doping potentials or exchange correlations [110, 111]. Our goal is not to describe these effects microscopically but rather focus on the transport properties. Hence, we lump these effects into the parameter α_1, which can be tuned with the lateral electric field [8].

A convenient way of quantifying the strength of the two different components present in the QPCs (due to either lateral or perpendicular electric fields) is with the definition in Eq. (4.1c) of the angle ϕ. Therefore, we can turn off the lateral contribution by setting $\phi = 0$ in which case $\mathcal{H}_{SO1}$ and $\mathcal{H}_{SO2}$ are identical except for the spin-orbit strength. For $\phi = \pi/2$ the lateral electric field contribution to the spin-orbit potential dominates over that of the perpendicular electric field. Thus, the ensuing spin-orbit field in $\mathcal{H}_{SO1}$ is orthogonal to that in $\mathcal{H}_{SO2}$. This ability to manipulate the orientation of the spin-orbit fields is crucial for the working principle of our system and has been proven in the experiments reported earlier [109]. It is a property that makes this device unique and that is absent from previous spin transistor studies. Another advantage of the QPCs is to reduce the wavevector spread of injected electrons in contrast to extended interfaces [96]. Spin injection and detection with QPCs have been discussed in Refs. [112, 113] in the context of ballistic spin resonance. Here, we do not consider any external magnetic field and all the spin dynamics originates from the effective magnetic fields due to the spin-orbit interactions present in the system, which makes our system an all-electric spin transistor.

4.2 One-Dimensional case

Let us for the moment disregard transverse channel effects and consider a purely one-dimensional model. We expect that this is a good approximation when the point contacts support evanescent states only. We will later discuss the more realistic case where the electronic waveguides have a nonzero transversal width. In this limit we describe the QPCs electrostatic potential, $V(x,y)$, with a double tunnel barrier of width L_1 and height V_0 and the in-between cavity with a quantum well of length L and bottom aligned with that of the reservoirs energy bands, see the sketch in Fig. 4.2. We then set $p_y = 0$ in Eq. (4.1a). Since the potential is piecewise constant, the eigenstates of $\mathcal{H}$ are readily found for the five regions defined in Fig. 4.2:

$$\Psi^0_{\ell s}(x) \equiv \Psi^I_{\ell s} = \Psi^V_{\ell s} = \frac{1}{\sqrt{2}} \begin{pmatrix} \sqrt{1 + s\,\sin\phi} \\ -is\sqrt{1 - s\,\sin\phi} \end{pmatrix} e^{ik^{(0)}_{\ell} x}, \tag{4.2a}$$

$$\Psi^1_{\ell s}(x) \equiv \Psi^{II}_{\ell s} = \Psi^{IV}_{\ell s} = \frac{1}{\sqrt{2}} \begin{pmatrix} \sqrt{1 + s\,\sin\phi} \\ -is\sqrt{1 - s\,\sin\phi} \end{pmatrix} e^{ik^{(1)}_{\ell s} x}, \tag{4.2b}$$

$$\Psi^2_{\ell s}(x) \equiv \Psi^{III}_{\ell s} = \frac{1}{\sqrt{2}} \begin{pmatrix} 1 \\ -is \end{pmatrix} e^{ik^{(2)}_{\ell s} x}, \tag{4.2c}$$

where $s = \pm$ is the spin index. For instance, $s = +$ corresponds to an electron with a spin pointing along $-y$ in the quantum well. We also label the states with the index $\ell = \pm$, which denotes the two possible momenta (i.e., the two possible wave propagation directions) for fixed

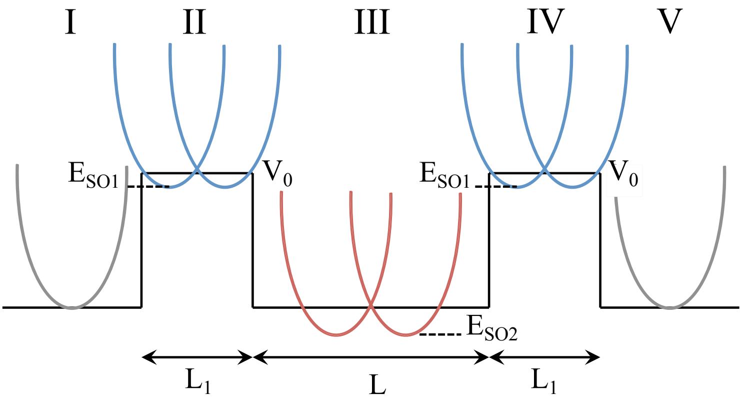

Figure 4.2: Energy diagram of our system. The QPCs are described with barrier potentials of height V_0 and width L_1 whereas the size of the central region is denoted with L. We also plot the energy spectra in each region. Due to the spin-orbit coupling the band structure undergoes a spin splitting and an energy downshift E_{SO}.

values of spin and energy E. The wave numbers read,

$$k_\ell^{(0)} \equiv k_\ell^I = k_\ell^V = \ell\sqrt{\frac{2m^*}{\hbar^2}E}\,, \tag{4.3a}$$

$$k_{\ell s}^{(1)} \equiv k_{\ell s}^{II} = k_{\ell s}^{IV} = \ell\sqrt{\frac{2m^*}{\hbar^2}(E+E_{SO1}-V_0)} - s\,k_{SO1}\,, \tag{4.3b}$$

$$k_{\ell s}^{(2)} \equiv k_{\ell s}^{III} = \ell\sqrt{\frac{2m^*}{\hbar^2}(E+E_{SO2})} - s\,k_{SO2}\,, \tag{4.3c}$$

with $E_{SOi} = m^*\alpha_i^2/(2\hbar^2)$ $(i = 1, 2)$ the downshift of the energy spectra due to the spin-orbit coupling, which also causes a horizontal band splitting Δk characterized by the momentum $k_{SOi} = m^*\alpha_i/\hbar^2$. Equations (4.3a), (4.3b), and (4.3c) depend on the energy of the incident electrons, which in the following we set equal to the Fermi energy E_F. Finally, we observe that both Eqs. (4.2a) and (4.2b) have the same spinor. Since the spin quantization axis in the reservoirs is not fixed, we select it parallel to the spin direction on the adjacent QPCs.

We are now in a position to solve the scattering problem in Fig. 4.2. We focus on the case $0 < E < V_0 - E_{SO1}$. This indicates that we are working with evanescent states in the QPC regions (II and IV).

Hence, $k_{\ell s}^{(1)}$ acquires an imaginary part but generally also possesses a real part. We emphasize that this differs from the case of tunnel barriers without spin-orbit coupling [70]. On the other hand, both $k_{\ell s}^{(0)}$ and $k_{\ell s}^{(2)}$ are always real numbers. The matching method allows us to determine all reflection and transmission amplitudes for an incoming electron, which we take as impinging from the left. The matching conditions are

$$\Psi(\epsilon) - \Psi(-\epsilon) = 0 \tag{4.4a}$$

$$\Psi'(\epsilon) - \Psi'(-\epsilon) = \frac{-im^*}{\hbar^2}\big[- \big(\alpha_2(\epsilon) - \alpha_2(-\epsilon)\big)\sigma_y \\ + \big(\alpha_1(\epsilon) - \alpha_1(-\epsilon)\big)\big(\sin\phi\sigma_z - \cos\phi\sigma_y\big)\big]\Psi(\epsilon)\,, \tag{4.4b}$$

where ϵ is a infinitesimal quantity around each interface. Equation (4.4a) is a statement of wave function continuity. Equation (4.4b) is derived from imposing flux conservation [114]. Notice that in the absence of spin-orbit interaction we recover the condition of continuity for the wave function derivative. In the presence of spin-orbit coupling, this condition must be generalized according to Eq. (4.4b).

Since transport is elastic, energy is conserved and the transmission $T^{s's}$ and reflection $R^{s's}$ probabilities depend on a given E. However, spin can be mixed after scattering and an incident electron with spin s is reflected or transmitted with spin s'. First, we analyze in Fig. 4.3 the main properties of $T^{s's}$ and $R^{s's}$ when we change the relative orientation between the QPCs and the QW spin-orbit fields. We choose the strength of the interaction in the QPCs (α_1) and in the QW (α_2) from Ref. [109]. We tune ϕ from 0 (spins parallel-oriented along the system) to $\pi/2$ (spin axes perpendicularly oriented). In Fig. 4.3(a) we observe that, independently of the value of ϕ, the electrons are reflected in the same spin state that the incoming one and that the reflection probability is roughly constant as a function of ϕ. We understand this effect as due to the spin orientation of electrons in regions I and II of Fig. 4.2, which is the same. In contrast, the transmission probability has both spin contributions for all values of ϕ except for the parallel configuration, for which $T^{-+} = 0$ since there exists no spin polarization. We also remark that as ϕ increases, i.e., as the injected spin direction is rotated from $-y$ to z, T^{-+} increases while T^{++} decreases since for higher ϕ the perpendicular component of the spin direction becomes larger and its contribution to the transmission

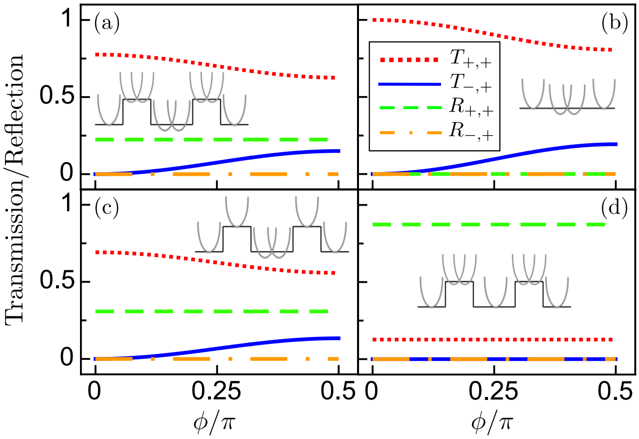

Figure 4.3: Transmission and reflection probabilities as a function of the relative angle ϕ between spin-orbit fields in the QPC and the QW. $T^{s's}$ ($R^{s's}$) in the transmission (reflection) probability from an electronic state of spin $s = \pm$ to spin $s' = \pm$ along the $-y$ direction. Parameters (a): $\alpha_1 = 20.16$ meV nm, $\alpha_2 = 25.18$ meV nm, $L = 440.83$ nm, $L_1 = 28.02$ nm, $V_0 = 4.94$ meV and $E_F = 4$ meV. In (b) we remove the tunnel barriers ($L_1 = 0$). In (c) [(d)] we cancel the spin-orbit interaction in the QPCs (QW): $\alpha_1 = 0$ ($\alpha_2 = 0$).

thus increases.

Let us further clarify the effects discussed above considering a few special cases. If we make $L_1 = 0$ (no tunnel barriers), the reflection probability is trivially zero, see Fig. 4.3(b), and the transmission functions follow the same behavior as in Fig. 4.3(a) for which L_1 is nonzero. In Fig. 4.3(c) we observe that if we turn off the spin-orbit coupling on the QPCs ($\alpha_1 = 0$), the transmission decreases as compared with the values in Fig. 4.3(a). As a consequence, we infer that the spin-orbit coupling enhances the transmission properties of our double-barrier system. This may seem counterintuitive—when the spin-orbit interaction is present, one would naively expect more scattering and smaller transmission. However, we stress that the spin-orbit coupling lowers the energy band bottom of the barrier, thus amplifying the role of the evanescent states (their characteristic decay length increases) and reducing consequently the reflection probability. Finally, when we take $\alpha_2 = 0$ (no spin-orbit interaction in the quantum well) all transport coefficients become independent of the angle ϕ [Fig. 4.3(d)] since the spin orientation in the central region is fixed. Furthermore, the reflection becomes higher due to the particular energy value, which lies around a resonance valley (see below).

Before proceeding, we notice that the case $\phi = 0$ can be considerably simplified. The second term in the right hand side of Eq. (4.1c) cancels out and we can write the projection of the Schrödinger equation $(\mathcal{H} - E)\Psi = 0$ onto the spinor pointing along the $-y$ direction as

$$\Big(- \frac{\hbar^2}{2m^*}\frac{d^2}{dx^2} - is\,(\alpha_1 + \alpha_2)\,\frac{d}{dx} + V_0 - E\Big)\Psi_s(x) = 0\,, \tag{4.5}$$

where α_1 and V_0 are nonzero in regions II and IV whereas α_2 is nonvanishing in region III only (Fig. 4.2). Now, using a similar gauge transformation as in Chapter 3 [see Eq. (3.8)]: $\Psi_s(x) = \Psi(x)\exp[-is\frac{m^*}{\hbar^2}\int dx'(\alpha_1 + \alpha_2)]$ we can recast Eq. (4.5) as

$$\left(-\frac{\hbar^2}{2m^*}\frac{d^2}{dx^2} + V_1 - V_2 - E\right)\Psi(x) = 0\,, \tag{4.6}$$

which is independent of the spin. Here, $V_1 = V_0 - E_{SO1}$ in regions II and IV and zero otherwise while $V_2 = E_{SO2}$ in region III. This potential corresponds to a double barrier of renormalized height V_1 and a quantum well of depth V_2 in the central region. Clearly, the spin-orbit coupling effectively lowers the top of the barrier potential as discussed earlier. Solving the scattering problem, we obtain a resonant condition that depends on all the parameters of our system,

$$k_{\ell s}^{(2)} L = n\pi + f(\alpha_1, \alpha_2, L_1)\,, \tag{4.7}$$

where $k_{\ell s}^{(2)}$ is the wave number in the central region [Eq. (4.3c)], $n = 1, 2\ldots$ labels the different resonances and $f(\alpha_1, \alpha_2, L_1)$ is a complicated function of α_1, α_2 and L_1 but independent of the QW length. The condition given by Eq. (4.7) can be numerically shown to hold also for the general case $\phi \neq 0$. However, in this case spin precession effects must be also taken into account.

Figure 4.4 shows how our system reacts to changes applied to the spin-orbit strength in the central region, α_2. The parallel configuration ($\phi = 0$) is plotted in Fig. 4.4(a), where we observe resonance

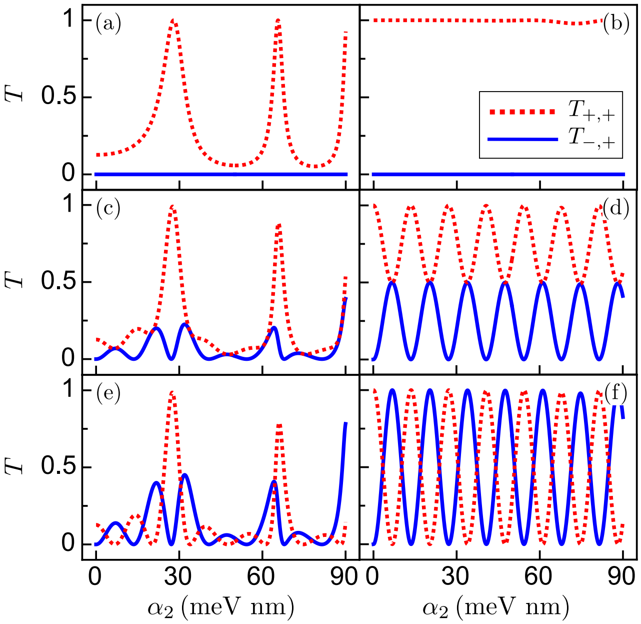

Figure 4.4: Transmission probabilities as a function of the spin-orbit strength in the central region, α_2, for $\alpha_1 = 20.16$ meV nm, $L = 440.8$ nm, $V_0 = 4.94$ meV and $E_F = 4$ meV. The left panels (a), (c) and (e) have $L_1 = 28.02$ nm while the right panels (b), (d) and (f) have $L_1 = 0$. The orientation angle is varied from top to bottom: $\phi = 0$ for (a) and (b), $\phi = \pi/4$ in (c) and (d), $\phi = \pi/2$ for (e) and (f).

peaks for certain values of spin-orbit interaction and a fixed Fermi energy. As the spin-orbit coupling increases, the quantum well becomes deeper and, as a consequence, there appear new quasibound states between the two barriers that fulfill Eq. (4.7). When the energy of the incident electron hits one of these states, the transmission probability is maximal. Therefore, the spin-orbit interaction acts in our system as a gate voltage by shifting the resonances of the quantum well [115]. Our system then behaves as an analog of a Fabry-Perot resonator tuned with a spin-orbit potential. Note that the resonances appear for T^{++} only since for $\phi = 0$ the spins are parallel and one obtains $T^{-+} = 0$ always. This can be better understood if we take $L_1 = 0$, in which case the double barrier potential disappears and we obtain an almost transparent system independently of the depth of the quantum well [Fig. 4.4(b)]. Here, the energy of the electron is sufficiently high that its wave is mostly unaffected by the well discontinuity. Only for strong enough spin-orbit strengths the transmission shows weak oscillations (Ramsauer effect). We also find that the off-diagonal transmission coefficient is zero. This originates from the fact in the parallel configuration the spin cannot be flipped, in agreement with the case $\phi = 0$ in Fig. 4.3(d).

In Figs. 4.4(c) and (d) we take $\phi = \pi/4$, i.e., the wave is spin polarized 45° with respect to $-y$. Let us first eliminate the double-barrier potential ($L_1 = 0$) and focus on the effects from the central region only, see Fig. 4.4(d). We observe that both T^{++} and T^{-+} are nonzero and oscillate out of phase. These oscillations are a consequence of the spin transistor effect predicted by Datta and Das [10], see Sec. 1.1. We find $T^{++} = 1$ and $T^{-+} = 0$ for $\alpha_2 = 0$ but then both transmissions become modulated as we increase the spin-orbit strength since the QW energy bands show a larger spin splitting $\Delta k = m^* \alpha_2/\hbar^2$. For certain values of α_2, T^{++} (T^{-+}) attains its minimum (maximum) value of 0.5. Importantly, the nature of these transmission oscillations fundamentally differs from the resonances in Fig. 4.4(a). To see this, we next obtain the spin-precession frequency from the relation [10]

$$T^{++} \propto \cos^2(\Delta k L) \tag{4.8}$$

This expression implies that the maximum condition is reached at $\Delta k L = n'\pi$ ($n' = 1, 2\ldots$). For the parameters of Fig. 4.4(d) this corresponds to $\alpha_2 \simeq 13.6n'$ meV nm.

More interestingly, we now turn on the double barrier potential and allow for the interplay between Fabry-Perot and Datta-Das oscillations. The superposition of the two effects can be seen in Fig. 4.4(c). We observe that (i) the resonance peaks for T^{++} become somewhat quenched and (ii) the off-diagonal coefficient T^{-+} shows an irregular series of oscillating peaks. The effect is more intense in the perpendicular configuration ($\phi = \pi/2$), see Fig. 4.4(e). Both transmissions oscillate now between 0 and 1 with opposite phases [Fig. 4.4(f)] and the combination of both types of oscillations yields the curves depicted in Fig. 4.4(e).

It is now natural to ask about the effect of tuning the QW length L. We show this in Fig. 4.5 for the same orientation angles as in

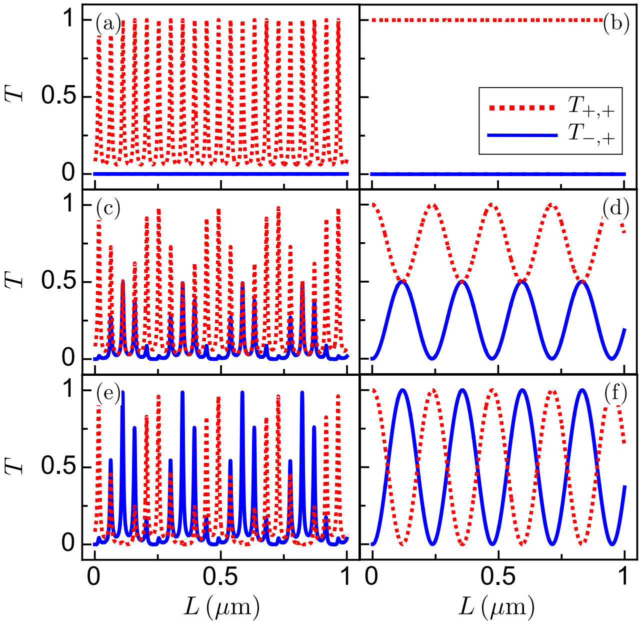

Figure 4.5: Transmission probabilities as a function of the central region width, L, for $\alpha_1 = 20.16$ meV nm, $\alpha_2 = 25.18$ meV nm, $V_0 = 4.94$ meV and $E_F = 4$ meV. The left panels (a), (c) and (e) have $L_1 = 28.02$ nm while the right panels (b), (d) and (f) have $L_1 = 0$. The orientation angle is varied from top to bottom: $\phi = 0$ for (a) and (b), $\phi = \pi/4$ in (c) and (d), $\phi = \pi/2$ for (e) and (f).

Fig. 4.4 but fixing the spin-orbit strength α_2. When $\phi = 0$, Fig. 4.5(a) presents for T^{++} narrowly spaced oscillations since as we increase the width of the central cavity there appear more internal modes that, at fixed values of L, are resonant with the incident wave (Fabry-Perot effect). The resonant condition from Eq. (4.7) implies that the transmission is peaked at $L \simeq (47.5n + 8.3)$ nm ($n = 1, 2\ldots$). For $\phi = 0$ spin flipping is not possible and $T^{-+} = 0$. When the constrictions are turned off ($L_1 = 0$), we have a completely open system and the transmission stays constant at its maximum value, see Fig. 4.5(b). As we increase the spin orientation angle [$\phi = \pi/4$ in Figs. 4.5(c) and (d) and $\phi = \pi/2$ in Figs. 4.5(e) and (f)], the spin transistor effect begins to contribute as we observe a spin precession for both T^{++} and T^{-+}, modulated by their characteristic frequency, namely, $L \simeq 237.6n'$ nm ($n' = 1, 2 \ldots$). We find that when $L_1 = 0$ (no tunnel barriers) the Fabry Perot resonances disappear and only the Datta-Das oscillations are present [Fig. 4.5(d) and (f)], as expected.

Remarkably, when both oscillation modes are present we find that the transmission becomes quasiperiodic [Fig. 4.5(c) and (e)]. This effect arises from the combination of at least two oscillations whose characteristic frequencies are incommensurate [116]. In our system, the Fabry-Perot frequency is given by $f_{FP} = \frac{1}{\pi}\sqrt{\frac{2m^*}{\hbar^2}E + k_{SO2}^2}$ whereas that of the spin precession motion is expressed as $f_{sp} = 2k_{SO2}/\pi$. Clearly, its ratio f_{FP}/f_{sp} is quite generally an irrational number. In related systems, quasiperiodic oscillations have been predicted to occur in double quantum dots with incommensurate capacitance couplings [117] and in ac-driven supelattices where the ratio between the ac frequency and the internal frequency is not a rational number [118]. Importantly, in our case the origin of both oscillations is purely quantum (wave interference and spin precession).

4.3 Quasi-one dimensional case

The above discussion demonstrates that two types of transmission oscillations can coexist in a double-barrier spin-orbit coupled resonant tunneling diode. However, the results were strictly limited to the 1D case. We now consider the more realistic situation of a double QPC embedded in a quantum wire of finite width. The problem is not a mere extension that takes into account transverse channels since these channels become coupled via the Rashba intersubband mixing potential. This term causes spin-flip transitions between adjacent channels and generally destroys the spin coherent oscillations [119]. Furthermore, it yieds Fano lineshapes [85] that dramatically alter the conductance curves [85, 120–122, 115]. We note that there exists another type of intersubband spin orbit coupling potential that occurs in coupled wells with two subbands [123]. Here, we consider the case of an intense confinement in the growth direction such that only the lowest subband is populated. We consider the planar waveguide formed in a 2D electron gas lying on the x–y plane as in Fig. 4.1. This system was also studied in Chapter 3. The difference is that here we consider QPCs as spin injector and detector. In the numeri-

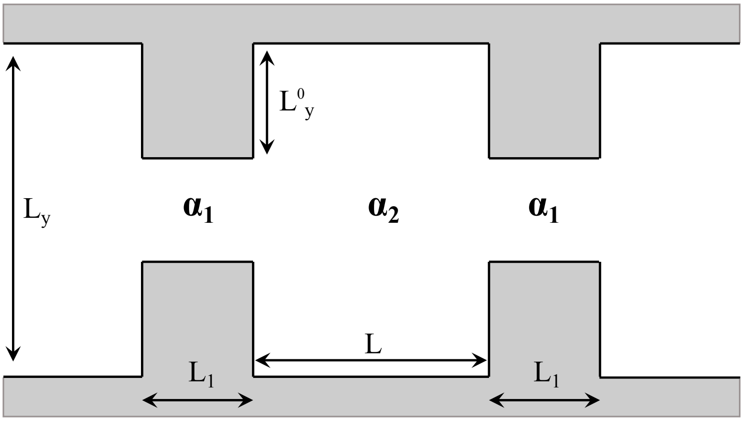

Figure 4.6: Sketch of the double quantum point contact system with a finite width L_y. Electrons can move in the white areas whereas forbidden regions are depicted in grey. The height of the constriction barriers is L_y^0. The rest of the parameters are defined as in the purely 1D case (Fig. 4.2).

cal simulations, we consider a hard-wall confinement potential along y and two square QPCs in the x direction. The system parameters are depicted in Fig. 4.6.

We take a given quantization axis $\hat{n}$ for the spin in the left and right contacts. The spin eigenfunctions are then denoted with $\chi_s(\eta)$, with $s = \pm$ the eigenstate label and $\eta = \uparrow, \downarrow$ the discrete variable. The full wave function $\Psi(x, y, \eta)$ is expanded in spin channels $\psi_s(x, y)$ as

$$\Psi(x, y, \eta) = \sum_{s=\pm} \psi_s(x, y)\chi_s(\eta)\,. \tag{4.9}$$

Projecting the Schrödinger equation on the spin basis, we obtain coupled channel equations,

$$\begin{aligned}
&\left(-\frac{\hbar^2\nabla^2}{2m}+V(x,y)\right)\psi_s(x,y)\\
&-\frac{i\hbar}{2}\sum_{s'}\langle s|\sigma_y|s'\rangle\left(V_A(x)\frac{\partial}{\partial x}+\frac{\partial}{\partial x}V_A(x)\right)\psi_{s'}(x,y)\\
&-\frac{i\hbar}{2}\sum_{s'}\langle s|\sigma_z|s'\rangle\left(V_B(x)\frac{\partial}{\partial x}+\frac{\partial}{\partial x}V_B(x)\right)\psi_{s'}(x,y)\\
&\qquad\qquad+\frac{i\hbar}{2}\sum_{s'}\langle s|\sigma_x|s'\rangle\,V_A(x)\frac{\partial}{\partial y}\,\psi_{s'}(x,y)=0\;,
\end{aligned}\tag{4.10}$$

where the potentials $V_A(x)$ and $V_B(x)$ are responsible for the coupling between the different spin channels $s=\pm$. In general, the Pauli-matrix elements in Eq. (4.10) depend on $\hat{n}$. To connect with the 1D case discussed in Sec. 4.2 we take $\hat{n}=-\hat{y}$, which makes the σ_y term diagonal, but those with σ_x and σ_z remain non diagonal. Coupling between opposite spin states is, therefore, always present in the quasi-1D case when $(V_A, V_B)\neq 0$ [52, 124].

In Eq. (4.10) the potentials V_A and V_B read

$$V_A(x)=\alpha_1\cos\phi\,\mathcal{P}_1(x)+\alpha_2\mathcal{P}_2(x)+\alpha_1\cos\phi\,\mathcal{P}_3(x)\,,\tag{4.11}$$

$$V_B(x)=-\alpha_1\sin\phi\,\mathcal{P}_1(x)-\alpha_1\sin\phi\,\mathcal{P}_3(x)\,,\tag{4.12}$$

where the projectors $\mathcal{P}_i(x)$ partition the x domain in regions $i=1$ (left QPC), $i=2$ (QW) and $i=3$ (right QPC). These two potentials yield qualitatively different spin-flip couplings, since V_B only appears with $\partial/\partial x$, while V_A appears with both $\partial/\partial x$ and $\partial/\partial y$. As before, ϕ is the angle defining the relative orientation of the Rashba fields. Notably, $V_B(x)$ vanishes with $\phi=0$ and then, for quantization axis along y, the only spin-flip coupling in Eq. (4.10) is via the last term depending on $\partial/\partial y$. To be effective, this spin-flip coupling requires that at least two transverse modes (differing in the nodes along y) are propagating in the asymptotic leads [85]. Otherwise, as we show below, there is no spin-flip when $\hat{n}$ lies along y.

Equation (4.10) is solved with the quantum-transmitting boundary method [86] on a uniform grid. As discussed in Sec. 3.1 this algorithm gives the transmission probability of an incoming electron from the left to the right side. In Fig. 4.7 we show the transmission probability as a function of the middle spin-orbit strength α_2. We recall

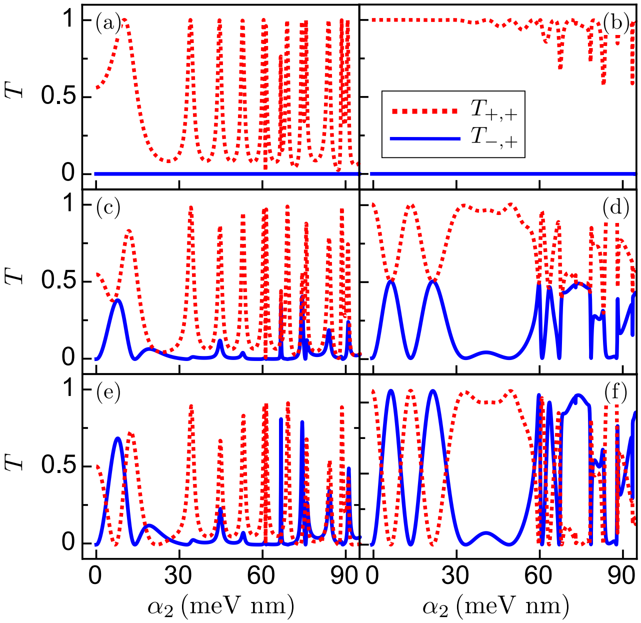

Figure 4.7: Transmission probabilities for a quasi-one dimensional double quantum point contact system as a function of the spin-orbit strength in the central region, α_2. Parameters: $\alpha_1 = 20.16$ meV nm, $L = 440.8$ nm, $L_1 = 10.91$ nm, $L_y^0 = 39.29$ nm, $L_y = 87.29$ nm and $E_F = 4$ meV. The left panels (a), (c) and (e) have $L_1 = 10.91$ nm while the right panels (b), (d) and (f) have $L_1 = 0$. The orientation angle is varied from top to bottom: $\phi = 0$ for (a) and (b), $\phi = \pi/4$ in (c) and (d), $\phi = \pi/2$ for (e) and (f).

that the transmission is expressed in the $-y$ direction basis. Similarly to Fig. 4.4 we distinguish the case with the constrictions (left panels) from the case without the QPCs (right panels). For $\phi = 0$ [Fig. 4.7(a)] we quench the spin precession oscillations since the injected spins are parallel to the Rashba field. Then, the cross transmission T^{-+} vanishes identically. The resonant tunneling peaks qualitatively agree with the 1D case [cf. Fig. 4.4(a)]. Likewise, the Ramsauer oscillations that arise when the QPCs are absent [Fig. 4.7(b)] are visible at large values of α_2 [cf. Fig. 4.4(b)]. The agreement in both cases is good for small values of α_2. This is reasonable since Rashba intersubband coupling is negligible if $\alpha_2 \ll \hbar^2/mL_y$ [10]. For larger α_2 we observe in Fig. 4.7(b) sharp dips that originate from the Fano-Rashba effect [85] and that are unique to quasi-one dimensional waveguides with nonuniform spin-orbit coupling as in our case. Strikingly enough, as α_2 increases we detect in Fig. 4.7(a) more resonant peaks than in the strict 1D case. We explain this effect as follows. For $\alpha_1 = \alpha_2 = 0$ the cavity works as a resonator with multiple resonances. If the cavity is closed, the bound levels can be described with a pair of natural numbers (n_1, n_2) since its potential corresponds to a 2D infinite well [125]. To a good approximation, the electronic scattering when the cavity is open obeys a conservation law that fixes the transversal component of motion [126]. Accordingly, n_2 is conserved upon traversing the cavity and the transmission shows less peaks than bound states in the closed cavity. In the presence of spin-orbit coupling, the conservation law does not have to hold and more resonances then emerge.

For $\phi = \pi/4$ the injected electrons are spin rotated with regard to the α_2 field and spin precession oscillations of the Datta-Das type are expected. This can be more distinctly seen in Fig. 4.7(d), where the QPC widths are set to zero. Up to $\alpha_2 \simeq 30$ meV nm the oscillations are smooth as in Fig. 4.4(d). For larger α_2 the subband mixing potential starts to play a significant role. As a consequence of the spin mixing induced by the p_y term, the precession oscillations become irregular [119] and the transmission curves can no longer be determined by a single frequency. When combined with the Fabry-Perot oscillations, the transmission lineshapes are transformed into nonharmonic functions of α_2 [see Fig. 4.7(c)] and our previous 1D analysis in terms of quasiperiodic oscillations does not hold. For completeness, we also show the case $\phi = \pi/2$ for which the Data-Das frequency is higher (the spins are injected perpendicular to the Rashba field) but the spin oscillations turn out to be nonuniform as α_2 grows as illustrated in Fig. 4.7(f). The overall transmission curves [Fig. 4.7(e)] qualitatively follow the pattern observed in the case $\phi = \pi/4$.

In Fig. 4.8 we analyze the dependence with the central cavity width L. We set the spin-orbit strenght α_2 to a moderate value to highlight the effects due to the Rashba intersubband coupling term. Figure 4.8(a) shows the transmission for $L_1 = 0$ and $\phi = \pi/2$. This implies that only oscillations from the spin dynamics are present since resonant tunneling effects are not allowed. Unlike Fig. 4.5(f) here

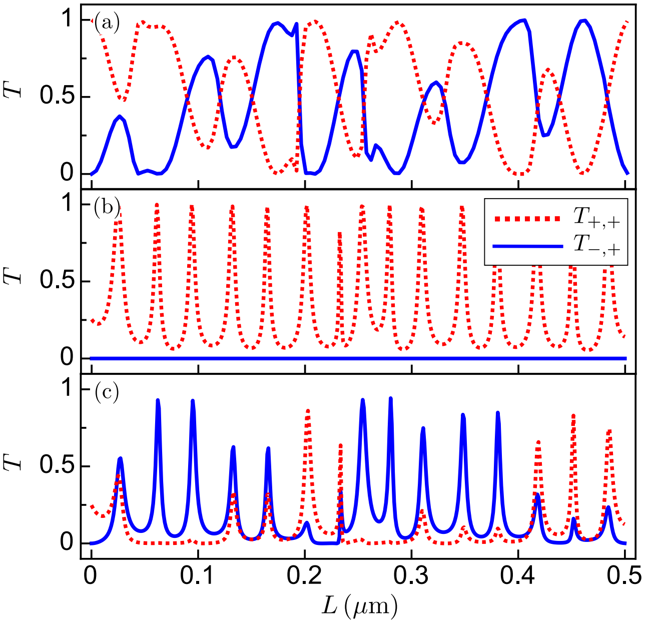

Figure 4.8: Transmission probabilities for a quasi-one dimensional double quantum point contact system as a function of the width of central region, L. Parameters: $\alpha_1 = 20.16$ meV nm, $\alpha_2 = 65.47$ meV nm, $L_y^0 = 39.29$ nm, $L_y = 87.29$ nm and $E_F = 4$ meV. Additionally, we set in (a) $L_1 = 0$ nm and $\phi = \pi/2$, in (b) $L_1 = 10.91$ nm and $\phi = 0$, and in (c): $L_1 = 10.91$ nm and $\phi = \pi/2$.

the oscillations are not uniform for both transmission probabilities, T^{++} and T^{-+}. The Fabry-Perot peaks are more regular as shown in Fig. 4.8(b), where L_1 is nonzero and $\phi = 0$ in order to forbid spin precession oscillations. This suggests that the Rashba intersubband potential has a stronger impact on the Datta-Das oscillations than on the Fabry-Perot peaks. In Fig. 4.5(c) we show characteristic transmission curves for nonzero L_1 and $\phi = \pi/2$, in which case both oscillation modes come into play. As compared to the 1D case in Fig. 4.5(e) the oscillations are now more intricate: their amplitudes strongly fluctuate with increasing L and their frequency cannot be described in terms of combinations of individual frequencies.

In order to complete the analysis of our system we present in

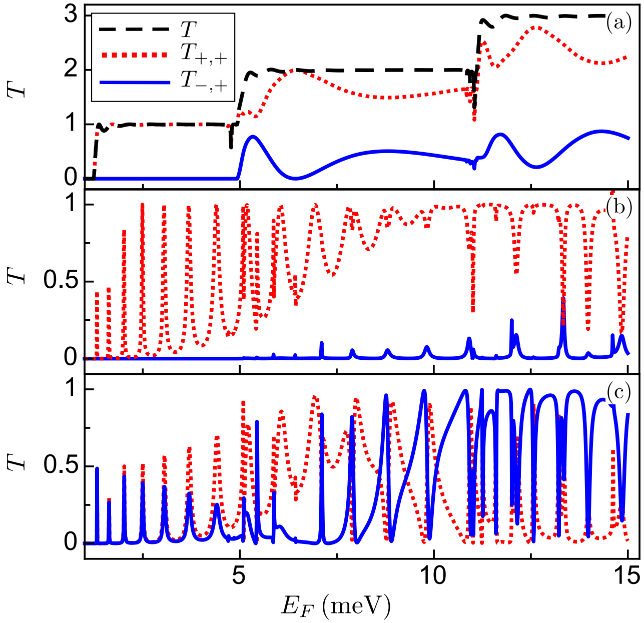

Figure 4.9: Transmission probabilities for a quasi-one dimensional double quantum point contact system as a function of the position of the Fermi level, E_F. Parameters: $\alpha_1 = 20.16$ meV nm, $\alpha_2 = 65.47$ meV nm, $L_y^0 = 21.82$ nm, $L_y = 87.29$ nm and $L = 440.8$ nm. Additionally, we set in (a) $L_1 = 0$ nm and $\phi = \pi/2$, in (b) $L_1 = 10.91$ nm and $\phi = 0$, and in (c): $L_1 = 10.91$ nm and $\phi = \pi/2$.

Fig. 4.9 the transmission probability as a function of the Fermi energy for the same parameters as above. In Fig. 4.9(a) we consider the case without the QPCs ($L_1 = 0$ nm) and apply a spin-orbit interaction in the central region such that its direction lies orthogonal to that of the leads ($\phi = \pi/2$). We find an approximate transmission quantization of $T = T^{++} + T^{-+}$ (black line) whenever a new propagating channel opens up as the Fermi energy surpasses the values $E_n = \hbar^2\pi^2 n^2/2m^* L_y^2$ with $n = 1, 2\ldots$ (recall that the confinement along the transverse direction is described with a hard-wall potential). We also observe in Fig. 4.9(a) the spin dependence due to the spin-orbit interaction in the middle region (solid red and dashed blue lines). The Fabry-Perot peaks form when $\phi = 0$ and $L_1 \neq 0$, see

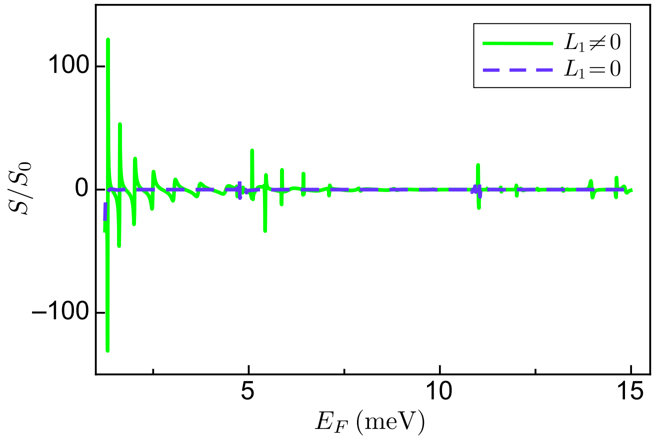

Figure 4.10: Seebeck coefficient as a function of the position of the Fermi level, E_F. Parameters: $\alpha_1 = 20.16$ meV nm, $\alpha_2 = 65.47$ meV nm, $L_y^0 = 21.82$ nm, $L_y = 87.29$ nm, $L = 440.8$ nm, $L_1 = 10.91$ nm, $\phi = \pi/2$ and $T_0 = 1$ K.

Fig. 4.9(b). Here, the transmission is zero until the Fermi energy is such that the first propagating state is allowed in the leads, which corresponds to $E_F > E_1 = 1.23$ meV. At the same time, in the QPCs we have evanescent states below the energy value $E_1^{QPC} = 4.93$ meV. Then, the resonances ranging between these two energies are due only to tunneling transmission across the QPCs. The second channel in the leads opens up at $E_2 = 4.93$ meV but the transmission does not exceed 1 because we have just one open channel in the constrictions. When the third channel in the leads opens up, $E_F > E_3 = 11.10$ meV, we observe dips in the diagonal transmission probability which correlate with peaks in the off-diagonal transmission. This effect originates from the coupling between propagating states in the system and quasibound states in the cavity. Finally, Fig. 4.9(c) shows the combination of Fabry-Perot peaks and Datta-Das oscillations when the spin-orbit fields are perpendicular. Its behavior is similar to the Fabry-Perot-Datta-Das oscillations discussed as a function of the spin-orbit coupling [Fig. 4.7(e)] and cavity length [Fig. 4.8(c)].

Once we have studied the transmission probability in depth, it is natural to ask what happens with the electric and thermoelectric conductance and the Seebeck coefficient in analogy with the previous chapters. In the quasi-1D case the electric conductance is just e^2/h times the transmission probability [see Eq. (3.15)] while the thermoelectric conductance can be written in terms of its energy derivative [see Eq. (3.24b)]. Then, we expect that since T has share peaks as we vary E_F (see Fig. 4.9) the thermoelectric conductance will present strong modulations. In order to summarize our results, we determine the Seebeck coefficient from the Mott formula [see Eq. (2.29)] which, taking into account that our system is nonmagnetic, can be written as

$$S = -S_0 \frac{k_B T_0 \pi^2}{3} \frac{\partial \ln T}{\partial E_F}\,, \tag{4.13}$$

where $S_0 = k_B/e$.

In Fig. 4.10 we show S as a function of E_F in the perpendicular case for $L_1 \neq 0$ (solid line) and $L_1 = 0$ (dashed line). The thermopower obtained when the QPCs are not active ($L_1 = 0$) is close to zero from most of the E_F values. Only at certain values of the Fermi energy we observe small deviations. If we observe the dashed line of Fig. 4.9(a), we note that it takes a constant value and only increases its value when a new propagating channel opens up (these are the same energies for which we observed deviations in S). Now we include the QPCs (solid line in Fig. 4.10) and observe how S shows dramatic sign changes at low energies. This is easy to understand if we consider the fact that at these energies the transmission probability has very narrow peaks that rapidly decay to zero [see Fig. 4.9(c)]. For higher energies the peaks and dips have lower amplitudes because at this energies the transmission probability never reaches zero and its variations are smoother.

4.4 Conclusions

In this chapter, we have studied the transport properties of a semiconductor layer with two quantum point contacts in series and a spatially inhomogeneous spin-orbit interaction applied on the QPCs and central region. In the strict one-dimensional limit, where we have a double barrier potential modeling the two QPCs, we have observed transmission oscillations as a function of the relative orientation between the QPC effective magnetic fields and the spin-orbit interaction in the well, the strength of the spin-orbit coupling and the width of the middle cavity. We stress that, depending on the direction of the spin polarization in the QPC regions, the transitions are dominated by processes that conserve or flip the spin direction. We have also analysed the combined effect of Datta-Das and Fabry-Perot oscillations and obtained their characteristic frequencies. We have found that modifying the strength of the spin-orbit coupling and the width of central region we can control the transmission probability for each spin. Finally, our analysis of the quasi-one-dimensional case, is important because it quantifies the role of spin-orbit intersubband coupling effects in both the Fabry-Perot and the Datta-Das oscillation modes.

5. Interacting quantum capacitor

Real-time manipulation of electrons is one of the greatest achievements in modern nanoelectronics [127–129]. The characteristic setup comprises a submicron-sized cavity or quantum dot (for a short introduction to quantum dots, see Sec. 1.3.2.3) tunnel coupled to a reservoir through a QPC. Then, a time dependent driving voltage is applied to a electrostatically coupled metallic gate placed on top of the dot. As a consequence, dc transport is impossible and the system response is purely dynamical[1]. The low-frequency admittance measured with cryogenic low-noise amplifiers can be understood from the serial combination of a charge relaxation resistance and a quantum capacitance [130, 131]. It turns out that in the linear regime (small ac amplitudes) the charge relaxation resistance is quantized for a single spin-polarized channel [132], a theoretical prediction that was experimentally confirmed [127]. For drivings with larger amplitudes (nonlinear regime), the system works as an on-demand single-electron source [128], in analogy with single-photon sources [133, 134], with alternate sequences of electron emission and absorption during a driving period in the fast (GHz) regime. When the voltage pulse has a Lorentzian shape [135–138], recent progress has shown that the holes can be efficiently removed from the stream of excitations when the pulse is applied to an Ohmic contact [139]. These phenomena imply the observation of quantized currents ensured by charge quantization, which might be useful in metrology applications [140] and quantum computation designs [141–143].

Now, tunneling electrons feel repulsive interactions that yield Coulomb blockade, a prominent effect in small capacitance conductors which manifests itself as an increased resistance of a quantum dot junction at finite bias voltages [144]. In fact, the effect is quite ubiquitous in nanoscale systems and arises not only in quantum dots but also in carbon nanotubes [145], molecular transistors [146], and optical lattices [147]. Therefore, it is natural to investigate the role of Coulomb blockade effects in single-electron sources. This is the goal we want to accomplish in this chapter.

---

[1] The contents of this chapter are based on M. I. Alomar, Jong Soo Lim and David Sánchez, Phys. Rev. B **94**, 165425 (2016).

We begin by noticing that electron-electron interactions have been widely analyzed in the quantum RC circuit [148–165]. However, these works have mostly focused on the linear regime (for an exception, see Ref. [161]). The nonlinear regime is interesting because both the capacitance and the charge relaxation resistance acquire an explicit time dependence [166]. This result was found for noninteracting electrons. Here, we give full expressions for the capacitive and the dissipative parts of the current valid in the case of strong interactions that lead to Coulomb blockade effect. We predict that this effect should be visible as a splitting of the dynamical current peaks for both emitted and absorbed electrons. Importantly, the simultaneous emission of pairs of electrons in the noninteracting case is modified to a subsequent emission of two electrons.

The energy diagram of our system is sketched in Fig. 5.1. We consider a single-level quantum dot (energy ε_0) coupled to a Fermi sea of electrons (Fermi energy E_F). The coupling region between the dot and the reservoir is typically a pinched-off quantum point contact (see Sec. 1.3.2.2) that we depict in Fig. 5.1 with a tunnel barrier. This part represents the resistive component of the quantum circuit, through which electrons can hop on and off the dot. The position of ε_0 can be tuned with a dc gate potential applied to the point contact [128] (not shown in Fig. 5.1). Additionally, the dot is coupled to a nearby gate terminal with an externally applied harmonic potential $\varepsilon_{ac}(t)$. This is the capacitive part of the RC circuit. Finally, a charging energy U is required to charge the dot with two electrons having opposite spins. This situation is experimentally relevant for small dots. The case of large dots with many quantum levels was treated in Ref. [148], where a Hartree-Fock approximation was employed to account for Coulomb interactions and screening effects. Here, we consider the Anderson model with a single level and a constant interaction energy. This model has been successfully applied to the Fermi liquid limit connected to the Korringa-Shiba relation [157],

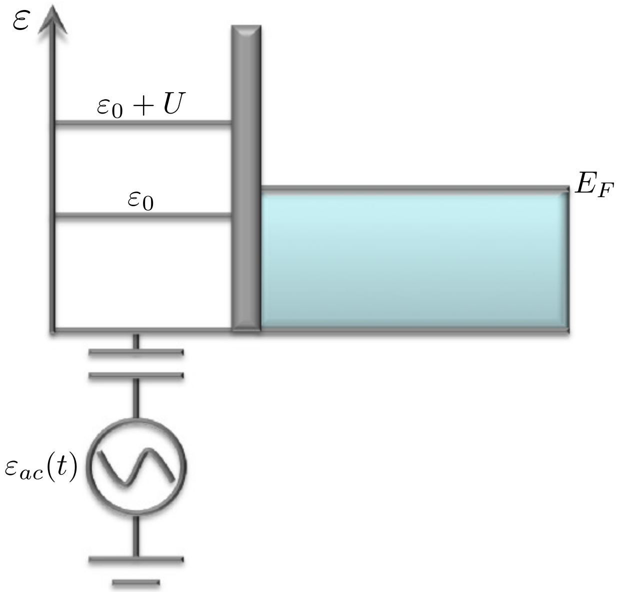

Figure 5.1: Schematic representation of a single-electron source comprising a single-level quantum dot coupled capacitively to an ac oscillating signal, $\varepsilon_{ac}(t)$. The dot can exchange electrons with an attached reservoir (Fermi energy E_F) via a tunnel barrier. The dot energy level is denoted with ε_0 and Coulomb repulsion is given by the charging energy U.

unveiling strong departures of the charge relaxation resistance from universality [158].

5.1 Theoretical model

Our theoretical discussion starts with the Anderson Hamiltonian of a mesoscopic capacitor, $H = H_R + H_T + H_D$, where H_R describes the single reservoir, H_T is the tunnel coupling between the reservoir and the quantum dot (QD) and H_D models the QD:

$$H_R = \sum_{k\sigma} \varepsilon_k c^\dagger_{k\sigma} c_{k\sigma} \,, \tag{5.1a}$$

$$H_T = \sum_{k\sigma} \left(V_k^* d^\dagger_\sigma c_{k\sigma} + V_k c^\dagger_{k\sigma} d_\sigma \right) \,, \tag{5.1b}$$

$$H_D = \sum_{\sigma} \varepsilon_\sigma(t) d^\dagger_\sigma d_\sigma + U n_\uparrow n_\downarrow \,, \tag{5.1c}$$

with $n_\sigma = d^\dagger_\sigma d_\sigma$ the occupation number operator and $\varepsilon_\sigma(t) = \varepsilon_\sigma + \varepsilon_{ac}(t)$ including both the QD energy level, $\varepsilon_\sigma = \varepsilon_0 + \sigma\Delta_Z/2$ (here Δ_Z denotes the Zeeman splitting due to interaction with an external magnetic field), and the oscillating potential applied to the gate, $\varepsilon_{ac}(t) = \varepsilon_{ac} \cos \Omega t$, where ε_{ac} is the ac amplitude and Ω is the driving frequency. We emphasize that ε_0 and $\varepsilon_{ac}(t)$ can be tuned independently, as experimentally demonstrated [128], with a dc and ac voltage, respectively, applied to the quantum point contact and the gate electrode: $\varepsilon_0 = -eV_{\text{QPC}}$ and $\varepsilon_{ac} = -eV_g$. This allows us to treat the position of the QD level relative to the Fermi energy and the ac amplitude as separate parameters in our calculations. The sinusoidal drive considered here is convenient because the derivative of the drive is proportional to the frequency and thus easily Fourier decomposed. Different drives such as a step function do not show this nice property and add mathematical difficulties to the formalism. Hence, we restrict ourselves to the monochromatic case.

In the Hamiltonian H, σ labels the electron spin and hereafter we consider the nonmagnetic case ($\Delta_Z = 0$). However, the magnetic ($\Delta_Z \neq 0$) situation can be easily included in our model but we focus on the spin-degenerate case. This is an important difference with the samples of Refs. [127, 128], which operate in the quantum Hall regime to achieve single-channel propagation with no spin degeneracy.

In Eq. (5.1a), ε_k represents the reservoir energy dispersion with momentum k and $c^\dagger_{k\sigma}(c_{k\sigma})$ creates (annihilates) a conduction band electron. The tunnel hamiltonian given by Eq. (5.1b) contains the tunnel amplitude V_k and the fermionic operator $d^\dagger_\sigma(d_\sigma)$, which creates (annihilates) a localized electron in the dot. Finally, $U = e^2/(C_g+C_R)$ in Eq. (5.1c) is the charging energy, which we also take as a tunable parameter depending on the capacitive strengths with the coupled gate, C_g, and eventually with the reservoir, C_R.

The time dependent field $\varepsilon_{ac}(t)$ induces a purely dynamical charge current $I_R(t)$ that can be measured at the reservoir. Since H commutes with the total charge, I_R is determined from the change rate of the dot occupation, $I(t)$:

$$I_R(t) + I(t) = 0\,, \tag{5.2}$$

where $I(t) = e\partial_t \sum_\sigma \langle d_\sigma^\dagger d_\sigma\rangle(t)$ and $I_R(t) = e\partial_t \sum_{k,\sigma}\langle c_{k\sigma}^\dagger c_{k\sigma}\rangle(t)$ with e the unit of charge. Here, ∂_t denotes the time derivative. Equation (5.2) thus represents the electronic charge conservation. In what follows, we focus on $I(t)$ because it can be directly expressed in terms of the QD Green's function without further manipulation, as shown below. The physical current I_R (since it amounts to a flux) can then be obtained immediately from Eq. (5.2).

Let $G_\sigma^<(t,t') = i\langle d_\sigma^\dagger(t') d_\sigma(t)\rangle$ be the lesser Green's function [167, 168] for the dot operators. Clearly, the QD occupation $\langle n_\sigma(t)\rangle = \langle d_\sigma^\dagger(t) d_\sigma(t)\rangle$ can be written in terms of the lesser Green's function. The current is hence calculated as

$$\begin{aligned} I(t) = e\partial_t \sum_\sigma \langle n_\sigma(t)\rangle &= e\partial_t \sum_\sigma \Big(- iG_\sigma^<(t,t)\Big) \\ &= e\partial_t \sum_\sigma \int \frac{d\varepsilon}{2\pi i} G_\sigma^<(t,\varepsilon)\,, \end{aligned} \tag{5.3}$$

where in the last line we express the lesser dot Green's function in a mixed time energy notation [169, 170]. This representation is especially useful for nonstationary scattering problems in the adiabatic limit [171, 172]. Its connection with the original double time picture and the corresponding Fourier transform is discussed in App. F.

Our regime of interest here is the adiabatic case (small frequency Ω) but arbitrary values of the ac amplitude ε_{ac}. In that case, the Green's function is expected to display small deviations around a frozen state in time characterized by a stationary scattering matrix with time dependent parameters. This approximation is good when $\hbar\Omega$ is the smallest energy scale of our problem. For a prototypical RC circuit [127], $\hbar\Omega \simeq 0.2$ μeV, which is at least fifty times smaller than the tunnel coupling $\Gamma \simeq 10$ μeV. Therefore, the electron interacts only weakly with the ac potential before tunneling into or out of the QD. The frequency expansion reads,

$$G_\sigma^<(t,\varepsilon) = G_\sigma^{<,f}(t,\varepsilon) + \hbar\Omega G_\sigma^{<,(1)}(t,\varepsilon) + O(\Omega^2)\,, \tag{5.4}$$

where the superscript f denotes the frozen approximation and (1) implies the first order in driving frequency Ω. Second-order terms and beyond are neglected, which suffices for the purposes of this work. (Inductive-like effects have been studied in Ref. [173]). We stress that the zeroth-order (frozen) term in Ω is still time dependent. No assumption has been made on the strength of the amplitude, which can be arbitrarily large, driving the system into the nonlinear regime.

Substituting Eq. (5.4) into Eq. (5.3), we find similar expansions for the occupation and the current,

$$\begin{aligned} I(t) &\simeq e\partial_t \sum_\sigma \int \frac{d\varepsilon}{2\pi i}\Big(G_\sigma^{<,f}(t,\varepsilon) + \hbar\Omega G_\sigma^{<,(1)}(t,\varepsilon)\Big) \\ &= e\partial_t \sum_\sigma (\langle n_\sigma(t)\rangle^f + \langle n_\sigma(t)\rangle^{(1)}) \\ &= I^{(1)}(t) + I^{(2)}(t)\,. \end{aligned} \tag{5.5}$$

From the definition given by Eq. (5.3), it follows that the leading order for the current is first order in Ω. To be consistent, we therefore keep the current terms in Eq. (5.5) up to second order in Ω. The physical implication says that $I^{(1)}$ represents a capacitive-like contribution while $I^{(2)}$ is understood as a dissipative component [166].

This interpretation can be substantiated by introducing a quantum RC circuit model (a capacitor and a resistor in a series with an applied ac potential) with time dependent capacitance and resistance functions,

$$eI(t) \simeq -C_\partial(t)\partial_t\varepsilon_{ac}(t) + R_\partial(t)C_\partial(t)\partial_t(C_\partial(t)\partial_t\varepsilon_{ac}(t))\,. \tag{5.6}$$

This relation is valid at low frequency for both the linear and the nonlinear regimes. In Eq. (5.6) $C_\partial(t)$ is the differential capacitance and $R_\partial(t)$ the differential resistance. Both depend on time because they constitute a generalization of the linear-response quantum capacitance C_q and charge relaxation resistance R_q [130] to the nonlinear ac transport regime [166]. Combining Eq. (5.5) with Eq. (5.6), we can find expressions for $C_\partial(t)$ and $R_\partial(t)$. Therefore, our goal is first to obtain an equation for $G_\sigma^<(t,\varepsilon)$ in the presence of Coulomb interactions and oscillating voltages.

5.2 Decoupling scheme

The temporal evolution of the dot Green's function is determined from the commutator of d_σ with H (Heisenberg equation of motion). It is convenient to consider the time-ordered Green's function $G_\sigma(t,t') \equiv \langle\langle d_\sigma, d_\sigma^\dagger\rangle\rangle(t,t') = -i\langle \mathcal{T} d_\sigma(t) d_\sigma^\dagger(t')\rangle$. After some straightforward steps, we find that the time-ordered Green's function satisfies the integral (Dyson) equation

$$\begin{aligned} G_\sigma(t,t') = \mathrm{g}_\sigma(t,t') &+ \int \frac{ds}{\hbar}\, G_\sigma(t,s)\varepsilon_{ac}(s)\mathrm{g}_\sigma(s,t') \\ &+ \int \frac{ds}{\hbar} \int \frac{ds'}{\hbar}\, G_\sigma(t,s')\Sigma_0(s',s)\mathrm{g}_\sigma(s,t') \\ &+ U \int \frac{ds}{\hbar}\, \langle\langle d_\sigma, d_\sigma^\dagger n_{\bar\sigma}\rangle\rangle(t,s)\mathrm{g}_\sigma(s,t')\,, \end{aligned} \tag{5.7}$$

where $\bar\sigma = -\sigma$. $\Sigma_0(t,t') = \sum_k |V_k|^2 \mathrm{g}_k(t,t')$ is the tunnel self-energy with $\mathrm{g}_{k(\sigma)}(t,t')$ the isolated reservoir (dot) Green's function in the absence of the ac driving potential. The retarded/advanced and lesser Green's functions can then be obtained from the Langreth's analytic continuation rules [168].

To consider the effect of U, we now generate an additional integral equation for the correlator $\langle\langle d_\sigma, d_\sigma^\dagger n_{\bar\sigma}\rangle\rangle(t,t')$ in Eq. (5.7):

$$\begin{aligned} \langle\langle d_\sigma, d_\sigma^\dagger n_{\bar\sigma}\rangle\rangle(t,t') &= \langle n_{\bar\sigma}(t)\rangle\, \mathrm{g}_\sigma(t,t') \\ &+ \int \frac{ds}{\hbar}\, \langle\langle d_\sigma, d_\sigma^\dagger n_{\bar\sigma}\rangle\rangle(t,s)\varepsilon_{ac}(s)\mathrm{g}_\sigma(s,t') \\ &+ \sum_k \int \frac{ds}{\hbar}\, \Big(V_k \langle\langle d_\sigma, c_{k\sigma}^\dagger n_{\bar\sigma}\rangle\rangle(t,s) + V_k \langle\langle d_\sigma, d_\sigma^\dagger c_{k\bar\sigma} d_{\bar\sigma}\rangle\rangle(t,s) \\ &\qquad - V_k^* \langle\langle d_\sigma, d_\sigma^\dagger d_{\bar\sigma}^\dagger c_{k\bar\sigma}\rangle\rangle(t,s)\Big)\, \mathrm{g}_\sigma(s,t') \\ &+ U \int \frac{ds}{\hbar}\, \langle\langle d_\sigma, d_\sigma^\dagger n_{\bar\sigma}\rangle\rangle(t,s)\mathrm{g}_\sigma(s,t')\,, \end{aligned} \tag{5.8}$$

where three new correlation functions arise. Since we are interested in the Coulomb blockade regime, we can neglect charge and spin excitations. This truncated equation of motion approach is good in the weak tunneling regime or for not very low temperatures, in which case Kondo correlations can be disregarded [174]. As a consequence, we neglect the spin-flip correlators in Eq. (5.8):

$$\langle\langle d_\sigma, d_\sigma^\dagger d_{\bar\sigma}^\dagger c_{k\bar\sigma}\rangle\rangle(t,s) \simeq 0\,, \tag{5.9a}$$

$$\langle\langle d_\sigma, d_\sigma^\dagger c_{k\bar\sigma} d_{\bar\sigma}\rangle\rangle(t,s) \simeq 0\,. \tag{5.9b}$$

Next, we calculate the equation of motion for $\langle\langle d_\sigma, c_{k\sigma}^\dagger n_{\bar\sigma}\rangle\rangle(t,t')$:

$$\begin{aligned}\langle\langle d_\sigma, c_{k\sigma}^\dagger n_{\bar\sigma}\rangle\rangle(t,t') = &\int \frac{ds}{\hbar}\; V_k^* \langle\langle d_\sigma, d_\sigma^\dagger n_{\bar\sigma}\rangle\rangle(t,s) \mathrm{g}_k(s,t') \\ &+ \sum_k \int \frac{ds}{\hbar}\; \Big(V_k \langle\langle d_\sigma, c_{k\sigma}^\dagger c_{k\bar\sigma}^\dagger d_{\bar\sigma}\rangle\rangle(t,s) \\ &\qquad - V_k^* \langle\langle d_\sigma, c_{k\sigma}^\dagger d_{\bar\sigma}^\dagger c_{k\bar\sigma}\rangle\rangle(t,s)\Big)\, \mathrm{g}_k(s,t')\,, \end{aligned} \tag{5.10}$$

where we neglect reservoir charge and spin excitations for the same reason as discussed above,

$$\langle\langle d_\sigma, c_{k\sigma}^\dagger c_{k\bar\sigma}^\dagger d_{\bar\sigma}\rangle\rangle(t,s) \simeq 0\,, \tag{5.11a}$$

$$\langle\langle d_\sigma, c_{k\sigma}^\dagger d_{\bar\sigma}^\dagger c_{k\bar\sigma}\rangle\rangle(t,s) \simeq 0\,. \tag{5.11b}$$

Combining Eqs. (5.8) and (5.10) with Eqs. (5.9) and (5.11) we obtain a closed expression for $\langle\langle d_\sigma, d_\sigma^\dagger n_{\bar\sigma}\rangle\rangle(t,t')$:

$$\begin{aligned}\langle\langle d_\sigma, d_\sigma^\dagger n_{\bar\sigma}\rangle\rangle(t,t') = &\langle n_{\bar\sigma}(t)\rangle\, \mathrm{g}_\sigma(t,t') \\ &+ \int \frac{ds}{\hbar}\; \langle\langle d_\sigma, d_\sigma^\dagger n_{\bar\sigma}\rangle\rangle(t,s) \varepsilon_{ac}(s) \mathrm{g}_\sigma(s,t') \\ &+ \int \frac{ds}{\hbar} \int \frac{ds'}{\hbar}\; \langle\langle d_\sigma, d_\sigma^\dagger n_{\bar\sigma}\rangle\rangle(t,s') \Sigma_0(s',s) \mathrm{g}_\sigma(s,t') \\ &+ U \int \frac{ds}{\hbar}\; \langle\langle d_\sigma, d_\sigma^\dagger n_{\bar\sigma}\rangle\rangle(t,s) \mathrm{g}_\sigma(s,t')\,. \end{aligned} \tag{5.12}$$

We have thus derived two coupled integral equations, namely Eqs. (5.7) and (5.12), which must be self-consistently solved because Eq. (5.12) depends on $\langle n_\sigma(t)\rangle$ and to calculate this quantity we need to know $G_\sigma^<(t,t)$ (see Eq. (5.7)), which depends itself on $\langle n_\sigma(t)\rangle$ via Eq. (5.12). Further progress can be made by expanding the equations in powers of driving frequency Ω. It is worthwhile to emphasize that Eq. (5.7) is exact while Eq. (5.12) is a quite reasonable approximation that works fairly well in the Coulomb blockade regime.

5.3 Noninteracting case

It is instructive to begin our discussion with the independent particle approximation. This is easy to accomplish by setting $U = 0$ in Eq. (5.7). Thus, we obtain an integral equation that depends on the dot Green's function only,

$$\begin{aligned}\mathcal{G}_\sigma(t,t') = \mathrm{g}_\sigma(t,t') + \int \frac{ds}{\hbar}\, \mathcal{G}_\sigma(t,s)\varepsilon_{ac}(s)\mathrm{g}_\sigma(s,t') \\ + \int \frac{ds}{\hbar} \int \frac{ds'}{\hbar}\, \mathcal{G}_\sigma(t,s')\Sigma_0(s',s)\mathrm{g}_\sigma(s,t') \,. \quad (5.13)\end{aligned}$$

Importantly, we have changed our notation $G \to \mathcal{G}$ in order to distinguish between the Green's function corresponding to the the Coulomb Blockade regime (G) and that for noninteracting electrons ($\mathcal{G}$). This is done for later convenience since we will show that interacting results can indeed be expressed using noninteracting quantities.

A frequency expansion of Eq. (5.13) yields (we refer the reader to App. G.1 for details):

$$\mathcal{G}_\sigma^{r/a,f}(t,\varepsilon) = \frac{1}{\varepsilon - \varepsilon_\sigma - \varepsilon_{ac}(t) - \Sigma_0^{r/a}(\varepsilon)}\,, \quad (5.14a)$$

$$\mathcal{G}_\sigma^{r/a,(1)}(t,\varepsilon) = \frac{i}{\Omega}\partial_t\varepsilon_{ac}(t)\mathcal{G}_\sigma^{r/a,f}(t,\varepsilon)\partial_\varepsilon\mathcal{G}_\sigma^{r/a,f}(t,\varepsilon)\,, \quad (5.14b)$$

$$\mathcal{G}_\sigma^{<,f}(t,\varepsilon) = \mathcal{G}_\sigma^{r,f}(t,\varepsilon)\Sigma_0^<(\varepsilon)\mathcal{G}_\sigma^{a,f}(t,\varepsilon)\,, \quad (5.14c)$$

$$\begin{aligned}\mathcal{G}_\sigma^{<,(1)}(t,\varepsilon) = \frac{i}{\Omega}\partial_t\varepsilon_{ac}(t)\Big(\mathcal{G}_\sigma^{a,f}(t,\varepsilon)\partial_\varepsilon\mathcal{G}_\sigma^{<,f}(t,\varepsilon) \\ + \mathcal{G}_\sigma^{<,f}(t,\varepsilon)\partial_\varepsilon\mathcal{G}_\sigma^{r,f}(t,\varepsilon)\Big)\,, \quad (5.14d)\end{aligned}$$

where the superscript "r/a" labels the retarded/advanced Green's function and the tunnel self-energies read $\Sigma_0^{r/a}(\varepsilon) = \mp i\Gamma$, $\Sigma_0^<(\varepsilon) = 2i\Gamma f(\varepsilon)$. $\Gamma = \pi|V_k|^2\rho$ is the hybridization width, which we take as a constant parameter. This is a good approximation when the tunnel probability $|V_k|^2$ and the lead density of states ρ depend weakly on energy, which is the experimentally relevant situation. As throughout this thesis, $f(\varepsilon) = 1/[1 + \exp{(\varepsilon - E_F)/k_BT}]$ denotes the Fermi-Dirac distribution with E_F the lead Fermi level and T the base temperature.

We consider the spin-degenerate case ($\Delta_Z = 0$). Therefore, the dot level fulfills

$$\varepsilon_\uparrow = \varepsilon_\downarrow \equiv \varepsilon_0\,, \quad (5.15)$$

and we can define a total dot occupation $\langle n(t)\rangle_0^f$ as

$$\langle n_\uparrow(t)\rangle_0^f = \langle n_\downarrow(t)\rangle_0^f \equiv \langle n(t)\rangle_0^f /2\,. \tag{5.16}$$

Here, the subscript 0 means "noninteracting". Using the expressions for the noninteracting Green's functions given by Eqs. (5.14), the current and mean occupation implied by Eq. (5.5) become

$$\langle n(t)\rangle_0^f = 2\int d\varepsilon\ f(\varepsilon)\mathcal{D}(t,\varepsilon)\,, \tag{5.17a}$$

$$I_0^{(1)}(t) = -2e\int d\varepsilon\ \left(-\partial_\varepsilon f(\varepsilon)\right)\mathcal{D}(t,\varepsilon)\partial_t\varepsilon_{ac}(t)\,, \tag{5.17b}$$

$$\langle n(t)\rangle_0^{(1)} = h\int d\varepsilon\ \left(-\partial_\varepsilon f(\varepsilon)\right)\mathcal{D}^2(t,\varepsilon)\partial_t\varepsilon_{ac}(t)\,, \tag{5.17c}$$

$$I_0^{(2)}(t) = eh\int d\varepsilon\ \left(-\partial_\varepsilon f(\varepsilon)\right)\partial_t\big(\mathcal{D}^2(t,\varepsilon)\partial_t\varepsilon_{ac}(t)\big)\,, \tag{5.17d}$$

where $\mathcal{D}(t,\varepsilon) \equiv \mathcal{D}_\uparrow(t,\varepsilon) = \mathcal{D}_\downarrow(t,\varepsilon)$ is the density of states written as

$$\mathcal{D}_\sigma(t,\varepsilon) = \frac{1}{\pi}\frac{\Gamma}{\big(\varepsilon-\varepsilon_\sigma-\varepsilon_{ac}(t)\big)^2+\Gamma^2}\,. \tag{5.18}$$

Equation (5.18) is a Breit-Wigner-like density of states which instantaneously changes with time. This is a physically transparent result—in the adiabatic regime the dot spectral function is given by the stationary density of states replacing the dot level ε_0 with the instantaneous variation of the dot potential as a function of time, i.e., $\varepsilon_0 \to \varepsilon_0 + \varepsilon_{ac}(t)$. In other words, the electron adjusts its dynamics to the slow ac potential. As a consequence, the frozen occupation [Eq. (5.17a)] is simply given by the integral of the local density states convoluted with the Fermi function. The next order in the Ω expansion [Eq. (5.17c)] depends on the derivative of $\varepsilon_{ac}(t)$, as it should. For small frequencies, this is a small correction to the frozen occupation. Finally, the capacitive and dissipative currents [Eqs. (5.17b) and (5.17d)] are just given by time derivatives of the frozen and the first-order occupations, respectively. At very low temperatures, the main contribution to both current contributions arises from the electrons around the Fermi energy due to the $-\partial_\varepsilon f$ term in the equations.

The total current $I_0(t) = I_0^{(1)}(t) + I_0^{(2)}(t)$ is plotted in Fig. 5.2(a) as a function of time for different ε_{ac} amplitudes. The results are

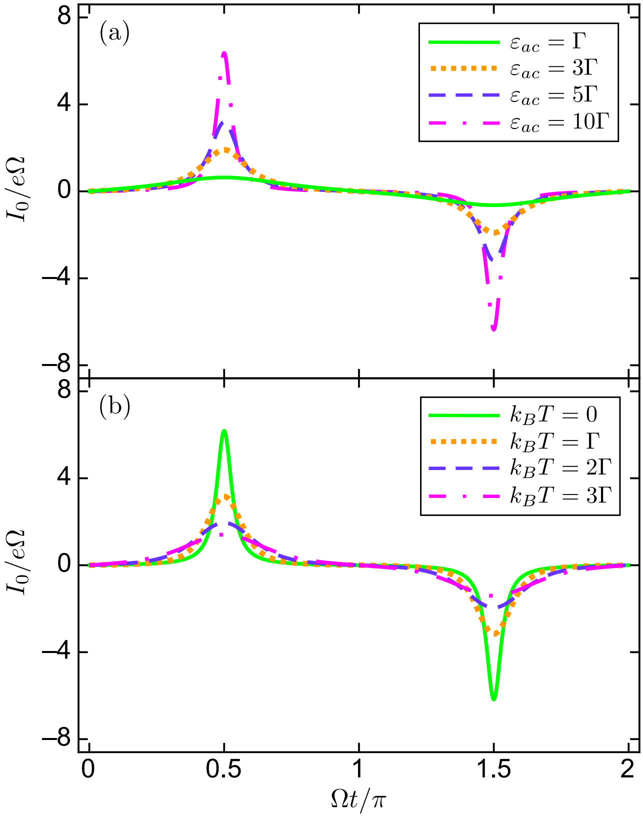

Figure 5.2: Noninteracting charge current (up to second order in the ac frequency) as a function time for different ac amplitudes (a) and temperatures (b). Parameters: $\varepsilon_0 = 0$, $\hbar\Omega = 0.02\,\Gamma$, (a) $k_BT = 0$, and (b) $\varepsilon_{ac} = 10\Gamma$.

calculated for zero temperature and very small ac frequencies. In the large amplitude case (pink dashed-dotted line), we observe a current peak (dip) in the first (second) half cycle since in the first (second) half cycle an electron is adsorbed (emitted) by the dot. This occurs when the ac modulated dot level aligns with the Fermi level, $\varepsilon_0+\varepsilon_{ac}\cos\Omega t = E_F$ (hereafter we set $E_F = 0$). The amplitude of the current peak (dip) is proportional to ε_{ac}, as shown in Eqs. (5.17b) and (5.17d). Therefore, the ac amplitude should be larger than Γ for the single-electron source to produce well defined current peaks. This is within experimental reach since $\varepsilon_{ac} \simeq 100$ μeV [128] and $\Gamma \simeq 10$ μeV. On the other hand, the ac frequency should be $\hbar\Omega = 0.02\,\Gamma \simeq 0.2$ μeV and the resulting current peak, given in Fig. 5.2(a) in units of $e\Omega$, attains values of the order of $I_0 \simeq 0.3$ nA, which is experimentally measurable.

At nonzero temperatures, the peaks broaden due to thermal smearing [see Fig. 5.2(b)]. The reason is clear—for large temperatures (larger than Γ) and fixed ac amplitude the current pulse is distributed among electronic states within k_BT around the Fermi energy and the pulse is not sharply peaked as in the $k_BT = 0$ case. As a consequence, low temperatures smaller than $T \simeq 100$ mK (=8.62 μeV) for $\Gamma \simeq 10$ μeV are needed to observe single-electron injection into the Fermi sea.

Figure 5.3 shows the total current for a fixed ε_{ac} as a function of time (horizontal axis) and the dot level position (vertical axis). The peak and dip found in Fig. 5.2 are also visible in Fig. 5.3 within a value range of ε_0. The current resonances shift with time in order to satisfy the resonant condition $\varepsilon_0 + \varepsilon_{ac}\cos\Omega t = E_F$. Notably, for dot levels such that $|\varepsilon_0| > |\varepsilon_{ac}|$ the current is identically zero independently of time, since at those energies the resonant condition is never met.

Now, using Eqs. (5.6), (5.17b), and (5.17d) we derive the following expressions for the differential capacitance and resistance:

$$C^0_\partial(t) = 2e^2\int d\varepsilon(-\partial_\varepsilon f)\mathcal{D}(t,\varepsilon)\,, \tag{5.19}$$

$$R^0_\partial(t) = \frac{h}{4e^2}\frac{\int d\varepsilon(-\partial_\varepsilon f)\partial_t\big(\mathcal{D}^2(t,\varepsilon)\partial_t\varepsilon_{ac}(t)\big)}{\int d\varepsilon(-\partial_\varepsilon f)\mathcal{D}(t,\varepsilon)\int d\varepsilon(-\partial_\varepsilon f)\partial_t\big(\mathcal{D}(t,\varepsilon)\partial_t\varepsilon_{ac}(t)\big)}\,, \tag{5.20}$$

where the dot density of states $\mathcal{D}(t,\varepsilon)$ is given by Eq. (5.18). Clearly, Eq. (5.19) can be interpreted as an instantaneous quantum capacitance. The physical meaning of the resistance of Eq. (5.20) is less

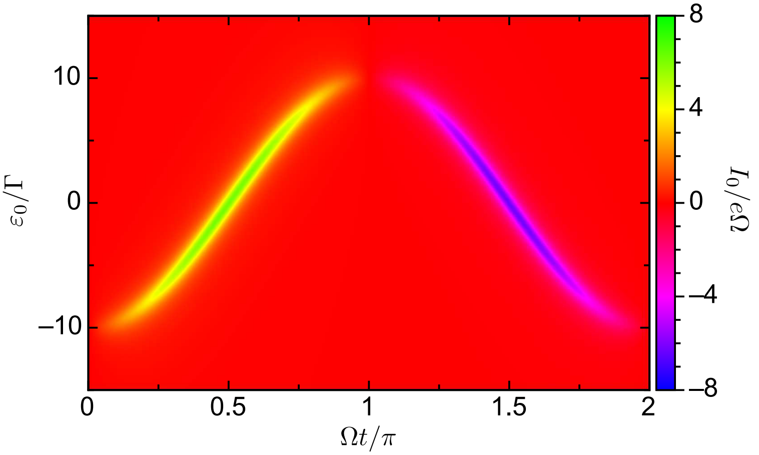

Figure 5.3: Noninteracting charge current (up to second order in the ac frequency) as a function of dot energy level (vertical axis) and time (horizontal). Parameters: $\varepsilon_{ac} = 10\Gamma$, $\hbar\Omega = 0.02\,\Gamma$, and $k_B T = 0$.

obvious. Only in linear response does $R_\partial^0(t)$ reduce to the charge relaxation resistance [166].

Figure 5.4(a) shows $C_\partial^0(t)$ for three specific cases: $\varepsilon_{ac} = 0.1\Gamma$ (solid green line), Γ (dotted orange line) and 10Γ (dashed blue line). In the first case, C_∂^0 is nearly time independent and takes on its maximum value as a constant times e^2/Γ. This occurs because in the low ε_{ac} limit the dot density of states has a constant value for any time. As the ac amplitude increases, a strong time dependence becomes apparent in terms of two well defined peaks when the aforementioned resonant condition is fulfilled. We observe that the minima of the dotted orange line never reaches zero since for intermediate values of ε_{ac} the dot energy level is close to E_F and can therefore be populated. In the strongly nonlinear case (dashed blue line) the two peaks become clearly resolved inasmuch as for large ε_{ac} the dot level gets fully depopulated (populated) after electron emission (injection).

In the linear regime ($\varepsilon_{ac} \to 0$) and zero temperature the quantum capacitance given by Eq. (5.19) takes a simpler form, $C_\partial^0 = 2e^2\mathcal{D}$, which is time independent and provides information about the dot density of states as we tune ε_0. In fact, the static density of states becomes $\mathcal{D} = (\Gamma/\pi)/[(E_F - \varepsilon_0)^2 + \Gamma^2]$, i.e., a Lorentzian curve centered

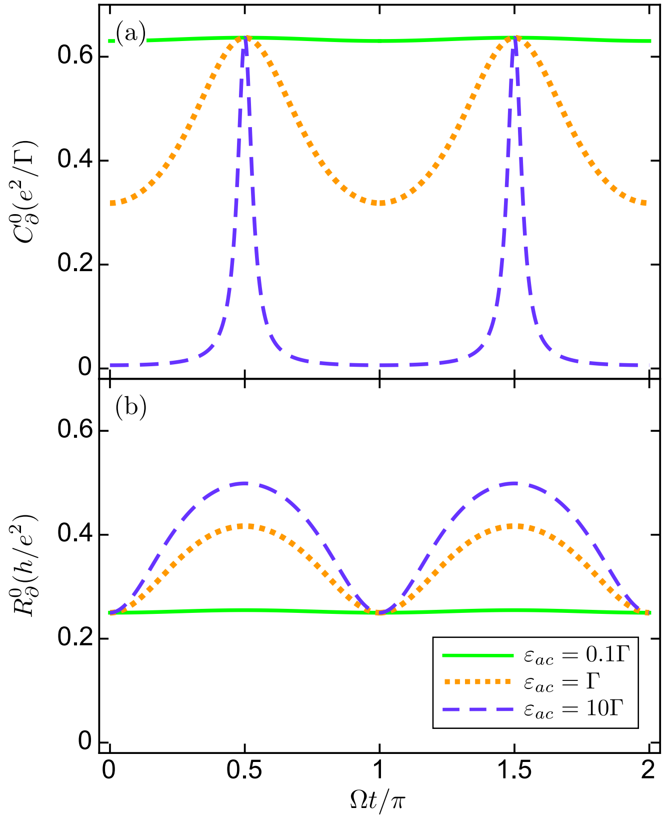

Figure 5.4: Differential capacitance (a) and differential resistance (b) as a function of time for different ac amplitudes. Parameters: $\varepsilon_0 = 0$, $\hbar\Omega = 0.02\Gamma$, and $k_B T = 0$.

at E_F with half-width Γ. Hence, the value marked by the solid green line of Fig. 5.4(a) is not universal and depends on the position of ε_0 with respect to E_F [149]. In particular, for $\varepsilon_0 = 0$ the capacitance is $C^0_\partial = 2e^2/\pi\Gamma \simeq 0.64e^2/\Gamma$ as shown in Fig. 5.4(a). In contrast, the resistance in the linear regime and for $k_BT = 0$ is not sample specific. R^0_∂ becomes time and energy independent [see the solid green line of Fig. 5.4(b)], taking the universal value $R^0_\partial = h/4e^2 = 0.25h/e^2$ (we recall that we have two independent channels, one per spin). This quantization of the resistance was earlier predicted by Büttiker *et al.* in 1993 [130] and later demonstrated experimentally for the spin-polarized case by Gabelli *et al.* in 2006 [127]. This resistance can be also connected with an instantaneous Joule law for the dissipated heat in the reservoir [175, 176].

Away from linear response [dotted orange line and dashed blue line in Fig. 5.4(b)], the resistance quickly deviates from the quantized value and becomes both time and energy dependent. With increasing ε_{ac}, R^0_∂ shows two peaks as a result of the resonant condition but, unlike the capacitance, the resistance peaks get higher and more broadened as the ac amplitude increases. Therefore, the dissipation enhances as ε_{ac} grows, which is naturally expected. The enhancement rate is, however, nonlinear and not easily derived from Eq. (5.20).

5.4 Coulomb Blockade Regime

Our aim now is to include Coulomb repulsion between electrons in the quantum dot and to investigate how the noninteracting results discussed in the previous section change in the presence of interactions. Before, we note that for metallic dots with good screening properties a Hartree approach (see App. H) is a good approximation. In what follows, however, we focus on small dots with strong electron-electron interactions.

In the Coulomb blockade regime, the charging energy is typically a large energy scale in the problem and for small dots one has $U > \pi\Gamma$ [144]. We start from the main results of the equation-of-motion method [Eqs. (5.7) and (5.12)]. The frequency expansion can be performed after somewhat lengthy calculations detailed in App. G.2. We find the frozen and dynamic (to leading order in Ω)

lesser and retarded Green's functions,

$$G^{r,f}_{\sigma}(t,\varepsilon)=\big(1-\langle n_{\bar\sigma}(t)\rangle^{f}\big)\mathcal{G}^{r,f}_{\sigma}(t,\varepsilon)+\langle n_{\bar\sigma}(t)\rangle^{f}\mathcal{G}^{r,f}_{U\sigma}(t,\varepsilon)\,, \tag{5.21a}$$

$$\begin{aligned} G^{r,(1)}_{\sigma}(t,\varepsilon)=\Big(&U\,\langle n_{\bar\sigma}(t)\rangle^{(1)}\,\mathcal{G}^{r,f}_{U\sigma}(t,\varepsilon)\\ &+\frac{i}{\Omega}\partial_t\varepsilon_{ac}(t)\Big[\big(1-\langle n_{\bar\sigma}(t)\rangle^{f}\big)\partial_\varepsilon\mathcal{G}^{r,f}_{\sigma}(t,\varepsilon)\\ &+(1+U\,\mathcal{G}^{r,f}_{U\sigma}(t,\varepsilon))\,\langle n_{\bar\sigma}(t)\rangle^{f}\partial_\varepsilon\mathcal{G}^{r,f}_{U\sigma}(t,\varepsilon)\Big]\Big)\mathcal{G}^{r,f}_{\sigma}(t,\varepsilon)\,, \end{aligned} \tag{5.21b}$$

$$G^{<,f}_{\sigma}(t,\varepsilon)=\big(1-\langle n_{\bar\sigma}(t)\rangle^{f}\big)\mathcal{G}^{<,f}_{\sigma}(t,\varepsilon)+\langle n_{\bar\sigma}(t)\rangle^{f}\mathcal{G}^{<,f}_{U\sigma}(t,\varepsilon)\,, \tag{5.21c}$$

$$\begin{aligned} G^{<,(1)}_{\sigma}(t,\varepsilon)=&\langle n_{\bar\sigma}(t)\rangle^{(1)}\,\Big(\mathcal{G}^{<,f}_{\sigma}(t,\varepsilon)-\mathcal{G}^{<,f}_{U\sigma}(t,\varepsilon)\Big)\\ &+\frac{i}{\Omega}\partial_t\varepsilon_{ac}(t)\Big(\big(1-\langle n_{\bar\sigma}(t)\rangle^{f}\big)\Big[\mathcal{G}^{a,f}_{\sigma}(t,\varepsilon)\partial_\varepsilon\mathcal{G}^{<,f}_{\sigma}(t,\varepsilon)\\ &\qquad+\mathcal{G}^{<,f}_{\sigma}(t,\varepsilon)\partial_\varepsilon\mathcal{G}^{r,f}_{\sigma}(t,\varepsilon)\Big]\\ &+\langle n_{\bar\sigma}(t)\rangle^{f}\Big[\mathcal{G}^{a,f}_{U\sigma}(t,\varepsilon)\partial_\varepsilon\mathcal{G}^{<,f}_{U\sigma}(t,\varepsilon)+\mathcal{G}^{<,f}_{U\sigma}(t,\varepsilon)\partial_\varepsilon\mathcal{G}^{r,f}_{U\sigma}(t,\varepsilon)\Big]\Big)\,. \end{aligned} \tag{5.21d}$$

Here, we express the interacting Green's functions (denoted by G) in terms of the noninteracting Green's functions [denoted by $\mathcal{G}$ and explicitly written in Eqs. (5.14)]. We indicate with the subscript U that $\mathcal{G}_{U\sigma}$ is the noninteracting Green's function with the replacement $\varepsilon_0 \to \varepsilon_0 + U$.

We focus on the nonmagnetic case as in Sec. 5.3. Notably, we find that the interacting occupations derived from Eqs. (5.21c) and (5.21d) can be also connected with the noninteracting densities of Eqs. (5.17a) and (5.17c):

$$\langle n(t)\rangle^{f}=\frac{2\,\langle n(t)\rangle^{f}_{0}}{2+\langle n(t)\rangle^{f}_{0}-\langle n(t)\rangle^{f}_{0U}}\,, \tag{5.22}$$

$$\langle n(t)\rangle^{(1)}=2\,\frac{\langle n(t)\rangle^{(1)}_{0}\,(2-\langle n(t)\rangle^{f}_{0U})+\langle n(t)\rangle^{(1)}_{0U}\,\langle n(t)\rangle^{f}_{0}}{(2+\langle n(t)\rangle^{f}_{0}-\langle n(t)\rangle^{f}_{0U})^2}\,, \tag{5.23}$$

where the subscript U again designates the substitution $\varepsilon_0 \to \varepsilon_0 + U$. From the latter equations we can immediately derive the capacitive and dissipative currents,

$$I^{(1)}(t)=2\,\frac{I^{(1)}_{0}(t)(2-\langle n(t)\rangle^{f}_{0U})+I^{(1)}_{0U}(t)\,\langle n(t)\rangle^{f}_{0}}{(2+\langle n(t)\rangle^{f}_{0}-\langle n(t)\rangle^{f}_{0U})^2}\,, \tag{5.24}$$

$$I^{(2)}(t)=e\partial_t\,\langle n(t)\rangle^{(1)}\,. \tag{5.25}$$

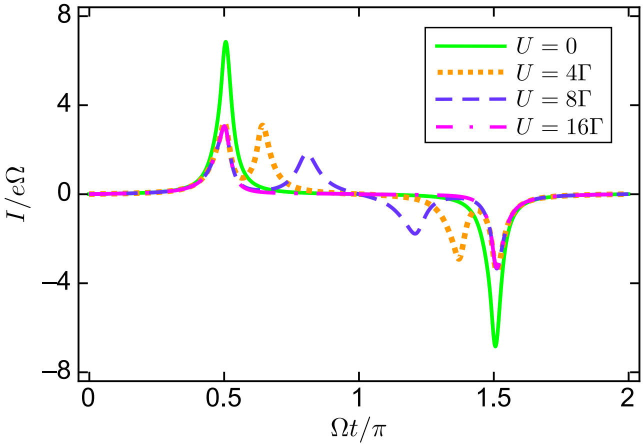

Figure 5.5: Interacting charge current (Coulomb blockade regime) as a function of time for different values of the charging energy U. Parameters: $\varepsilon_0 = 0$, $\varepsilon_{ac} = 10\Gamma$, $\hbar\Omega = 0.02\,\Gamma$, and $k_B T = 0$.

These are the central results of our paper. In particular, Eq. (5.24) states that the leading-order current for interacting electrons is given by a weighted sum of the noninteracting expressions [Eq. (5.17b)] corresponding to two resonances, namely, ε_0 and $\varepsilon_0 + U$. This finding is particularly appealing since it anticipates the main transformation of the noninteracting results—the current pulses, for moderate values of U, will split into two separate peaks. We will now confirm our expectation with exact numerical results.

Figure 5.5 shows the behavior of total charge current, $I^{(1)}(t) + I^{(2)}(t)$, as a function of time for $\varepsilon_0 = 0$, $\varepsilon_{ac} = 10\Gamma$, and different values of the charging energy U at zero temperature. For $U = 0$ (solid green line) we reproduce the curve from Fig. 5.2 for comparison with the nonzero U results. Strikingly enough, for $U = 4\Gamma$ (dotted orange line) both the peak and the dip split into two resonances each. Therefore, we have *two* consecutive electron emissions (absorptions) whenever ε_0 and $\varepsilon_0 + U$ cross above (below) the lead Fermi level thus satisfying the resonant condition. Furthermore, the amplitude of each resonance becomes reduced as compared with the noninteracting case. This can be understood if one recalls that in the noninteracting case the dot level is spin-degenerate while for interacting electrons each

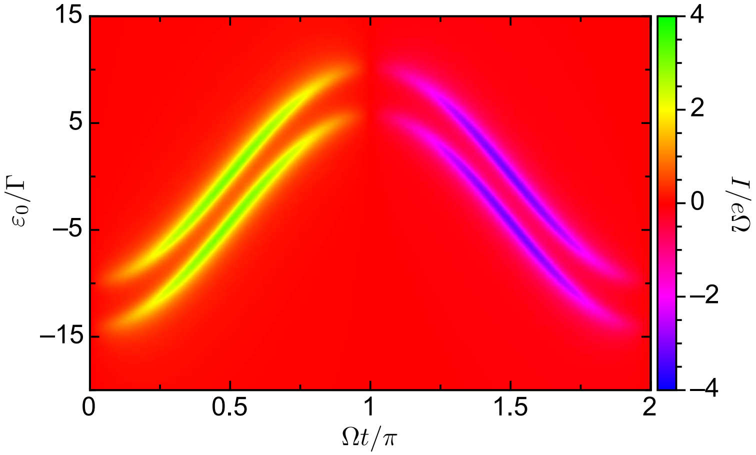

Figure 5.6: Interacting charge current (Coulomb blockade regime) as a function of the dot energy level (vertical axis) and time (horizonal axis). Parameters: $\varepsilon_{ac} = 10\Gamma$, $U = 4\Gamma$, $\hbar\Omega = 0.02\,\Gamma$, and $k_B T = 0$.

resonance can be occupied with at most one electron due to Pauli blocking. The splitting gradually increases as U is enhanced [see the transition to the dotted orange line ($U = 4\Gamma$) and the dashed blue line ($U = 8\Gamma$)] because the second resonance shifts to higher (lower) times as compared with the peak (dip) originally present for $U = 0$. This second resonance decreases its amplitude until it vanishes for $U > \varepsilon_{ac} = 16\Gamma$ (dashed-dotted pink line). This effect can be explained if we notice that the resonance $\varepsilon_0 + U$ never crosses the Fermi level if $U > \varepsilon_{ac}$. In other words, the two resonances can be occupied (at least partially) only if $U < E_F + \varepsilon_{ac} - \varepsilon_0$.

In Fig. 5.6 we present the total current as a function of time and the dot energy level position for a fixed charging energy ($U = 4\Gamma$) and ac amplitude ($\varepsilon_{ac} = 10\Gamma$). We see clear signatures of the peak splitting for a wide range of energy levels since as we tune ε_0 the resonant condition is satisfied at different times, as explained above.

Importantly, electron-electron interactions affect the charge quantization in a mesoscopic capacitor. From the total charge current we can obtain the charge Q emitted for a half of a period in terms of the

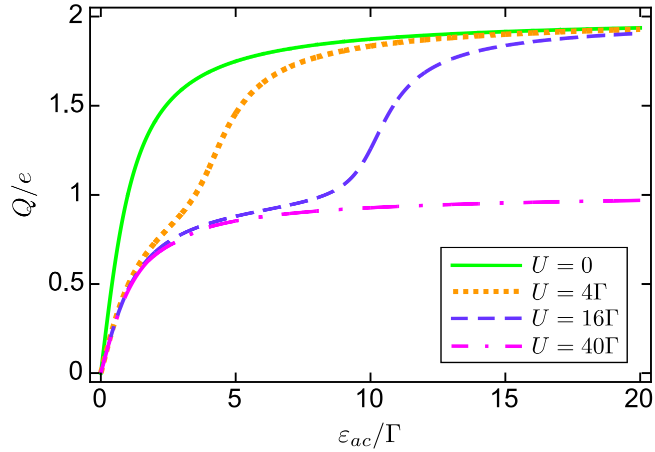

Figure 5.7: Charge (Coulomb blockade regime) as a function of the ac amplitude ε_{ac}. Parameters: $\varepsilon_0 = 0$, $\hbar\Omega = 0.02\,\Gamma$, and $k_B T = 0$.

occupation:

$$Q = \int_0^{\tau/2} dt\ I(t) = e\left(\langle n(t=\tau/2)\rangle - \langle n(t=0)\rangle\right), \qquad (5.26)$$

where $\tau = 2\pi/\Omega$ is the ac period and $\langle n(t)\rangle = \langle n(t)\rangle^f + \langle n(t)\rangle^{(1)}$ is the total occupation given by the sum of Eqs. (5.22) and (5.23) to lowest order in frequency. Figure 5.7 shows Q as a function of the ac amplitude for different values of the Coulomb strength, U. For $U = 0$ we recover a full charge quantization at large values of the harmonic potential [166]. With increasing electron-electron interactions, a new plateau emerges for intermediate values of ε_{ac}. This phenomenon is exclusively due to Coulomb repulsion effects since when $U > \Gamma$ the dot energy level is split into two resonances, ε_0 and $\varepsilon_0 + U$, which are occupied sequentially as ε_{ac} grows. It is worth noting that the transition between plateaus shifts to larger values of energy as U increases because when $U > \varepsilon_{ac}$ only the resonance at ε_0 is able to fulfill the resonant condition and the second plateau ceases to be visible. Therefore, it is crucial to take into account electron-electron interactions to give precise predictions on the charge quantization amplitude and its domain.

Let us turn now to the differential capacitance and resistance. In

Eqs. (5.19) and (5.20) we obtained their full expressions for noninteracting electrons. When interactions are present, we should combine Eq. (5.6) together with Eqs. (5.24) and (5.25) to arrive at the following relation:

$$C_\partial(t) = 2\,\frac{C_\partial^0(t)(2-\langle n(t)\rangle_{0U}^f) + C_\partial^{0U}(t)\,\langle n(t)\rangle_0^f}{(2+\langle n(t)\rangle_0^f - \langle n(t)\rangle_{0U}^f)^2}\,. \tag{5.27}$$

Remarkably, we again find the nice result that the Coulomb-blockaded capacitance $C_\partial(t)$ can be written in terms of a weighted sum of noninteracting capacitances renormalized by interactions. The weight factors depend themselves on shifted occupations calculated in the absence ($\langle n(t)\rangle_0^f$) and in the presence ($\langle n(t)\rangle_{0U}^f$) of interactions. Nevertheless, the analytic expression for the resistance is too lengthy to be included here. For the numerical calculations we shall use the definition

$$R_\partial(t) = e\frac{I^{(2)}(t)}{C_\partial(t)\partial_t(C_\partial(t)(\partial_t\varepsilon_{ac}(t)))}\,. \tag{5.28}$$

In Fig. 5.8 we plot Eqs. (5.27) and (5.28) as a function of time for different Coulomb strengths. In the top panel [Fig. 5.8(a)], we depict $C_\partial(t)$ in units of e^2/Γ. As expected, the capacitance, which mimics the instantaneous density of states, undergoes a double splitting for finite charging energies (cf. the case $U=0$ showed in solid green line with the case $U=8\Gamma$ in dotted orange line). The four-peak structure arises from multiple passings (upward and downward) of the resonances ε_0 and ε_0+U across the Fermi energy. Our calculations predict that four peaks (two in each half cycle) will appear in the Coulomb blockade regime ($U>\pi\Gamma$) and for sufficiently low temperature. Further increase of U leads to a recovery of the two peaks but with reduced amplitude. In general, for energies $U>E_F+\varepsilon_{ac}-\varepsilon_0$ (with $\varepsilon_0>0$) the resonance lying at ε_0+U is not able to fulfill the resonant condition and we recover the $U=0$ case but with half-height peaks due to the 1/2 occupation (on average) of each spin level.

We show the differential resistance R_∂ in Fig. 5.8(b). Already for $U=0$ we find departures from the universal charge relaxation resistance value $h/4e^2$. These deviations are stronger as U increases and lead to *negative* values of R_∂ for certain values of time. Therefore, we cannot identify the product $C_\partial R_\partial$ with a delay time since this

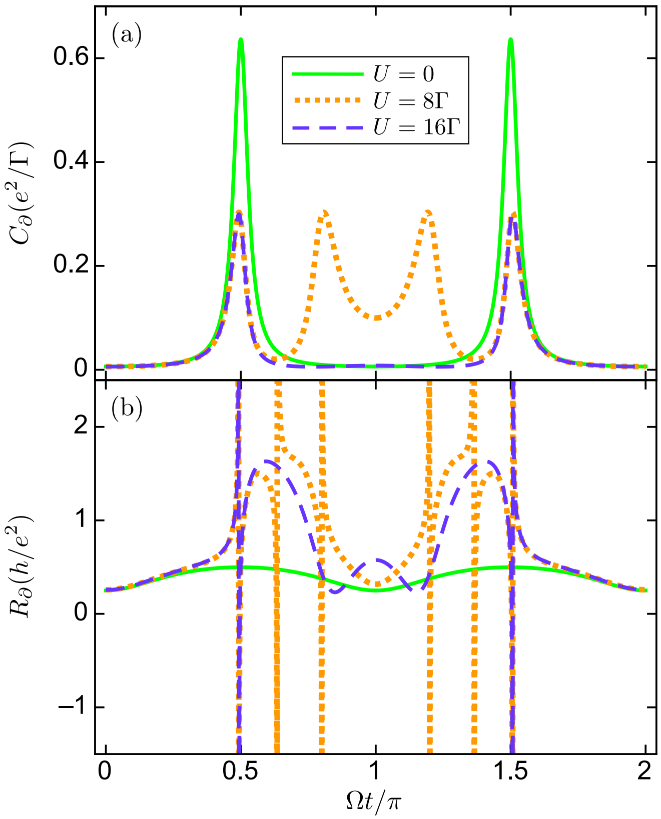

Figure 5.8: Differential capacitance (a) differential resistance (b) as a function of time for different values of the charging energy U. Parameters: $\varepsilon_0 = 0$, $\varepsilon_{ac} = 10\Gamma$, and $k_BT = 0$.

interpretation is physically meaningful in linear response only. In fact, at some points the resistance diverges. Analogous resistance divergences have been found in the thermoelectric transport [163] but here the effect is purely electric. Equation (5.28) dictates that the differential resistance is inversely proportional to the derivative of the differential capacitance. As a consequence, R_∂ diverges whenever this derivative vanishes. This implies that the resistance divergences are correlated with the maxima or minima of C_∂, as can be easily inferred from a close inspection of Figs. 5.8(a) and 5.8(b).

A natural question is then whether the strong fluctuations of the nonlinear resistance away from its quantized value persist in the linear regime. To examine this, we take the limit $\varepsilon_{ac} \to 0$ in Eqs. (5.27) and (5.28). We find for $k_B T = 0$ the expressions

$$C_\partial = 4\,\frac{\mathcal{D}(2-\langle n\rangle^f_{0U}) + \mathcal{D}_U\,\langle n\rangle^f_0}{(2+\langle n\rangle^f_0 - \langle n\rangle^f_{0U})^2}\,, \tag{5.29}$$

$$R_\partial = \frac{h}{8e^2}\frac{\mathcal{D}^2(2-\langle n\rangle^f_{0U})+\mathcal{D}_U^2\,\langle n\rangle^f_0}{(\mathcal{D}(2-\langle n\rangle^f_{0U})+\mathcal{D}_U\,\langle n\rangle^f_0)^2}(2+\langle n\rangle^f_0-\langle n\rangle^f_{0U})^2\,, \tag{5.30}$$

where $\mathcal{D} = \Gamma/[(E_F-\varepsilon_0)^2+\Gamma^2]$ and $\mathcal{D}_U = \Gamma/[(E_F-\varepsilon_0-U)^2+\Gamma^2]$. Interestingly, Eqs. (5.29) and (5.30) depend on the mean frozen occupation. The capacitance is a weighted sum of densities of states and will therefore show two peaks at $\varepsilon_0 \simeq E_F$ and $\varepsilon_0 \simeq E_F - U$ [see Fig. 5.9(a) where we depict the capacitance as a function of the dot level]. Even in the presence of interactions the capacitance can be traced back to a spectroscopic measure of the dot spectral function. However, the charge relaxation resistance is no longer constant as in the noninteracting case. In Fig. 5.9(b) we observe a strong energy dependence of R_∂ with ε_0. Only when the dot level is clearly off resonance (either $\varepsilon_0 \gg \Gamma$ or $\varepsilon_0 \ll \Gamma$) do we recover the universal value $h/4e^2$. In both cases the reason is clear—either for ε_0 well above E_F or for a deep level configuration, interactions play no role and the noninterating result is restored. In the electron-hole symmetry point $[\varepsilon_0 = (E_F - U)/2]$ the system behaves effectively as a single channel conductor because the occupation per spin is 1/2. For dot energies in between the electron-hole symmetry point and the off-resonant situation, the charge relaxation resistance acquires its maximum value, which is sample dependent. We attribute this resistance

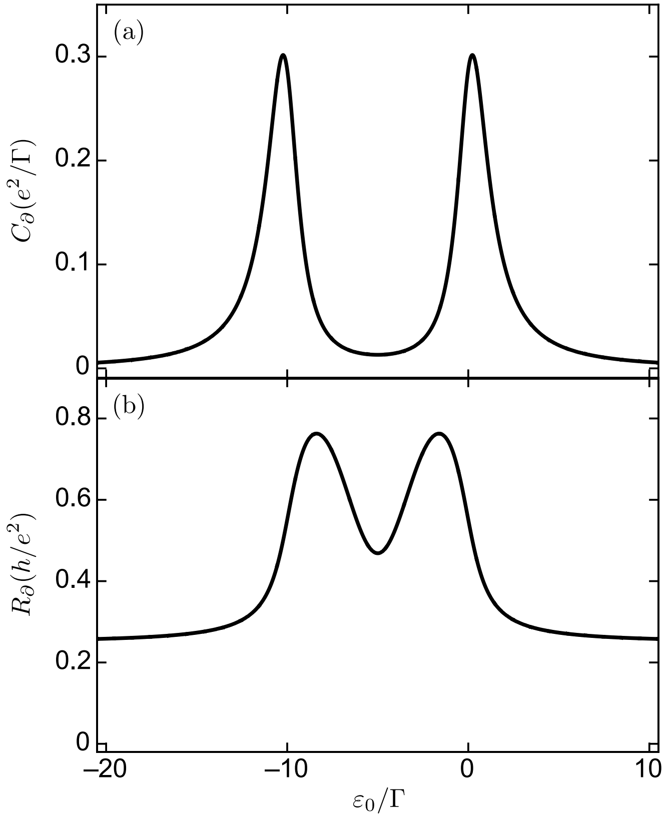

Figure 5.9: Quantum capacitance (a) and charge relaxation resistance resistance (b) as a function of dot energy level in the linear regime, $\varepsilon_{ac} \rightarrow 0$, and for interacting electrons in the Coulomb-blockade regime. Parameters: $U = 10\Gamma$, and $k_B T = 0$.

increase to the maximal charge fluctuations that operate around the point $\varepsilon_0 \simeq -\Gamma$ and its symmetric counterpart $\varepsilon_0 \simeq U - \Gamma$. We notice that significant enhancements of R_∂ have been previously reported in the literature for interacting RC circuits [158, 157].

5.5 Conclusions

In this chapter we have studied the Coulomb blockade effects in a system formed by a single-level quantum dot coupled to a reservoir via one channel and capacitively couplet to an oscillating potential. We have found, using the nonequilibrium Green's function method, that the current peaks become split with a reduced amplitude, which is to half of the noninteracting case. This second peak becomes smaller as the U increases until it disappears for $U > \varepsilon_{ac}$. We have also observed the presence of an additional quantization step in the emitted charge as a function of ε_{ac}. Importantly, our calculations are valid for arbitrarily large amplitudes of the ac potential and small frequencies in the Coulomb blockade regime.

6. Concluding remarks

The goal of this thesis has been to formulate theoretical models to study the electronic transport in a representative set of nanodevices in which the electric current arises in response to externally applied thermal gradients or ac potentials. The subject is interesting in view of the recent advances that have been reached in quantum thermoelectricity and in charge detection with temporal resolution. The charge current can be manipulated in a variety of ways. In this thesis, we have proposed to use the spin-orbit coupling in graphene and in two-dimensional electron gases in order to investigate the spintronic effects that give rise to polarized spin currents. Finally, the final objective has been to analyze the role of charging effects in quantum capacitors when electron-electron interactions dominate the physics of the problem.

In Chapter 2 we have investigated the electric and thermoelectric properties of a graphene monolayer with inhomogeneous Rashba spin-orbit interaction patterned as a stripe along the sample. We have discussed the energy splitting due to the Rashba coupling and their effect in the transmission probabilities. Importantly, the existence of a critical angle for only one of the two subband states leads to a finite polarization when the externally modulated Fermi energy is of the order of the spin-orbit strength.

We have found that our system is more sensitive to temperature shifts than to potential difference. Moreover, we have shown that the linear conductance is dominated by a given energy subband for large enough spin-orbit strengths or region sizes. Interestingly, we have obtained a strongly modulated thermoelectric conductance as a function of both parameters, which suggests useful applications of spin-orbit graphene as a heat-to-energy converter. Surprisingly enough, the thermopower as a function of Fermi energy is strongly influenced by an intrinsic term which is independent of the scattering potential. In contrast, we have obtained highly tunable thermopower as a function of the Rashba coupling and the width of the spin-orbit region. The strong energy variation is recovered when the thermopower is calculated in the subband space. Then, an applied temperature bias creates a subband polarization, which can attain significant values (positive or negative) at low Fermi energies.

We have considered a system free of disorder or scattering centers additional to the spin-orbit coupling. In a realistic sample, diffusion processes should be taken into account. However, it is remarkable that in the diffusive regime a similar intrinsic thermopower ($S \sim k_B^2 T_0/eE_F$) is obtained [67]. Therefore, further work is needed to clarify the behavior of the Seebeck coefficient in the transition from the diffusive regime to the ballistic (quantum) regime considered here. Another interesting route would focus on the role of phonons [177]. However, we do not expect that our results will change qualitatively since the phonon contribution is negligible at the low temperatures considered in this chapter.

Our results might be tested in a suspended graphene sample with a central section deposited onto a metallic substrate inducing a spin-orbit interaction. The coupling between the monolayer and the metal can be tuned with an external electric field. Then, thermovoltages and thermocurrents would be detected upon local heating of a sample side. An alternative measurement would consider heating currents generated in response to an applied electric current under vanishing thermal gradients (Peltier effect). Due to reciprocity, the measured response can be related to the thermopower. Finally, hot electrons can originate from sample irradiation, as recently demonstrated in Ref. [178]. Our results are thus relevant for the exciting area that emphasizes the interplay between spin interactions and thermoelectric effects in graphene and related nanostructures. Future works should investigate the validity of this statement for nanoribbons [179], magnetic samples [180] or different spin-orbit two-dimensional systems such as silicene [181].

In Chapter 3 we have discussed the quantum thermoelectric properties of a two-dimensional electron system with nonhomogeneous spin-orbit interaction. When the device is attached to normal electrodes, we find that the thermopower is strongly modulated by either the spin-orbit strength or the channel length at fixed Fermi energy. In the case of ferromagnetic leads, we distinguish between charge, spin and magneto-Seebeck effects. Interestingly, the thermoelectric dynamics is dominated by quantum interference effects for energies below the Zeeman splitting in the leads. These effects lead to large amplitude oscillations of the different thermopowers that change their sign as the Fermi energy increases. The number of observed oscillations can be tuned with the separation between contacts. Importantly, the Seebeck coefficients depend on the relative orientation of the magnetic moments in the leads, causing sizeable values of the magneto-Seebeck coefficient. In general, we demonstrate that a semiconductor two-dimensional electron system offers quite remarkable capabilities for the generation of highly tunable thermoelectric properties.

Our results may be also relevant for spin transistors built with two-dimensional electron systems other than semiconductor heterostructures: silicon [182, 183], graphene [184–188] or metal dichalcogenides [188]. Further extensions of our model should consider the quasi-one-dimensional case, which is important for quantum wires and carbon nanotubes. Another crucial aspect in modeling realistic ferromagnetic-tunnel junctions is the presence of tunnel barriers, which might alter the predictions discussed in this paper. Future works should also consider disorder effects, which are relevant in 2D systems with low mobility [189], and nonlinear features as those observed in the dc resistivity of quantum Hall conductors [190]

In Chapter 4 we have investigated a spin-orbit quantum wire coupled to quantum point contacts. We have found that both resonant tunneling and spin precession oscillations combine into complex patterns that can be explained with the aid of quasiperiodic modes in the strict 1D case. For the more realistic setup where the conducting channel has a finite width (2D case) we have discussed the important role of the Rashba intersubband coupling term as the spin-orbit strength increases.

We have used in our numerical simulations realistic parameters taken from the sample and measurements of Ref. [109]. Therefore, our predictions are within the realm of today's techniques. The angle between the spin-orbit fields in the QPCs and the quantum well can be tuned with lateral electric fields while the spin-orbit strength can be manipulated with a gate terminal on top of the middle cavity.

We have focused on the transmission, from which the two-terminal conductance G, which is experimentally accessible, readily follows in the zero temperature limit. For finite temperatures we expect thermal smearing effects but we have in mind low temperatures as in Ref. [109] (0.03 K). Thus, phonon effects can be safely neglected. Another detrimental effect would be the presence of disorder since we consider ballistic systems only and our predictions rely on quantum interference. Therefore, samples with large enough coherence lengths and mean free paths would be needed, which are now routinely available [191]. Measurement of diagonal and off-diagonal conductances can be achieved, e.g., with ferromagnetic electrodes whose relative magnetization can be changed from parallel to antiparallel orientation in response to a small magnetic field. The results regarding the length variation can be tested with different samples. Finally, the resolution of the conductance peaks would lie in the sub-meV range, which can be achieved by tuning an external backgate electrode capacitively coupled to the sample.

Further extensions of our work could address high-field transport properties, in which case inelastic transitions in three-dimensional resonant tunneling diodes can change the current–voltage characteristics [192, 193]. Another important issue for future works is the role of electron-electron interactions, which may lead to instabilities and hysteretic curves in double barrier systems [194]. Furthermore, magnetically doped resonant tunneling devices are shown to be quite sensitive to external magnetic fields [195, 90, 196]. In the presence of a spin-orbit coupling beating patterns are predicted to occur in double-barrier resonant tunneling structures [197]. Finally, we would like to mention the closely related systems known as chaotic dots [198] since they are built as semiconductor cavities between a pair of quantum point contacts, similarly to the two-dimensional cavities considered in the last part of our work. In contrast, our cavities have a regular shape. Interestingly, closed chaotic dots exhibit Coulomb blockade peak fluctuations [199] and subsequent discussions might then consider how these fluctuations are affected by the presence of spin-orbit interactions.

In Chapter 5 we have investigated Coulomb blockade effects in a coherent source of single-electrons driven by a monochromatic excitation. Using a nonequilibrium Green's function approach valid for arbitrarily large amplitudes of the ac potential, we have found that the current peaks associated to electron emission and absorption become split in the Coulomb blockade regime. The effect is particularly intense for the emitted charge, with additional quantization steps as a function of the ac forcing. Our model is capable of describing the noninteracting case ($U = 0$) up to strong interactions ($U \to \infty$) within the Coulomb blockade regime. While for $U = 0$ our theory produces two-electron or two-hole pulses, for $U \to \infty$ our model predicts single-electron or single-hole pulses. For intermediate values of U one may have two single-electron or single-hole pulses separated in time. Our model system is a mesoscopic capacitor but our results are equally relevant for different single-electron sources such as those formed with dopant atoms in silicon [200–202] or dots embedded in coplanar cavities [203–206].

Further investigations should address the role of cotunneling processes which are dominant in the Coulomb blockade valley at temperatures $k_B T \ll \Gamma$. One possibility is to relax the conditions given by Eqs. (5.9) and (5.11) and to make a step further in the equation-of-motion hierarchy. In particular, spin-flip cotunneling processes would lead to Kondo correlations that would alter the picture discussed here. In general, we expect the minimum between current peaks (dips) to rise (lower) due to the buildup of a many-body Kondo resonance pinned at the Fermi energy. An additional peak should then appear in the quantum capacitance since it is proportional to the local density of states. However, a new energy scale ($k_B T_K$ with T_K the Kondo temperature) would arise and a more careful analysis should be carried out.

Another assumption of our model is the spin degeneracy in both the dot level and the coupled reservoir. Introducing a Zeeman splitting Δ_Z would lead to extra splittings that would compete with the existing ones depending on the strength of Δ_Z as compared with Γ, U and $k_B T$. We note that the original experiments by Fève *et al.* [128] applied a strong magnetic field that drove the system into the quantum Hall regime. Moreover, the dot coupled to a gate with a large capacitance and charging effects were then negligible. To test our predictions, we would need a smaller dot in the absence of magnetic fields (or with Zeeman fields smaller than the characteristic energy scales).

Finally, we have focused on the adiabatic regime (low frequencies). This approximation is valid if one is interested in the capacitance and the charge relaxation resistance. Arbitrary frequencies are beyond the scope of the present work but are certainly interesting (for $U = 0$ see, e.g., Refs. [207, 208]). In fact, for larger frequencies (larger than the GHz scale considered in this work) photon-assisted tunneling takes place [209, 210] and our frequency expansion breaks down. It would be highly desirable to take into account large frequencies and amplitudes in a unified framework for the purely ac transport of electrons in nanostructures.

Appendices

A. Scattering approach

In this appendix we will discuss the charge current in the scattering approach used in Chapters 2 and 3.

This approach, also called Landauer-Büttiker formalism, is very useful to study mesoscopic transport. In this framework the current through a conductor is determined in terms of the probability that an electron can be transmitted through the sample. Then, the transport properties of the system are related with the scattering properties, which can be known by means of a quantum-mechanical calculation.

We consider a mesoscopic sample attached to two contacts, left (ℓ) and right (r) respectively. We assume that the contacts are large enough to be able to define a characteristic temperature T_c and chemical potential μ_c with $c = \ell, r$. Since each of them is in thermal equilibrium separately, we can define the electron's distribution in the contacts with the aid of the Fermi distribution function, $f_c(E) = 1/[1 + e^{(E-\mu_c)/k_B T_c}]$.

It is important to point out that, although there are no inelastic processes in the sample, the only way to establish a strict equilibrium state in the contacts is via inelastic processes. This can be understood as follows: If one electron from contact ℓ with temperature T_ℓ and electrochemical potential μ_ℓ travels across the system towards contact r, in this contact the electron has to change its energy and temperature to T_r and μ_r, and this is only possible via inelastic processes (thermalization). Then, we assume that the contacts are wide compared to the typical cross-section of the mesoscopic conductor and, as a consequence, this inelastic processes occur far form the sample so that we can describe the local properties of the contacts in terms of the equilibrium state.

Another important point is that far from the sample we can separate the transverse and longitudinal motion of the electrons. The longitudinal motion is referred to be the direction from the left to the right contact and along this direction the system is open and has a continuous wave number k. For future calculations it is helpful to distinguish between incoming and outgoing states. This scattering states are characterized by the longitudinal energy $E_l = \hbar^2 k^2/2m$. In contrast, the transverse motion across the contacts is confined by a transverse potential. Because of that, the transverse energies states are quantized by the discrete momentum q_n and these can be different in each contact, $E_{\ell,r;n}$. In other words, not all the q-momenta are allowed. Finally, the total energy of the electrons in the system is given by the sum of both contributions (longitudinal and transverse), $E = E_l + E_n$. Since E_l has to be positive in order for the current to flow, for a fixed total energy E only a certain number of channels (or modes) are open. Since it is possible that the number of open modes will be different in each contact, we define the number of incoming channels by $n_{\ell,r}$ in the left and right side, respectively.

Now we are in the position of defining our system, which consists of a narrow conductor with a few transverse channels attached to two wider contacts, ideally with infinite transverse channels. Then, the contacts act as sources of carriers determined by their Fermi distribution. We also assume reflectionless contacts, which means that the contacts act as perfect sinks of carriers independently of its energy with which they leave the conductor. Finally, we define the creation and annihilation operators of electrons in the scattering states as $\hat{a}^\dagger_{\ell,r;q_n}(E)$ and $\hat{a}_{\ell,r;q_n}(E)$ with total energy E and transverse momentum q_n in the left and right side, which are incident on the sample. Following the same reasoning, $\hat{b}^\dagger_{\ell,r;q_n}(E)$ and $\hat{b}_{\ell,r;q_n}(E)$ create and annihilate electrons in the outgoing states, respectively [211].

We define the quantum mechanical current operator from the left contact as follows,

$$\hat{I}_\ell(t) = \frac{e}{h} \sum_{q_n} \int_{-\infty}^{\infty} dE \int_{-\infty}^{\infty} dE' e^{i(E-E')t/\hbar} \times \left[\hat{a}^\dagger_{\ell q_n}(E) \hat{a}_{\ell q_n}(E') - \hat{b}^\dagger_{\ell q_n}(E) \hat{b}_{\ell q_n}(E') \right], \quad \text{(A.1)}$$

where $\hat{n}^+_{\ell q_n}(E) = \hat{a}^\dagger_{\ell q_n}(E)\hat{a}_{\ell q_n}(E)$ is the incoming occupation number operator from the left contact in a channel characterized by the transverse momentum q_n and $\hat{n}^-_{\ell q_n}(E) = \hat{b}^\dagger_{\ell q_n}(E)\hat{b}_{\ell q_n}(E)$ in the outgoing number operator. We integrate over all the energies E and E', sum over all the allowed transverse momenta q_n and multiply by e/h where h is the Planck constant which comes from the definition of carriers' velocity $v = (1/\hbar)\partial E(k)/\partial k$ and e is the electron charge. As a result, Eq. (A.1) has correct units.

Now, through the scattering matrix s we can relate the operators $\hat{a}$ and $\hat{b}$,

$$\left(\begin{array}{c} \hat{b}_{\ell q_1} \\ \cdots \\ \hat{b}_{\ell q_{n_\ell}} \\ \hat{b}_{r q_1} \\ \cdots \\ \hat{b}_{r q_{n_r}} \end{array} \right) = s \left(\begin{array}{c} \hat{a}_{\ell q_1} \\ \cdots \\ \hat{a}_{\ell q_{n_\ell}} \\ \hat{a}_{r q_1} \\ \cdots \\ \hat{a}_{r q_{n_r}} \end{array} \right) , \tag{A.2}$$

where the s matrix takes the following form,

$$s = \left(\begin{array}{cc} r & t' \\ t & r' \end{array} \right) . \tag{A.3}$$

Here, the blocks r, of size $n_\ell \times n_\ell$, and r', of size $n_r \times n_r$ describe the reflection amplitude of electrons back to the left and right reservoirs, respectively. Consequently, the blocks t, of size $n_r \times n_\ell$, and t', of size $n_\ell \times n_r$, are the amplitude transmission of electrons across the sample. The matrix s is quite generally unitary due to the flux conservation in the scattering process. Further, s is symmetric in the presence of time-reversal symmetry.

Introducing Eq. (A.2) into Eq. (A.1) and using matrix notation we obtain,

$$\hat{I}_\ell(t) = \frac{e}{h} \sum_{\alpha\beta} \sum_{q_m q_n} \int_{-\infty}^{\infty} dE \int_{-\infty}^{\infty} dE' e^{i(E-E')t/\hbar}$$

$$\hat{a}^\dagger_{\alpha q_m}(E) A^{q_m q_n}_{\alpha\beta}(\ell; EE_\prime) \hat{a}_{\beta q_n}(E') \, , \tag{A.4}$$

where the indices α and β label the contacts ℓ and r. The matrix A is defined as

$$A^{q_m q_n}_{\alpha\beta}(\ell; EE_\prime) = \delta_{mn} \delta_{\alpha\ell} \delta_{\beta\ell} -$$

$$\sum_{q_l} s^\dagger_{\ell\alpha; q_m q_l}(E) s_{\ell\beta; q_l q_n}(E') \, , \tag{A.5}$$

where $s_{\ell\beta;q_l q_n}(E)$ is the scattering amplitude that relates $\hat{b}_{\ell q_m}(E)$ with $\hat{a}_{\alpha q_l}(E)$.

In order to achieve the current flowing along x-direction for a Fermi gas at thermal equilibrium we perform the quantum statistical average of Eq. (A.4)

$$I = \langle \hat{I}_\ell(t) \rangle = \frac{e}{h} \int_{-\infty}^{\infty} dE\, Tr[t^\dagger(E) t(E)][f_\ell(E) - f_r(E)] \,, \qquad \text{(A.6)}$$

where we have used that

$$\langle \hat{a}^\dagger_{\alpha q_m}(E) \hat{a}_{\beta q_n}(E') \rangle = \delta_{mn} \delta_{\alpha\beta} \delta(E'_E) f_\alpha(E) \,. \qquad \text{(A.7)}$$

In Eq. (A.6) the matrices t and t' are the off-diagonal block of the scattering matrix given by Eq. (A.3). We note that the matrix $t^\dagger t$ can be diagonalized obtaining

$$I = \frac{e}{h} \sum_{q_n} \int_{-\infty}^{\infty} dE\, T(E, q_n)[f_\ell(E) - f_r(E)] \,, \qquad \text{(A.8)}$$

where $T(E, q_n)$ is the transmission probability of one carrier injected from the left contact with energy E and transverse momentum q_n arriving to the right contact.

In our calculation the transmission probability are spin dependent, $T(E, q_n) = \sum_{s's} T_{s's}(E, q_n)$. Then, the spin current flowing along x-direction is given by

$$I_s = \frac{e}{h} \sum_{s'} \sum_{q_n} \int_{-\infty}^{\infty} T_{s's}(E, q_n) \left[f_\ell(E) - f_r(E)\right] dE \,, \qquad \text{(A.9)}$$

where $\sum_{s'}$ is a sum over the transmitted spin and $\sum_{q_n}$ a sum over all the possibles momenta on the y-direction. Here $f_c(E)$ with $c = \ell, r$ are the Fermi distribution functions defined above and $T_{s's}$ the transmission probability from spin s to spin s'.

In the continuum limit valid fore wide samples, we make the replacement

$$\sum_{q_n} \longrightarrow \frac{W}{2\pi} \int_{-\infty}^{\infty} dq \,, \qquad \text{(A.10)}$$

where W is the width of the sample in the y-direction and $q = \mathcal{K}(E)\sin\phi$ with $\mathcal{K}(E)$ the momentum magnitude and ϕ the incident angle. Using this relation,

$$I_s = \frac{e}{h}\frac{W}{2\pi}\int_{-\pi/2}^{\pi/2}\cos\phi\,d\phi\int_{-\infty}^{\infty}\sum_{s'}T_{s's}(E,\phi)\,\mathcal{K}(E)\times[f_\ell(E)-f_r(E)]\,dE\,. \quad \text{(A.11)}$$

Using the fact that $T_{s's}(E,\phi)\cos\phi$ is an even function and that the contribution to the current of the states with negative energy is zero, we find

$$I_s = \frac{e}{h}\frac{W}{\pi}\int_{0}^{\pi/2}\cos\phi\,d\phi\int_{-\infty}^{\infty}\sum_{s'}T_{s's}(E,\phi)\,\mathcal{K}(E)\times[f_\ell(E)-f_r(E)]\,dE\,. \quad \text{(A.12)}$$

This corresponds to Eqs. (2.13) and (3.14) in Chapter 2 and 3, respectively.

B. Rashba spin-orbit coupling

In this appendix we derive the Rashba spin-orbit interaction for electrons in a two-dimensional electron system. The spin-orbit coupling is a relativistic effect. Therefore, we describe the electron motion with the Dirac equation

$$i\hbar\frac{\partial}{\partial t}\psi(t) = (c\vec{\alpha}\cdot\vec{p} + \beta mc^2)\psi(t)\,, \tag{B.1}$$

where c is the light speed, m the electron mass, $\vec{p} = -i\hbar\nabla$ the momentum operator,

$$\vec{\alpha} = \begin{pmatrix} 0 & \vec{\sigma} \\ \vec{\sigma} & 0 \end{pmatrix}, \quad \beta = \begin{pmatrix} \mathbb{I} & 0 \\ 0 & -\mathbb{I} \end{pmatrix} \tag{B.2}$$

and $\vec{\sigma}$ the Pauli matrix vector.

Since Eq. (B.1) is a matrix equation, ψ has four components

$$\psi(t) = \begin{pmatrix} \psi_1(t) \\ \psi_2(t) \\ \psi_3(t) \\ \psi_4(t) \end{pmatrix} \equiv \begin{pmatrix} \psi_+(t) \\ \psi_-(t) \end{pmatrix}, \tag{B.3}$$

where $\psi_\pm(t)$ are vectors of two components.

Now, defining the time-dependent part of the wave function as

$$\psi(t) = \psi e^{-iEt/\hbar}\,, \tag{B.4}$$

we can rewrite Eq. (B.1) and obtain

$$E\psi = (c\vec{\alpha}\cdot\vec{p} + \beta mc^2)\psi\,, \tag{B.5}$$

with $E = E_S + mc^2$ and E_S is the energy that appears in the Schrödinger equation.

Then, in order to obtain the Rashba coupling term we include in Eq. (B.5) the action of an electric field, see Sec. 1.3.2.1. With the aid of the electric potential ϕ and substituting $E \to E - q\phi$,we find

$$E\psi = (c\vec{\alpha}\cdot\vec{p} + \beta mc^2 + q\phi)\psi\,, \tag{B.6}$$

where $q = -e\,(e > 0)$ is the electron charge.

Writing Eq. (B.5) in matrix form and decoupling the two resulting equations we obtain

$$\left[(\vec{\sigma}\cdot\vec{p})\frac{c^2}{E + mc^2 - q\phi}(\vec{\sigma}\cdot\vec{p}) + q\phi\right]\psi_+ = (E - mc^2)\psi_+\,. \tag{B.7}$$

Now, we expand Eq. B.7 to order $(v/c)^4$ and obtain

$$\begin{aligned} E_S\psi_+ = \Bigg[&\frac{\vec{p}^2}{2m} + q\phi - \frac{\vec{p}^4}{8m^3c^2} \\ &- \frac{q\hbar}{4m^2c^2}\,\vec{\sigma}\cdot(\vec{p}\times\vec{\mathcal{E}}) - \frac{iq\hbar}{4m^2c^2}\,(\vec{p}\cdot\vec{\mathcal{E}})\Bigg]\psi_+\,, \end{aligned} \tag{B.8}$$

where we have used $\vec{p}\phi = -i\hbar\nabla\phi = -i\hbar\vec{\mathcal{E}}$. In addition to the free Hamiltonian $\vec{p}^2/(2m) + q\phi$, one finds three relativistic corrections [212]. The fourth term describes the spin-orbit interaction, i.e., the action of an external electric field on a moving spin. We replace the electric field $\vec{\mathcal{E}}$ by $-\nabla V(\vec{r})/e$ where $V(\vec{r}) = e\phi(\vec{r})$ is the potential energy. Then, the fourth term of Eq. (B.8) can be written (after symmetrization) as

$$-\frac{\hbar}{8m^2c^2}\left(\vec{\sigma}\cdot[\vec{p}\times\nabla V(\vec{r})] + \nabla V(\vec{r})\cdot[\vec{\sigma}\times\vec{p}]\right)\,. \tag{B.9}$$

This is the general form of the spin-orbit interaction Hamiltonian.

We are interested in systems based on a 2DEG in which electrons are strongly confined in the z-direction by a confining potential $V(z)$, see Chapters 3 and 4. This means that

$$\frac{dV}{dz} \gg \frac{dV}{dx}\,,\frac{dV}{dy} \quad \text{and then} \quad \nabla V(\vec{r}) \sim \hat{z}\frac{d}{dz}V\,. \tag{B.10}$$

Moreover, for inversion asymmetric heterostructures this $V(z)$ is asymmetric with respect to the reflection point $z = 0$ and, as a consequence, the matrix element $\langle\Phi|(d/dz)V(z)|\Phi\rangle \neq 0$ where $\Phi(z)$ are the bound states in the z-direction. Taking into account all these conditions, Eq. (B.9) reduces to the Rashba spin-orbit interaction Hamiltonian

$$H_R^{\mathrm{2DEG}} = \frac{1}{2\hbar}\hat{z}\cdot\left[\alpha(\vec{\sigma}\times\vec{p}) + (\vec{\sigma}\times\vec{p})\alpha\right], \tag{B.11}$$

where

$$\alpha = -\frac{\hbar^2}{4m^2c^2}\langle\Phi|\frac{d}{dz}V(z)|\Phi\rangle\,, \tag{B.12}$$

is the Rashba coupling strength and depends on the material parameters. For a constant value of α we arrive at Eq. (1.35). When the spin-orbit coupling is not homogeneous, we must use Eq. (B.11) as discussed in Chapter 3. A more rigorous derivation of Eq. (B.11) can be found in Ref. [56] where the conduction and valence bands are taken into account.

C. Dirac current

In this appendix we derive the probability current for electrons in a graphene monolayer. We describe the electrons in graphene as a massless Dirac fermions that obey [Eq. (1.15)]

$$H = -i\hbar v_F \vec{\sigma} \cdot \vec{\nabla}\,, \tag{C.1}$$

where v_F is the Fermi velocity and $\vec{\sigma} = (\sigma_x, \sigma_y)$ the Pauli matrix vector.

The Schrödinger equation takes the following form,

$$i\hbar \frac{\partial \psi(\bar{r},t)}{\partial t} = H\psi(\bar{r},t)\,, \tag{C.2}$$

where $\vec{r} = (x, y)$ and the wave function expressed as a spinor of two components is

$$\psi(\bar{r},t) = \left(\begin{array}{c} X(\bar{r},t) \\ Y(\bar{r},t) \end{array} \right) . \tag{C.3}$$

For simplicity, we consider the one-dimensional case. Then, the Hamiltonian reads $H = -i\hbar v_F \sigma_x \partial/\partial x$. When we substitute Eq. (C.3) into Eq. (C.2) we obtain,

$$i\hbar \frac{\partial}{\partial t} \left(\begin{array}{c} X(x) \\ Y(x) \end{array} \right) = -i\hbar V_F \left(\begin{array}{cc} 0 & \frac{\partial}{\partial x} \\ \frac{\partial}{\partial x} & 0 \end{array} \right) \left(\begin{array}{c} X(x) \\ Y(x) \end{array} \right) . \tag{C.4}$$

This matrix equation gives two coupled equations

$$\frac{\partial}{\partial t} X(x) = -V_F \frac{\partial}{\partial x} Y(x)\,, \tag{C.5a}$$

$$\frac{\partial}{\partial t} Y(x) = -V_F \frac{\partial}{\partial x} X(x)\,. \tag{C.5b}$$

Then, in order to obtain the expression for $\vec{J}$ we consider the right-hand side of the following continuity equation,

$$\frac{\partial}{\partial t}\rho = -\vec{\nabla} \cdot \vec{J} \,. \tag{C.6}$$

In one-dimension, where we only have current along the x-direction, we find

$$\begin{aligned} \frac{\partial}{\partial t}\rho = \frac{\partial}{\partial t}|\psi|^2 = \frac{\partial}{\partial t}\psi^*\psi &= \frac{\partial(XX^* + YY^*)}{\partial t} \\ &= X^*\frac{\partial X}{\partial t} + X\frac{\partial X^*}{\partial t} + Y^*\frac{\partial Y}{\partial t} + Y\frac{\partial Y^*}{\partial t} \\ &= -V_F(X\frac{\partial Y^*}{\partial x} + X^*\frac{\partial Y}{\partial x} + Y^*\frac{\partial X}{\partial x} + Y\frac{\partial X^*}{\partial x}) \\ &= -V_F\frac{\partial(YX^* + XY^*)}{\partial x} = -\frac{\partial J_x}{\partial x} \,. \end{aligned} \tag{C.7}$$

Therefore,

$$J_x = V_F(YX^* + XY^*) = V_F\psi^\dagger\sigma_x\psi \,. \tag{C.8}$$

This expression can be straightforwardly generalized to:

$$\vec{J} = V_F\psi^\dagger\vec{\sigma}\psi \,. \tag{C.9}$$

D. Interfaces

This appendix contains the mathematical expressions of $\alpha(x)$ and $\Delta(x)$ employed in our numerical simulations for the interfaces. We model the step-like character of these quantities using Fermi-like functions

$$\mathcal{F}_{x_0,\sigma}(x) = \frac{1}{1 + e^{(x-x_0)/\sigma}} \,, \tag{D.1}$$

where x_0 is the junction position of the step and σ determines the length around x_0 where the transition takes place. Then,

$$\alpha(x) = \alpha \left(\mathcal{F}_{L/2,\sigma_\alpha}(x) - \mathcal{F}_{-L/2,\sigma_\alpha}(x) \right) \,, \tag{D.2a}$$

$$\Delta(x) = \Delta_\ell \mathcal{F}_{-d/2,\sigma_\Delta}(x) + \Delta_r \left(1 - \mathcal{F}_{d/2,\sigma_\Delta}(x) \right) \,, \tag{D.2b}$$

where the Rashba strength α and the Zeeman splitting $\Delta_{r,\ell}$ are constants. Here L is the region in between the contacts where the Rashba spin-orbit interaction acts and d, which is smaller than L, is the distance between the ferromagnetic contacts. For mode details see Ref. [119]. Our results are independent of the interface details because we take sharp transitions, i.e., $\sigma_\alpha \ll L$. In our numerical calculations we take $\sigma_\alpha = 0.1L_0$, $\sigma_\Delta = 0.3L_0$ and $d = 20L_0$.

E. Heat transport

In this appendix we will study the heat current which we use in Chapter 3.

The stationary heat current (say, at the right contact) is given by:

$$Q_r = \frac{1}{h}\frac{W}{2\pi}\sum_s \int_0^\infty dE\, \mathcal{T}_s(E)\mathcal{K}(E)\,(E-\mu_{rs}) \\ \times \left[f_{\ell s}(E) - f_{rs}(E)\right]\,, \quad \text{(E.1)}$$

where μ_{rs} is the chemical potential in the right contact at given spin s. The sum of the right and the left heat current gives the dissipated Joule heating, $Q_r + Q_\ell = IV$.

We apply a small voltage bias which, after Taylor expanding up to first order in V, gives the electrothermal conductance $M = (dQ/dV)_{V=0}$

$$M = \frac{e\pi W(k_B T_0)^2}{6hE_F}\mathcal{K}_F \sum_s \left(\frac{1}{2}\mathcal{T}_s + E_F\frac{\partial \mathcal{T}_s}{\partial E_F}\right) \quad \text{(E.2)}$$

at very low values of T_0. Here, $\mathcal{T}_s = \mathcal{T}_s(E_F)$. Comparing with Eq. (3.18), we check that the Klein-Onsager relation, $M = T_0 L$, is fulfilled as expected.

The thermal conductance, $K = (dQ/d(\Delta T))_{\Delta T=0}$, is obtained in linear response when a small temperature difference is applied across the junction. At low temperatures we find:

$$K = \frac{\pi W k_B^2 T_0}{6h}\mathcal{K}_F\,\mathcal{T}(E_F)\,, \quad \text{(E.3)}$$

where $\mathcal{T}(E_F) = \sum_s \mathcal{T}_s(E_F)$. Then, the Wiedemann-Franz law is satisfied since $K/T_0 G = \pi^2 k_B^2/3e^2$.

F. Fourier transform

This appendix contains a set of Fourier transformation relations which we use in Chapter 5.

The double Fourier transformation and its inverse are defined as

$$\mathcal{G}(t,t') = \sum_{m,n} \int \frac{d\varepsilon}{2\pi}\; e^{-i(\varepsilon+m\hbar\Omega)t/\hbar} e^{i(\varepsilon+n\hbar\Omega)t'/\hbar} \mathcal{G}(m-n,\varepsilon_n)\,, \tag{F.1}$$

$$\mathcal{G}(m-n,\varepsilon_n) = \int_0^{\tau} \frac{dt}{\tau} \int \frac{dt'}{\hbar}\; e^{i(\varepsilon+m\hbar\Omega)t/\hbar} e^{-i(\varepsilon+n\hbar\Omega)t'/\hbar} \mathcal{G}(t,t')\,, \tag{F.2}$$

where m and n are intergers, $\tau = 2\pi/\Omega$ is the ac period, and $\varepsilon_n = \varepsilon + n\hbar\Omega$. Notice that only the states whose energies differ by interger times $\hbar\Omega$ can be coupled. It is convenient to employ the mixed time-energy representation

$$\mathcal{G}(t,\varepsilon) = \sum_{n} e^{-in\Omega t} \mathcal{G}(n,\varepsilon)\,. \tag{F.3}$$

The Fourier transform can then be written in the form

$$\mathcal{G}(t,t') = \int \frac{d\varepsilon}{2\pi}\; e^{-i\varepsilon(t-t')/\hbar} \mathcal{G}(t,\varepsilon) \tag{F.4}$$

and the corresponding inverse Fourier transforms are given by

$$\mathcal{G}(t,\varepsilon) = \int \frac{dt'}{\hbar}\; e^{i\varepsilon(t-t')/\hbar} \mathcal{G}(t,t')\,, \tag{F.5}$$

$$\mathcal{G}(n,\varepsilon) = \int_0^{\tau} \frac{dt}{\tau}\; e^{in\Omega t} \mathcal{G}(t,\varepsilon)\,, \tag{F.6}$$

respectively.

G. Frequency expansion

In this appendix we will explain is detail the different steps needed to obtain the frozen and first order in frequency dot Green function in both the interacting and noninteracting case.

We begin by applying the double Fourier transform Eq. (F.2) to Eqs. (5.7) and (5.12):

$$
\begin{aligned}
G_\sigma(n,\varepsilon) = \mathrm{g}_\sigma(n,\varepsilon) &+ \sum_p G_\sigma(n-p,\varepsilon_p)[\varepsilon_{ac}\mathrm{g}_\sigma](p,\varepsilon) \\
&+ \sum_{p,q} G_\sigma(n-p,\varepsilon_p)\Sigma_0(p-q,\varepsilon_q)\mathrm{g}_\sigma(q,\varepsilon) \\
&+ U\sum_p \langle\langle d_\sigma, d_\sigma^\dagger n_{\bar\sigma}\rangle\rangle(n-p,\varepsilon_p)\mathrm{g}_\sigma(p,\varepsilon)\,, \qquad \text{(G.1)}
\end{aligned}
$$

$$
\begin{aligned}
\langle\langle d_\sigma, d_\sigma^\dagger n_{\bar\sigma}\rangle\rangle(n,\varepsilon) = &\left[\langle n_{\bar\sigma}\rangle \mathrm{g}_\sigma\right](n,\varepsilon) \\
&+ \sum_p \langle\langle d_\sigma, d_\sigma^\dagger n_{\bar\sigma}\rangle\rangle(n-p,\varepsilon_p)\left[\varepsilon_{ac}\mathrm{g}_\sigma\right](p,\varepsilon) \\
&+ \sum_{p,q} \langle\langle d_\sigma, d_\sigma^\dagger n_{\bar\sigma}\rangle\rangle(n-p,\varepsilon_p)\Sigma_0(p-q,\varepsilon_q)\mathrm{g}_\sigma(q,\varepsilon) \\
&+ U\sum_p \langle\langle d_\sigma, d_\sigma^\dagger n_{\bar\sigma}\rangle\rangle(n-p,\varepsilon_p)\mathrm{g}_\sigma(p,\varepsilon)\,. \qquad \text{(G.2)}
\end{aligned}
$$

The retarded/advanced and lesser Green's functions then follow from Eqs. (G.1) and (G.2) by applying the Langreth's rules [168].

G.1 Noninteracting case

In the noninteracting case, we set $U = 0$ and therefore $\langle\langle d_\sigma, d_\sigma^\dagger n_{\bar\sigma}\rangle\rangle(n,\varepsilon)$ in Eqs. (G.1) and (G.2) is neglected.

G.1.1 Retarded and advanced Green's function

The retarded/advanced dot Green's function is given by

$$\begin{aligned}\mathcal{G}^{r/a}_\sigma(n,\varepsilon) = \mathrm{g}^{r/a}_\sigma(n,\varepsilon) + \sum_p \mathcal{G}^{r/a}_\sigma(n-p,\varepsilon_p)[\varepsilon_{ac}\mathrm{g}^{r/a}_\sigma](p,\varepsilon) \\ + \sum_{p,q} \mathcal{G}^{r/a}_\sigma(n-p,\varepsilon_p)\Sigma^{r/a}_0(p-q,\varepsilon_q)\mathrm{g}^{r/a}_\sigma(q,\varepsilon)\,,\end{aligned} \tag{G.3}$$

with

$$\mathrm{g}^{r/a}_\sigma(n,\varepsilon) = \frac{\delta_{n,0}}{\varepsilon-\varepsilon_\sigma \pm i0^+} = \delta_{n,0}\mathrm{g}^{r/a}_\sigma(\varepsilon)\,, \tag{G.4a}$$

$$\Sigma^{r/a}_0(m-n,\varepsilon_n) = \mp i\delta_{m,n}\Gamma(\varepsilon_n) = \delta_{m,n}\Sigma^{r/a}_0(\varepsilon_n)\,, \tag{G.4b}$$

$$[\varepsilon_{ac}\mathrm{g}^{r/a}_\sigma](n,\varepsilon) = \frac{\varepsilon_{ac}}{2}(\delta_{n,1}+\delta_{n,-1})\mathrm{g}^{r/a}_\sigma(\varepsilon)\,, \tag{G.4c}$$

where $\Gamma(\varepsilon_n) = 2\pi|V_k|^2\rho(\varepsilon_n)$ and $\rho(\varepsilon_n) = \sum_k \delta(\varepsilon_n - \varepsilon_k)$ is the reservoir density of states.

Introducing Eq. (G.4) into Eq. (G.3), we find

$$\mathcal{G}^{r/a}_\sigma(n,\varepsilon) = \Big(\delta_{n,0} + \frac{\varepsilon_{ac}}{2}\sum_{p=\pm1}\mathcal{G}^{r/a}_\sigma(n-p,\varepsilon_p)\Big)\mathscr{G}^{r/a}_\sigma(\varepsilon)\,, \tag{G.5}$$

where

$$\mathscr{G}^{r/a}_\sigma(\varepsilon) = \frac{1}{\varepsilon-\varepsilon_\sigma-\Sigma^{r/a}_0(\varepsilon)}\,. \tag{G.6}$$

We now expand in powers of $\hbar\Omega$

$$\begin{aligned}\mathcal{G}(n-p,\varepsilon_p) = \mathcal{G}^f(n-p,\varepsilon) \\ + \hbar\Omega\Big(p\partial_\varepsilon\mathcal{G}^f(n-p,\varepsilon) + \mathcal{G}^{(1)}(n-p,\varepsilon)\Big) + \dots\,,\end{aligned} \tag{G.7}$$

and substitute it in Eq. (G.5) to find

$$\mathcal{G}^{r/a,f}_\sigma(n,\varepsilon) = \Big(\delta_{n,0} + \frac{\varepsilon_{ac}}{2}\sum_{p=\pm1}\mathcal{G}^{r/a}_\sigma(n-p,\varepsilon)\Big)\mathscr{G}^{r/a}_\sigma(\varepsilon)\,, \tag{G.8}$$

$$\begin{aligned}\mathcal{G}^{r/a,(1)}_\sigma(n,\varepsilon) = \frac{\varepsilon_{ac}}{2}\sum_{p=\pm1}\Big(p\partial_\varepsilon\mathcal{G}^{r/a,f}_\sigma(n-p,\varepsilon) \\ + \mathcal{G}^{r/a,(1)}_\sigma(n-p,\varepsilon)\Big)\mathscr{G}^{r/a}_\sigma(\varepsilon)\,.\end{aligned} \tag{G.9}$$

Using Eq. (F.3) and taking into account the wide band limit $\Gamma(\varepsilon) = \Gamma$, which is a good approximation for reservoirs with flat densities of states, we arrive at Eqs. (5.14a) and (5.14b) of Chapter 5.

G.1.2 Lesser Green's function

The lesser Green's function for the quantum dot electrons can be obtained as

$$\begin{aligned}\mathcal{G}^<_\sigma(n,\varepsilon) &= \delta_{n,0}\mathrm{g}^<_\sigma(n,\varepsilon)\\ &\quad+\sum_p\Big(\mathcal{G}^r_\sigma(n-p,\varepsilon_p)[\varepsilon_{ac}\mathrm{g}^<_\sigma](p,\varepsilon)+\mathcal{G}^<_\sigma(n-p,\varepsilon_p)[\varepsilon_{ac}\mathrm{g}^a_\sigma](p,\varepsilon)\Big)\\ &\quad+\sum_{p,q}\Big(\mathcal{G}^r_\sigma(n-p,\varepsilon_p)\Sigma^r_0(p-q,\varepsilon_q)\mathrm{g}^<_\sigma(q,\varepsilon)\\ &\qquad\qquad+\mathcal{G}^r_\sigma(n-p,\varepsilon_p)\Sigma^<_0(p-q,\varepsilon_q)\mathrm{g}^a_\sigma(q,\varepsilon)\\ &\qquad\qquad\quad+\mathcal{G}^<_\sigma(n-p,\varepsilon_p)\Sigma^a_0(p-q,\varepsilon_q)\mathrm{g}^a_\sigma(q,\varepsilon)\Big)\,, \qquad \text{(G.10)}\end{aligned}$$

where

$$\mathrm{g}^<_\sigma(n,\varepsilon) = 2\pi i\delta_{n,0}\delta(\varepsilon-\varepsilon_\sigma)f(\varepsilon_\sigma) = \delta_{n,0}\mathrm{g}^<_\sigma(\varepsilon)\,, \qquad \text{(G.11a)}$$

$$\Sigma^<_0(m-n,\varepsilon_n) = 2i\delta_{m,n}\Gamma(\varepsilon_n)f(\varepsilon_n) = \delta_{m,n}\Sigma^<_0(\varepsilon_n)\,, \qquad \text{(G.11b)}$$

$$[\varepsilon_{ac}\mathrm{g}^<_\sigma](n,\varepsilon) = \frac{\varepsilon_{ac}}{2}(\delta_{n,1}+\delta_{n,-1})\mathrm{g}^<_\sigma(\varepsilon)\,. \qquad \text{(G.11c)}$$

Introducing Eqs. (G.4) and (G.11) into Eq. (G.10) and using $\mathrm{g}^{r,-1}_\sigma(\varepsilon)\mathrm{g}^<_\sigma(\varepsilon)=0$ we find

$$\mathcal{G}^<_\sigma(n,\varepsilon) = \Big(\frac{\varepsilon_{ac}}{2}\sum_{p=\pm1}\mathcal{G}^<_\sigma(n-p,\varepsilon_p) + \mathcal{G}^r_\sigma(n,\varepsilon)\Sigma^<_0(\varepsilon)\Big)\mathscr{G}^a_\sigma(\varepsilon)\,. \qquad \text{(G.12)}$$

This is the starting point for a series expansion in powers of $\hbar\Omega$. The procedure is analogous to Eq. (G.7). Then, the frozen and first order terms in Ω become, respectively,

$$\mathcal{G}^{<,f}_\sigma(n,\varepsilon) = \Big(\frac{\varepsilon_{ac}}{2}\sum_{p=\pm1}\mathcal{G}^{<,f}_\sigma(n-p,\varepsilon) + \mathcal{G}^{r,f}_\sigma(n,\varepsilon)\Sigma^<_0(\varepsilon)\Big)\mathscr{G}^a_\sigma(\varepsilon)\,, \qquad \text{(G.13)}$$

$$\mathcal{G}^{<,(1)}_\sigma(n,\varepsilon) = \left(\frac{\varepsilon_{ac}}{2}\sum_{p=\pm1}\Big(p\partial_\varepsilon\mathcal{G}^{<,f}_\sigma(n-p,\varepsilon)+\mathcal{G}^{r,(1)}_\sigma(n-p,\varepsilon)\Big) + \mathcal{G}^{r,(1)}_\sigma(n,\varepsilon)\Sigma^<_0(\varepsilon)\right)\mathscr{G}^a_\sigma(\varepsilon)\,. \qquad \text{(G.14)}$$

As discussed earlier, we can again use Eq. (F.3) and consider the wide band limit, which leads to Eqs. (5.14c) and (5.14d).

G.2 Interacting case: Coulomb blockade regime

In order to describe the Coulomb blockade regime, we consider the nonzero U case. Hence, Eq. (G.2) must be taken into account.

G.2.1 Retarded and advanced Green's function

The retarded/advanced Green's functions are simply derived from Eq. (G.1) and (G.2), yielding

$$\begin{aligned}
G_\sigma^{r/a}(n,\varepsilon) &= \mathrm{g}_\sigma^{r/a}(n,\varepsilon) + \sum_p G_\sigma^{r/a}(n-p,\varepsilon_p)[\varepsilon_{ac}\mathrm{g}_\sigma^{r/a}](p,\varepsilon) \\
&\quad + \sum_{p,q} G_\sigma^{r/a}(n-p,\varepsilon_p)\Sigma_0^{r/a}(p-q,\varepsilon_q)\mathrm{g}_\sigma^{r/a}(q,\varepsilon) \\
&\quad\quad + U\sum_p \langle\langle d_\sigma, d_\sigma^\dagger n_{\bar\sigma}\rangle\rangle^{r/a}(n-p,\varepsilon_p)\mathrm{g}_\sigma^{r/a}(p,\varepsilon)\,, \qquad \text{(G.15)} \\
\langle\langle d_\sigma, d_\sigma^\dagger n_{\bar\sigma}\rangle\rangle^{r/a}(n,\varepsilon) &= \left[\langle n_{\bar\sigma}\rangle \mathrm{g}_\sigma^{r/a}\right](n,\varepsilon) \\
&\quad + \sum_p \langle\langle d_\sigma, d_\sigma^\dagger n_{\bar\sigma}\rangle\rangle^{r/a}(n-p,\varepsilon_p)\left[\varepsilon_{ac}\mathrm{g}_\sigma^{r/a}\right](p,\varepsilon) \\
&\quad + \sum_{p,q} \langle\langle d_\sigma, d_\sigma^\dagger n_{\bar\sigma}\rangle\rangle^{r/a}(n-p,\varepsilon_p)\Sigma_0^{r/a}(p-q,\varepsilon_q)\mathrm{g}_\sigma^{r/a}(q,\varepsilon) \\
&\quad\quad + U\sum_p \langle\langle d_\sigma, d_\sigma^\dagger n_{\bar\sigma}\rangle\rangle^{r/a}(n-p,\varepsilon_p)\mathrm{g}_\sigma^{r/a}(p,\varepsilon)\,, \qquad \text{(G.16)}
\end{aligned}$$

with

$$\left[\langle n_{\bar\sigma}\rangle \mathrm{g}_\sigma^{r/a}\right](n,\varepsilon) = \langle n_{\bar\sigma}\rangle_n\, \mathrm{g}_\sigma^{r/a}(\varepsilon)\,, \qquad \text{(G.17)}$$

where we have used the Fourier expansion

$$\langle n_{\bar\sigma}(t)\rangle = \sum_n \langle n_{\bar\sigma}\rangle_n\, e^{-in\Omega t}\,. \qquad \text{(G.18)}$$

We substitute Eqs. (G.4) and (G.17) into Eqs. (G.15) and (G.16) and find

$$\begin{aligned} G_\sigma^{r/a}(n,\varepsilon) = \Big(\delta_{n,0} + \frac{\varepsilon_{ac}}{2} \sum_{p=\pm 1} G_\sigma^{r/a}(n-p,\varepsilon_p) \\ + U\langle\langle d_\sigma, d_\sigma^\dagger n_{\bar\sigma}\rangle\rangle^{r/a}(n,\varepsilon)\mathrm{g}_\sigma^{r/a}(\varepsilon)\Big)\mathscr{G}_\sigma^{r/a}(\varepsilon)\,, \quad \text{(G.19)} \\ \langle\langle d_\sigma, d_\sigma^\dagger n_{\bar\sigma}\rangle\rangle^{r/a}(n,\varepsilon) = \Big(\ \langle n_{\bar\sigma}\rangle_n \\ + \frac{\varepsilon_{ac}}{2} \sum_{p=\pm 1} \langle\langle d_\sigma, d_\sigma^\dagger n_{\bar\sigma}\rangle\rangle^{r/a}(n-p,\varepsilon_p)\Big)\mathscr{G}_\sigma^{r/a}(\varepsilon - U)\,, \quad \text{(G.20)} \end{aligned}$$

where $\mathscr{G}_\sigma^{r/a}$ is given by (G.6). The solution has poles at ε_σ and $\varepsilon_\sigma + U$ such that it properly describes the Coulomb blockade.

Let us now expand in powers of $\hbar\Omega$. The expansion is based upon Eq. (G.7), which leads to

$$\begin{aligned} G_\sigma^{r/a,f}(n,\varepsilon) = \Big(\delta_{n,0} + \frac{\varepsilon_{ac}}{2} \sum_{p=\pm 1} G_\sigma^{r/a}(n-p,\varepsilon) \\ + U\langle\langle d_\sigma, d_\sigma^\dagger n_{\bar\sigma}\rangle\rangle^{r/a,f}(n,\varepsilon)\Big)\mathscr{G}_\sigma^{r/a}(\varepsilon)\,, \quad \text{(G.21)} \\ G_\sigma^{r/a,(1)}(n,\varepsilon) = \Big(\frac{\varepsilon_{ac}}{2} \sum_{p=\pm 1} \Big[p\partial_\varepsilon G_\sigma^{r/a,f}(n-p,\varepsilon) \\ + G_\sigma^{r/a,(1)}(n-p,\varepsilon)\Big] \\ + U\langle\langle d_\sigma, d_\sigma^\dagger n_{\bar\sigma}\rangle\rangle^{r/a,(1)}(n,\varepsilon)\Big)\mathscr{G}_\sigma^{r/a}(\varepsilon)\,, \quad \text{(G.22)} \end{aligned}$$

where

$$\begin{aligned} \langle\langle d_\sigma, d_\sigma^\dagger n_{\bar\sigma}\rangle\rangle^{r/a,f}(n,\varepsilon) = \Big(\ \langle n_{\bar\sigma}\rangle_n^f \\ + \frac{\varepsilon_{ac}}{2} \sum_{p=\pm 1} \langle\langle d_\sigma, d_\sigma^\dagger n_{\bar\sigma}\rangle\rangle^{r/a,f}(n-p,\varepsilon)\Big)\mathscr{G}_\sigma^{r/a}(\varepsilon - U)\,, \quad \text{(G.23)} \\ \langle\langle d_\sigma, d_\sigma^\dagger n_{\bar\sigma}\rangle\rangle^{r/a,(1)}(n,\varepsilon) = \Big(\ \langle n_{\bar\sigma}\rangle_n^{(1)} \\ + \frac{\varepsilon_{ac}}{2} \sum_{p=\pm 1} \Big[p\partial_\varepsilon \langle\langle d_\sigma, d_\sigma^\dagger n_{\bar\sigma}\rangle\rangle^{r/a,f}(n-p,\varepsilon) \\ + \langle\langle d_\sigma, d_\sigma^\dagger n_{\bar\sigma}\rangle\rangle^{r/a,(1)}(n-p,\varepsilon)\Big]\Big)\mathscr{G}_\sigma^{r/a}(\varepsilon - U)\,. \quad \text{(G.24)} \end{aligned}$$

Expressing Eqs. (G.21) and (G.22) in the mixed time-energy representation leads to Eqs. (5.21a) and Eqs. (5.21b).

G.2.2 Lesser Green's function

Applying Langreth's rules again, the lesser Green's functions become

$$\begin{aligned}
G^{<}_{\sigma}(n,\varepsilon) &= \delta_{n,0}\mathrm{g}^{<}_{\sigma}(n,\varepsilon) \\
&+ \sum_{p} \Big(G^{r}_{\sigma}(n-p,\varepsilon_p)[\varepsilon_{ac}\mathrm{g}^{<}_{\sigma}](p,\varepsilon) + G^{<}_{\sigma}(n-p,\varepsilon_p)[\varepsilon_{ac}\mathrm{g}^{a}_{\sigma}](p,\varepsilon) \Big) \\
&+ U \sum_{p} \Big(\langle\langle d_\sigma, d^{\dagger}_{\sigma} n_{\bar{\sigma}} \rangle\rangle^{r}(n-p,\varepsilon_p)\mathrm{g}^{<}_{\sigma}(p,\varepsilon) \\
&\qquad\qquad + \langle\langle d_\sigma, d^{\dagger}_{\sigma} n_{\bar{\sigma}} \rangle\rangle^{<}(n-p,\varepsilon_p)\mathrm{g}^{a}_{\sigma}(p,\varepsilon) \Big) \\
&+ \sum_{p,q} \Big(G^{r}_{\sigma}(n-p,\varepsilon_p)\Sigma^{r}_{0}(p-q,\varepsilon_q)\mathrm{g}^{<}_{\sigma}(q,\varepsilon) + G^{r}_{\sigma}(n-p,\varepsilon_p) \\
&\quad \times \Sigma^{<}_{0}(p-q,\varepsilon_q)\mathrm{g}^{a}_{\sigma}(q,\varepsilon) + G^{<}_{\sigma}(n-p,\varepsilon_p)\Sigma^{a}_{0}(p-q,\varepsilon_q)\mathrm{g}^{a}_{\sigma}(q,\varepsilon) \Big) ,
\end{aligned} \tag{G.25}$$

$$\begin{aligned}
\langle\langle d_\sigma, d^{\dagger}_{\sigma} n_{\bar{\sigma}} \rangle\rangle^{<}_{\sigma}(n,\varepsilon) &= \left[\langle n_{\bar{\sigma}} \rangle \mathrm{g}^{<}_{\sigma}\right](n,\varepsilon) \\
&+ \sum_{p} \Big(\langle\langle d_\sigma, d^{\dagger}_{\sigma} n_{\bar{\sigma}} \rangle\rangle^{r}_{\sigma}(n-p,\varepsilon_p)[\varepsilon_{ac}\mathrm{g}^{<}_{\sigma}](p,\varepsilon) \\
&\qquad + \langle\langle d_\sigma, d^{\dagger}_{\sigma} n_{\bar{\sigma}} \rangle\rangle^{<}_{\sigma}(n-p,\varepsilon_p)[\varepsilon_{ac}\mathrm{g}^{a}_{\sigma}](p,\varepsilon) \Big) \\
&+ U \sum_{p} \Big(\langle\langle d_\sigma, d^{\dagger}_{\sigma} n_{\bar{\sigma}} \rangle\rangle^{r}(n-p,\varepsilon_p)\mathrm{g}^{<}_{\sigma}(p,\varepsilon) \\
&\qquad + \langle\langle d_\sigma, d^{\dagger}_{\sigma} n_{\bar{\sigma}} \rangle\rangle^{<}(n-p,\varepsilon_p)\mathrm{g}^{a}_{\sigma}(p,\varepsilon) \Big) \\
&+ \sum_{p,q} \Big(\langle\langle d_\sigma, d^{\dagger}_{\sigma} n_{\bar{\sigma}} \rangle\rangle^{r}_{\sigma}(n-p,\varepsilon_p)\Sigma^{r}_{0}(p-q,\varepsilon_q)\mathrm{g}^{<}_{\sigma}(q,\varepsilon) \\
&\qquad + \langle\langle d_\sigma, d^{\dagger}_{\sigma} n_{\bar{\sigma}} \rangle\rangle^{r}_{\sigma}(n-p,\varepsilon_p)\Sigma^{<}_{0}(p-q,\varepsilon_q)\mathrm{g}^{a}_{\sigma}(q,\varepsilon) \\
&\qquad + \langle\langle d_\sigma, d^{\dagger}_{\sigma} n_{\bar{\sigma}} \rangle\rangle^{<}_{\sigma}(n-p,\varepsilon_p)\Sigma^{a}_{0}(p-q,\varepsilon_q)\mathrm{g}^{a}_{\sigma}(q,\varepsilon) \Big) ,
\end{aligned} \tag{G.26}$$

with

$$\left[\langle n_{\bar{\sigma}} \rangle \mathrm{g}^{<}_{\sigma}\right](n,\varepsilon) = \langle n_{\bar{\sigma}} \rangle_{n}\, \mathrm{g}^{<}_{\sigma}(\varepsilon) \,. \tag{G.27}$$

Inserting Eqs. (G.4), (G.11), and (G.27) into Eqs. (G.25) and (G.26), and recalling that $\mathrm{g}_\sigma^{r-1}(\varepsilon)\mathrm{g}_\sigma^<(\varepsilon) = 0$, we get

$$\begin{aligned}G_\sigma^<(n,\varepsilon) = \Big(&\frac{\varepsilon_{ac}}{2}\sum_{p=\pm1} G_\sigma^<(n-p,\varepsilon_p)\\ &+ U\langle\langle d_\sigma, d_\sigma^\dagger n_{\bar\sigma}\rangle\rangle^<(n,\varepsilon) + G_\sigma^r(n,\varepsilon)\Sigma_0^<(\varepsilon)\Big)\mathscr{G}_\sigma^a(\varepsilon)\,, \qquad \text{(G.28)}\\ \langle\langle d_\sigma, d_\sigma^\dagger n_{\bar\sigma}\rangle\rangle_\sigma^<(n,\varepsilon) = \Big(&\frac{\varepsilon_{ac}}{2}\sum_{p=\pm1}\langle\langle d_\sigma, d_\sigma^\dagger n_{\bar\sigma}\rangle\rangle_\sigma^<(n-p,\varepsilon_p)\\ &+ \langle\langle d_\sigma, d_\sigma^\dagger n_{\bar\sigma}\rangle\rangle_\sigma^r(n,\varepsilon)\Sigma_0^<(\varepsilon)\Big)\mathscr{G}_\sigma^a(\varepsilon-U)\,. \qquad \text{(G.29)}\end{aligned}$$

The expansion in Ω yields

$$\begin{aligned}G_\sigma^{<,f}(n,\varepsilon) = \Bigg(&\frac{\varepsilon_{ac}}{2}\sum_{p=\pm1} G_\sigma^{<,f}(n-p,\varepsilon)\\ &+ U\langle\langle d_\sigma, d_\sigma^\dagger n_{\bar\sigma}\rangle\rangle_\sigma^{<,f}(n,\varepsilon) + G_\sigma^{r,f}(n,\varepsilon)\Sigma_0^<(\varepsilon)\Bigg)\mathscr{G}_\sigma^a(\varepsilon)\,, \qquad \text{(G.30)}\\ G_\sigma^{<,(1)}(n,\varepsilon) = \Bigg(&\mathcal{G}_\sigma^{r,(1)}(n,\varepsilon)\Sigma_0^<(\varepsilon)\\ &+ \frac{\varepsilon_{ac}}{2}\sum_{p=\pm1}\Big[p\partial_\varepsilon G_\sigma^{<,f}(n-p,\varepsilon) + \mathcal{G}_\sigma^{r,(1)}(n-p,\varepsilon)\Big]\\ &+ U\langle\langle d_\sigma, d_\sigma^\dagger n_{\bar\sigma}\rangle\rangle_\sigma^{<,(1)}(n,\varepsilon)\Bigg)\mathscr{G}_\sigma^a(\varepsilon)\,, \qquad \text{(G.31)}\end{aligned}$$

and

$$\begin{aligned}\langle\langle d_\sigma, d_\sigma^\dagger n_{\bar\sigma}\rangle\rangle_\sigma^<(n,\varepsilon) = \Big(&\frac{\varepsilon_{ac}}{2}\sum_{p=\pm1}\langle\langle d_\sigma, d_\sigma^\dagger n_{\bar\sigma}\rangle\rangle_\sigma^{<,f}(n-p,\varepsilon)\\ &+ \langle\langle d_\sigma, d_\sigma^\dagger n_{\bar\sigma}\rangle\rangle_\sigma^{r,f}(n,\varepsilon)\Sigma_0^<(\varepsilon)\Big)\mathscr{G}_\sigma^a(\varepsilon-U)\,, \qquad \text{(G.32)}\\ \langle\langle d_\sigma, d_\sigma^\dagger n_{\bar\sigma}\rangle\rangle_\sigma^{<,(1)}(n,\varepsilon) = \Big(&\langle\langle d_\sigma, d_\sigma^\dagger n_{\bar\sigma}\rangle\rangle_\sigma^{r,(1)}(n,\varepsilon)\Sigma_0^<(\varepsilon)\\ &+ \frac{\varepsilon_{ac}}{2}\sum_{p=\pm1}\Big[p\partial_\varepsilon\langle\langle d_\sigma, d_\sigma^\dagger n_{\bar\sigma}\rangle\rangle_\sigma^{<,f}(n-p,\varepsilon)\\ &+ \langle\langle d_\sigma, d_\sigma^\dagger n_{\bar\sigma}\rangle\rangle_\sigma^{r,(1)}(n-p,\varepsilon)\Big]\Big)\mathscr{G}_\sigma^a(\varepsilon-U)\,. \qquad \text{(G.33)}\end{aligned}$$

Equations (5.21c) and (5.21d) then follow easily.

H. Hartree approximation

In this appendix we study the charge current and dot occupation of the system of Chapter 5 using the Hartree approach[1]. This approximation decouples higher-order correlators of Eq. (5.7) in the following way: $\langle\langle d_\sigma, d_\sigma^\dagger n_{\bar{\sigma}} \rangle\rangle(t,t') \approx G_\sigma(t,t') \langle n_{\bar{\sigma}}(t') \rangle$. Hence, the equation of motion for the Green's function can be exactly solved. We find that both frozen dot occupation and current to first order in $\hbar\Omega$ take the same form as in Eqs. (5.17a) and (5.17b) but replacing $\varepsilon_{ac}(t)$ with $\varepsilon_{ac}(t) + U \langle n(t) \rangle^f$. As a consequence, Eq. (5.17a) becomes a self-consistent equation for $\langle n(t) \rangle^f$ and the dot occupation has to be solved iteratively.

The inset of Fig. H.1 shows the results of our numerical evaluations for the frozen occupation in the Hartree approximation at a fixed value of the dot level varying the interaction strength. We keep the ac amplitude with a large value ($\varepsilon_{ac} = 5\Gamma$). In the frozen regime, the electronic potential is instantaneously adjusted to the variation of the ac field. As a consequence, $\langle n(t) \rangle_H^f$ attains its maximum value when $\Omega t = \pi + 2\pi m$ ($m = 0, 1, \ldots$). In the inset of Fig. H.1 we can observe how the frozen occupation increases during the first half-cycle of the pulse (two electrons, one per spin, are absorbed) whereas during the second half-cycle it decreases (two electrons, one per spin, are emitted). For $U \neq 0$, in the Hartree approximation, we observe that the peak maxima decrease while the minima stay constant when U increases. We attribute this behavior to a repulsion effect that hampers the process of emission and absorption of electrons since an extra energy is to be paid in order to populate the dot.

The main panel of Fig. H.1 presents the total current to first order in the ac frequency. We have checked numerically that the current

---

[1] The contents of this appendix are based on M. I. Alomar, Jong Soo Lim and David Sánchez, J. Phys.: Conf. Ser. **647**, 012049 (2015).

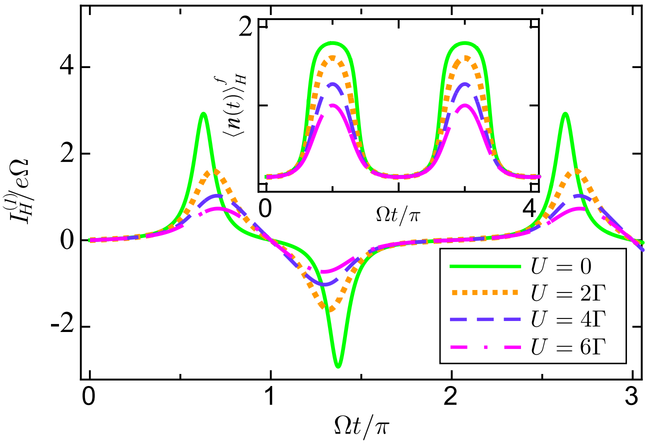

Figure H.1: Time-dependent current in Hartree approximation as a function of time for different values of the Coulomb interaction strength U. In the inset, we plot the frozen dot occupation (also in Hartree approximatioin) as a function of $\Omega t/\pi$ for the same values of U as in the main plot. Parameters: $\varepsilon_0 = 2\Gamma$, $\varepsilon_{ac} = 5\Gamma$ and $k_B T = 0$.

to second order in the ac frequency is much smaller than the first order and then it is enough to understand the current behavior to leading order in Ω. What we observe is that the current presents peaks (dips) during the absorption (emission) part of the process. Between pulses the occupation remains roughly constant and the current is close to zero. As expected, when U increases, the current peaks are significantly lower. Comparing these results with those obtained in the Coulomb blockade regime (see Fig. 5.5) we observe an important difference. In the Hartree approximation our results suggest that mean-field interactions can be understood as an effective ac potential with a lowered amplitude. In contrast, in the Coulomb blockade regime the current peaks (and dips) split indicating that we have two one-electron (and two one-hole) pulses (see Sec. 5.4). We must keep in mind that the Hartree approximation is valid for weak electron-electron Coulomb interaction ($U < \pi\Gamma$) whereas the Coulomb blockade is valid for strong electron-electron Coulomb interaction ($U > \pi\Gamma$).

References

[1] N. F. Mott, *The electrical conductivity of transition metals*, Proc. R. Soc. London **153**, 699 (1936).

[2] N. F. Mott, *The resistance and thermoelectric properties of the transition metals*, Proc. R. Soc. London **156**, 368 (1936).

[3] A. G. Aronov, *Spin injection in metals and polarization of nuclei*, JETP Lett. **24**, 37 (1976).

[4] M. Johnson and R. H. Silsbee, *Thermodynamic analysis of interfacial transport and of the thermomagnetoelectric system*, Phys. Rev. B **35**, 4959 (1987).

[5] M. N. Baibich, J. M. Broto, A. Fert, F. N. Van Dau, F. Petroff, P. Etienne, G. Creuzet, A. Friederich, and J. Chazelas, *Giant magnetoresistance of (001)Fe/(001)Cr magnetic superlattices*, Phys. Rev. Lett. **61**, 2472 (1988).

[6] J. S. Moodera, L. R. Kinder, T. M. Wong, and R. Meservey, *Large magnetoresistance at room temperature in ferromagnetic thin film tunnel junctions*, Phys. Rev. Lett. **74**, 3273 (1995).

[7] J. Fabian, A. Matos-Abiague, C. Ertler, P. Stano, and I. Zutic, *Semiconductor spintronics*, Acta Phys. Slov. **57** (2007).

[8] P. Debray, S. M. S. Rahman, J. Wan, R. S. Newrock, M. Cahay, A. T. Ngo, S. E. Ulloa, S. T. Herbert, M. Muhammad, and M. Johnson, *All-electric quantum point contact spin-polarizer*, Nat. Nanotechnol. **4**, 759 (2009).

[9] M. P. Nowak and B. Szafran, *Spin current source based on a quantum point contact with local spin-orbit interaction*, Appl. Phys. Lett. **103**, 202404 (2013).

[10] S. Datta and B. Das, *Electronic analog of the electro-optic modulator*, Appl. Phys. Lett. **56**, 665 (1990).

[11] J.-P. Fleurial, *Thermoelectric power generation materials: Technology and application opportunities*, JOM **61**, 79 (2009).

[12] G. Chen and A. Shakouri, *Heat transfer in nanostructures for solid-state energy conversion*, J. Heat Transfer **124**, 242 (2001).

[13] D. M. Rowe, *CRC Handbook of thermoelectrics* (CRC Press, USA, 1995).

[14] L. D. Hicks and M. S. Dresselhaus, *Effect of quantum-well structures on the thermoelectric figure of merit*, Phys. Rev. B **47**, 12727 (1993).

[15] K. Uchida, S. Takahashi, K. Harii, J. Ieda, W. Koshibae, K. Ando, S. Maekawa, and E. Saitoh, *Observation of the spin Seebeck effect*, Nature (London) **455**, 778 (2008).

[16] H. J. Goldsmid, *Introduction to thermoelectricity* (Springer, Berlin, 2010).

[17] L. Onsager, *Reciprocal relations in irreversible processes. I.*, Phys. Rev. **37**, 405 (1931).

[18] H. B. G. Casimir, *On Onsager's principle of microscopic reversibility*, Rev. Mod. Phys. **17**, 343 (1945).

[19] M. Büttiker, *Four-terminal phase-coherent conductance*, Phys. Rev. Lett. **57**, 1761 (1986).

[20] A. D. Benoit, S. Washburn, C. P. Umbach, R. B. Laibowitz, and R. A. Webb, *Asymmetry in the magnetoconductance of metal wires and loops*, Phys. Rev. Lett. **57**, 1765 (1986).

[21] J. Matthews, F. Battista, D. Sánchez, P. Samuelsson, and H. Linke, *Experimental verification of reciprocity relations in quantum thermoelectric transport*, Phys. Rev. B **90**, 165428 (2014).

[22] G. E. W. Bauer, A. H. MacDonald, and S. Maekawa, *Spin caloritronics*, Solid State Commun. **150**, 459 (2010).

[23] J. Sinova, S. O. Valenzuela, J. Wunderlich, C. Back, and T. Jungwirth, *Spin Hall effects*, Rev. Mod. Phys. **87**, 1213 (2015).

[24] C. M. Jaworski, J. Yang, S. Mack, D. D. Awschalom, J. P. Heremans, and R. C. Myers, *Observation of the spin-Seebeck effect in a ferromagnetic semiconductor*, Nat. Mater **9**, 898 (2010).

[25] C. M. Jaworski, R. C. Myers, E. Johnston-Halperin, and J. P. Heremans, *Giant spin Seebeck effect in a non-magnetic material*, Nature (London) **487**, 210 (2012).

[26] M. Walter, J. Walowski, V. Zbarsky, M. Münzenberg, M. Schäfers, D. Ebke, G. Reiss, A. Thomas, P. Peretzki, M. Seibt, et al., *Seebeck effect in magnetic tunnel junctions*, Nat. Mater. **10**, 742 (2011).

[27] R. A. Webb, S. Washburn, C. P. Umbach, and R. B. Laibowitz, *Observation of h/e Aharonov-Bohm oscillations in normal-metal rings*, Phys. Rev. Lett. **54**, 2696 (1985).

[28] D. C. Tsui, H. L. Stormer, and A. C. Gossard, *Two-dimensional magnetotransport in the extreme quantum limit*, Phys. Rev. Lett. **48**, 1559 (1982).

[29] A. H. Castro Neto, F. Guinea, N. M. R. Peres, K. S. Novoselov, and A. K. Geim, *The electronic properties of graphene*, Rev. Mod. Phys. **81**, 109 (2009).

[30] K. S. Novoselov, A. K. Geim, S. V. Morozov, D. Jiang, Y. Zhang, S. V. Dubonos, I. V. Grigorieva, and A. A. Firsov, *Electric field effect in atomically thin carbon films*, Science **306**, 666 (2004).

[31] K. S. Novoselov, A. K. Geim, S. V. Morozov, D. Jiang, M. I. Katsnelson, I. V. Grigorieva, S. V. Dubonos, and A. A. Firsov, *Two-dimensional gas of massless Dirac fermions in graphene*, Nature (London) **438**, 197 (2005).

[32] A. K. Geim and K. S. Novoselov, *The rise of graphene*, Nat. Mater. **6**, 183 (2007).

[33] C. W. J. Beenakker, *Colloquium: Andreev reflection and Klein tunneling in graphene*, Rev. Mod. Phys. **80**, 1337 (2008).

[34] A. K. Geim, *Graphene: Status and prospects*, Science **324**, 1530 (2009).

[35] N. W. Ashcroft and N. D. Mermin, *Solid State Physics* (Saunders College, Philadelphia, 1976).

[36] P. R. Wallace, *The band theory of graphite*, Phys. Rev. **71**, 622 (1947).

[37] T. Ihn, *Semiconductor nanostructures: quantum states and electronic transport* (Oxford University Press Inc., New York, 2010).

[38] G. W. Semenoff, *Condensed-matter simulation of a three-dimensional anomaly*, Phys. Rev. Lett. **53**, 2449 (1984).

[39] D. Huertas-Hernando, F. Guinea, and A. Brataas, *Spin-orbit coupling in curved graphene, fullerenes, nanotubes, and nanotube caps*, Phys. Rev. B **74**, 155426 (2006).

[40] H. Min, J. E. Hill, N. A. Sinitsyn, B. R. Sahu, L. Kleinman, and A. H. MacDonald, *Intrinsic and Rashba spin-orbit interactions in graphene sheets*, Phys. Rev. B **74**, 165310 (2006).

[41] A. Varykhalov, J. Sánchez-Barriga, A. M. Shikin, C. Biswas, E. Vescovo, A. Rybkin, D. Marchenko, and O. Rader, *Electronic and magnetic properties of quasifreestanding graphene on Ni*, Phys. Rev. Lett. **101**, 157601 (2008).

[42] Y. S. Dedkov, M. Fonin, U. Rüdiger, and C. Laubschat, *Rashba effect in the graphene/Ni(111) system*, Phys. Rev. Lett. **100**, 107602 (2008).

[43] E. I. Rashba, *Graphene with structure-induced spin-orbit coupling: Spin-polarized states, spin zero modes, and quantum Hall effect*, Phys. Rev. B **79**, 161409 (2009).

[44] C. Ertler, S. Konschuh, M. Gmitra, and J. Fabian, *Electron spin relaxation in graphene: The role of the substrate*, Phys. Rev. B **80**, 041405 (2009).

[45] S. Abdelouahed, A. Ernst, J. Henk, I. V. Maznichenko, and I. Mertig, *Spin-split electronic states in graphene: Effects due to lattice deformation, Rashba effect, and adatoms by first principles*, Phys. Rev. B **82**, 125424 (2010).

[46] Z. Y. Li, Z. Q. Yang, S. Qiao, J. Hu, and R. Q. Wu, *Spin-orbit splitting in graphene on metallic substrates*, J. Phys.: Condens. Matter **23**, 225502 (2011).

[47] E. I. Rashba, *Properties of semiconductors with an extremum loop I. Cyclotron and combinational resonance in a magnetic field perpendicular to the plane of the loop*, Sov. Phys. Solid State **2**, 1109 (1906).

[48] Y. A. Bychkov and E. I. Rashba, *Oscillatory effects and the magnetic susceptibility of carriers in inversion layers*, J. Phys. C: Solid State Phys. **17**, 6039 (1984).

[49] C. L. Kane and E. J. Mele, *Quantum spin Hall effect in graphene*, Phys. Rev. Lett. **95**, 226801 (2005).

[50] C. L. Kane and E. J. Mele, Z_2 *Topological order and the quantum spin Hall effect*, Phys. Rev. Lett. **95**, 146802 (2005).

[51] J. Nitta, T. Akazaki, H. Takayanagi, and T. Enoki, *Gate control of spin-orbit interaction in an inverted* $In_{0.53}Ga_{0.47}As/In_{0.52}Al_{0.48}As$ *heterostructure*, Phys. Rev. Lett. **78**, 1335 (1997).

[52] A. V. Moroz and C. H. W. Barnes, *Effect of the spin-orbit interaction on the band structure and conductance of quasi-one-dimensional systems*, Phys. Rev. B **60**, 14272 (1999).

[53] F. Mireles and G. Kirczenow, *Ballistic spin-polarized transport and Rashba spin precession in semiconductor nanowires*, Phys. Rev. B **64**, 024426 (2001).

[54] S. Konschuh, *Spin-orbit coupling effects from graphene to graphite*, Ph.D. thesis, University of Regensburg (2011).

[55] S. Konschuh, M. Gmitra, and J. Fabian, *Tight-binding theory of the spin-orbit coupling in graphene*, Phys. Rev. B **82**, 245412 (2010).

[56] R. Winkler, *Spin-orbit coupling effects in two-dimensional electron and hole systems* (Springer, Berlin - New York, 2003).

[57] B. J. van Wees, H. van Houten, C. W. J. Beenakker, J. G. Williamson, L. P. Kouwenhoven, D. van der Marel, and C. T. Foxon, *Quantized conductance of point contacts in a two-dimensional electron gas*, Phys. Rev. Lett. **60**, 848 (1988).

[58] D. A. Wharam, T. J. Thornton, R. Newbury, M. Pepper, H. Ahmed, J. E. F. Frost, D. G. Hasko, D. C. Peacock, D. A. Ritchie, and G. A. C. Jones, *One-dimensional transport and the quantisation of the ballistic resistance*, J. Phys. C: Solid State Phys. **21**, L209 (1988).

[59] S. Lindemann, T. Ihn, T. Heinzel, W. Zwerger, K. Ensslin, K. Maranowski, and A. C. Gossard, *Stability of spin states in quantum dots*, Phys. Rev. B **66**, 195314 (2002).

[60] A. Yamakage, K.-I. Imura, J. Cayssol, and Y. Kuramoto, *Spin-orbit effects in a graphene bipolar pn junction*, Europhys. Lett. **87**, 47005 (2009).

[61] M. Rataj and J. Barnaś, *Graphene p-n junctions with nonuniform Rashba spin-orbit coupling*, Appl. Phys. Lett. **99**, 162107 (2011).

[62] T. Stauber and J. Schliemann, *Electronic properties of graphene and graphene nanoribbons with 'pseudo-Rashba' spin-orbit coupling*, New J. Phys. **11**, 115003 (2009).

[63] K. Shakouri, M. R. Masir, A. Jellal, E. B. Choubabi, and F. M. Peeters, *Effect of spin-orbit couplings in graphene with and without potential modulation*, Phys. Rev. B **88**, 115408 (2013).

[64] D. Bercioux and A. De Martino, *Spin-resolved scattering through spin-orbit nanostructures in graphene*, Phys. Rev. B **81**, 165410 (2010).

[65] M.-H. Liu, J. Bundesmann, and K. Richter, *Spin-dependent Klein tunneling in graphene: Role of Rashba spin-orbit coupling*, Phys. Rev. B **85**, 085406 (2012).

[66] D. Dragoman and M. Dragoman, *Giant thermoelectric effect in graphene*, Appl. Phys. Lett. **91**, 203116 (2007).

[67] Y. M. Zuev, W. Chang, and P. Kim, *Thermoelectric and magnetothermoelectric transport measurements of graphene*, Phys. Rev. Lett. **102**, 096807 (2009).

[68] P. Wei, W. Bao, Y. Pu, C. N. Lau, and J. Shi, *Anomalous thermoelectric transport of Dirac particles in graphene*, Phys. Rev. Lett. **102**, 166808 (2009).

[69] O. Shevtsov, P. Carmier, C. Groth, X. Waintal, and D. Carpentier, *Tunable thermopower in a graphene-based topological insulator*, Phys. Rev. B **85**, 245441 (2012).

[70] L. Serra, D. Sánchez, and R. López, *Evanescent states in quantum wires with Rashba spin-orbit coupling*, Phys. Rev. B **76**, 045339 (2007).

[71] M. Khodas, A. Shekhter, and A. M. Finkel'stein, *Spin polarization of electrons by nonmagnetic heterostructures: The basics of spin optics*, Phys. Rev. Lett. **92**, 086602 (2004).

[72] M. I. Katsnelson, K. S. Novoselov, and A. K. Geim, *Chiral tunnelling and the Klein paradox in graphene*, Nat. Phys. **2**, 620 (2006).

[73] C. W. J. Beenakker and H. van Houten, *Quantum transport in semiconductor nanostructures*, Solid State Physics **44**, 1 (1991).

[74] T. Rejec, R. Žitko, J. Mravlje, and A. Ramšak, *Spin thermopower in interacting quantum dots*, Phys. Rev. B **85**, 085117 (2012).

[75] J. S. Lim, R. López, and D. Sánchez, *Orbital caloritronic transport in strongly interacting quantum dots*, New J. Phys. **16**, 015003 (2014).

[76] A. S. Dzurak, C. G. Smith, C. H. W. Barnes, M. Pepper, L. Martín-Moreno, C. T. Liang, D. A. Ritchie, and G. A. C. Jones, *Thermoelectric signature of the excitation spectrum of a quantum dot*, Phys. Rev. B **55**, R10197 (1997).

[77] P. Streda, *Quantised thermopower of a channel in the ballistic regime*, J. Phys.: Condens. Matter **1**, 1025 (1989).

[78] H. v. Houten, L. W. Molenkamp, C. W. J. Beenakker, and C. T. Foxon, *Thermo-electric properties of quantum point contacts*, Semicond. Sci. Technol. **7**, B215 (1992).

[79] M. Cutler and N. F. Mott, *Observation of Anderson localization in an electron gas*, Phys. Rev. **181**, 1336 (1969).

[80] Z. Ma, *Spin Hall effect generated by a temperature gradient and heat current in a two-dimensional electron gas*, Solid State Commun. **150**, 510 (2010).

[81] C. M. Wang and M. Q. Pang, *Thermally induced spin polarization and thermal conductivities in a spin-orbit-coupled two-dimensional electron gas*, Solid State Commun. **150**, 1509 (2010).

[82] A. Dyrdał, M. Inglot, V. K. Dugaev, and J. Barnaś, *Thermally induced spin polarization of a two-dimensional electron gas*, Phys. Rev. B **87**, 245309 (2013).

[83] J. Borge, C. Gorini, and R. Raimondi, *Spin thermoelectrics in a disordered Fermi gas*, Phys. Rev. B **87**, 085309 (2013).

[84] P. E. Iglesias and J. A. Maytorena, *Absence of thermospin current response of a spin-orbit-coupled two-dimensional electron gas*, Phys. Rev. B **89**, 155432 (2014).

[85] D. Sánchez and L. Serra, *Fano-Rashba effect in a quantum wire*, Phys. Rev. B **74**, 153313 (2006).

[86] C. S. Lent and D. J. Kirkner, *The quantum transmitting boundary method*, J. Appl. Phys. **67**, 6353 (1990).

[87] D. J. Griffiths, *Introduction to quantum mechanics* (Pearson Prentice Hall, Upper Saddle River, New Jersey, 2005).

[88] G. Schmidt, D. Ferrand, L. W. Molenkamp, A. T. Filip, and B. J. van Wees, *Fundamental obstacle for electrical spin injection from a ferromagnetic metal into a diffusive semiconductor*, Phys. Rev. B **62**, R4790 (2000).

[89] E. I. Rashba, *Theory of electrical spin injection: Tunnel contacts as a solution of the conductivity mismatch problem*, Phys. Rev. B **62**, R16267 (2000).

[90] A. Slobodskyy, C. Gould, T. Slobodskyy, G. Schmidt, L. W. Molenkamp, and D. Sánchez, *Resonant tunneling diode with spin polarized injector*, Appl. Phys. Lett. **90**, 122109 (2007).

[91] M. Cahay and S. Bandyopadhyay, *Conductance modulation of spin interferometers*, Phys. Rev. B **68**, 115316 (2003).

[92] M. M. Gelabert and L. Serra, *Conductance oscillations of a spin-orbit stripe with polarized contacts*, Eur. Phys. J. B **79**, 341 (2011).

[93] A. A. M. Staring, L. W. Molenkamp, B. W. Alphenaar, H. v. Houten, O. J. A. Buyk, M. A. A. Mabesoone, C. W. J. Beenakker, and C. T. Foxon, *Coulomb-blockade oscillations in the thermopower of a quantum dot*, Europhys. Lett. **22**, 57 (1993).

[94] S. F. Svensson, E. A. Hoffmann, N. Nakpathomkun, P. M. Wu, H. Q. Xu, H. A. Nilsson, D. Sánchez, V. Kashcheyevs, and H. Linke, *Nonlinear thermovoltage and thermocurrent in quantum dots*, New J. Phys. **15**, 105011 (2013).

[95] P. Reddy, S.-Y. Jang, R. A. Segalman, and A. Majumdar, *Thermoelectricity in molecular junctions*, Science **315**, 1568 (2007).

[96] J. Schliemann, J. C. Egues, and D. Loss, *Nonballistic spin-field-effect transistor*, Phys. Rev. Lett. **90**, 146801 (2003).

[97] K. C. Hall, W. H. Lau, K. Gündoğdu, M. E. Flatté, and T. F. Boggess, *Nonmagnetic semiconductor spin transistor*, Appl. Phys. Lett. **83**, 2937 (2003).

[98] B. Wang, J. Wang, and H. Guo, *Quantum spin field effect transistor*, Phys. Rev. B **67**, 092408 (2003).

[99] D. D. Awschalom and N. Samarth, *Spintronics without magnetism*, Physics **2** (2009).

[100] J. Wunderlich, B.-G. Park, A. C. Irvine, L. P. Zârbo, E. Rozkotová, P. Nemec, V. Novák, J. Sinova, and T. Jungwirth, *Spin Hall effect transistor*, Science **330**, 1801 (2010).

[101] J.-F. Liu, K. S. Chan, and J. Wang, *Nonmagnetic spin-field-effect transistor*, Appl. Phys. Lett. **101**, 082407 (2012).

[102] V. A. Sablikov and Y. Y. Tkach, *Evanescent states in two-dimensional electron systems with spin-orbit interaction and spin-dependent transmission through a barrier*, Phys. Rev. B **76**, 245321 (2007).

[103] A. Voskoboynikov, S. S. Liu, and C. P. Lee, *Spin-dependent tunneling in double-barrier semiconductor heterostructures*, Phys. Rev. B **59**, 12514 (1999).

[104] E. A. de Andrada e Silva and G. C. La Rocca, *Electron-spin polarization by resonant tunneling*, Phys. Rev. B **59**, R15583 (1999).

[105] T. Koga, J. Nitta, H. Takayanagi, and S. Datta, *Spin-filter device based on the Rashba effect using a nonmagnetic resonant tunneling diode*, Phys. Rev. Lett. **88**, 126601 (2002).

[106] D. Z.-Y. Ting and X. Cartoixà, *Resonant interband tunneling spin filter*, Appl. Phys. Lett. **81**, 4198 (2002).

[107] M. M. Glazov, P. S. Alekseev, M. A. Odnoblyudov, V. M. Chistyakov, S. A. Tarasenko, and I. N. Yassievich, *Spin-dependent resonant tunneling in symmetrical double-barrier structures*, Phys. Rev. B **71**, 155313 (2005).

[108] G. Isić, D. Indjin, V. Milanović, J. Radovanović, Z. Ikonić, and P. Harrison, *Phase-breaking effects in double-barrier resonant tunneling diodes with spin-orbit interaction*, J. Appl. Phys. **108**, 044506 (2010).

[109] P. Chuang, S.-C. Ho, L. W. Smith, F. Sfigakis, M. Pepper, C.-H. Chen, J.-C. Fan, J. P. Griffiths, I. Farrer, H. E. Beere, et al., *All-electric all-semiconductor spin field-effect transistors*, Nat. Nanotechnol. **10**, 35 (2015).

[110] R. S. Calsaverini, E. Bernardes, J. C. Egues, and D. Loss, *Intersubband-induced spin-orbit interaction in quantum wells*, Phys. Rev. B **78**, 155313 (2008).

[111] F. Dettwiler, J. Fu, S. Mack, P. J. Weigele, J. C. Egues, D. D. Awschalom, and D. M. Zumbühl, *Electrical spin protection and manipulation via gate-locked spin-orbit fields*, arXiv:1403.3518 [cond-mat] (2014).

[112] S. M. Frolov, S. Luescher, W. Yu, Y. Ren, J. A. Folk, and W. Wegscheider, *Ballistic spin resonance*, Nature (London) **458**, 868 (2009).

[113] M. O. Hachiya, G. Usaj, and J. C. Egues, *Ballistic spin resonance in multisubband quantum wires*, Phys. Rev. B **89** (2014).

[114] L. W. Molenkamp, G. Schmidt, and G. E. W. Bauer, *Rashba Hamiltonian and electron transport*, Phys. Rev. B **64**, 121202 (2001).

[115] R. López, D. Sánchez, and L. Serra, *From Coulomb blockade to the Kondo regime in a Rashba dot*, Phys. Rev. B **76**, 035307 (2007).

[116] E. Ott, *Chaos in dynamical systems* (Cambridge University Press, New York, 1993).

[117] I. M. Ruzin, V. Chandrasekhar, E. I. Levin, and L. I. Glazman, *Stochastic Coulomb blockade in a double-dot system*, Phys. Rev. B **45**, 13469 (1992).

[118] D. Sánchez, G. Platero, and L. L. Bonilla, *Quasiperiodic current and strange attractors in ac-driven superlattices*, Phys. Rev. B **63**, 201306 (2001).

[119] M. M. Gelabert, L. Serra, D. Sánchez, and R. López, *Multichannel effects in Rashba quantum wires*, Phys. Rev. B **81**, 165317 (2010).

[120] I. A. Shelykh and N. G. Galkin, *Fano and Breit-Wigner resonances in carrier transport through Datta and Das spin modulators*, Phys. Rev. B **70**, 205328 (2004).

[121] X. F. Wang, *Spin transport of electrons through quantum wires with a spatially modulated Rashba spin-orbit interaction*, Phys. Rev. B **69**, 035302 (2004).

[122] L. Zhang, P. Brusheim, and H. Q. Xu, *Multimode electron transport through quantum waveguides with spin-orbit interaction modulation: Applications of the scattering matrix formalism*, Phys. Rev. B **72**, 045347 (2005).

[123] S. Souma, A. Sawada, H. Chen, Y. Sekine, M. Eto, and T. Koga, *Spin blocker using the interband Rashba effect in symmetric double quantum wells*, Phys. Rev. Appl. **4**, 034010 (2015).

[124] A. V. Moroz and C. H. W. Barnes, *Spin-orbit interaction as a source of spectral and transport properties in quasi-one-dimensional systems*, Phys. Rev. B **61**, R2464 (2000).

[125] C. Cohen-Tannoudji, B. Diu, and F. Laloë, *Quantum mechanics* (Wiley-Interscience, New York, 1977).

[126] L. Baskin, P. Neittaanmäki, B. Plamenevskii, and O. Sarafanov, *Resonant tunneling. Quantum waveguides of variable cross-section, asymptotics, numerics, and applications* (Springer, Cham, Switzerland, 2015).

[127] J. Gabelli, G. Fève, J.-M. Berroir, B. Plaçais, A. Cavanna, B. Etienne, Y. Jin, and D. C. Glattli, *Violation of Kirchhoff's laws for a coherent RC circuit*, Science **313**, 499 (2006).

[128] G. Fève, A. Mahé, J.-M. Berroir, T. Kontos, B. Plaçais, D. C. Glattli, A. Cavanna, B. Etienne, and Y. Jin, *An on-demand coherent single-electron source*, Science **316**, 1169 (2007).

[129] J. Gabelli, G. Fève, J.-M. Berroir, and B. Plaçais, *A coherent RC circuit*, Rep. Prog. Phys. **75**, 126504 (2012).

[130] M. Büttiker, A. Prêtre, and H. Thomas, *Dynamic conductance and the scattering matrix of small conductors*, Phys. Rev. Lett. **70**, 4114 (1993).

[131] A. Prêtre, H. Thomas, and M. Büttiker, *Dynamic admittance of mesoscopic conductors: Discrete-potential model*, Phys. Rev. B **54**, 8130 (1996).

[132] M. Büttiker, H. Thomas, and A. Prêtre, *Mesoscopic capacitors*, Phys. Lett. A **180**, 364 (1993).

[133] P. Michler, A. Kiraz, C. Becher, W. V. Schoenfeld, P. M. Petroff, L. Zhang, E. Hu, and A. Imamoglu, *A quantum dot single-photon turnstile device*, Science **290**, 2282 (2000).

[134] C. Santori, M. Pelton, G. Solomon, Y. Dale, and Y. Yamamoto, *Triggered single photons from a quantum dot*, Phys. Rev. Lett. **86**, 1502 (2001).

[135] L. S. Levitov, H. Lee, and G. B. Lesovik, *Electron counting statistics and coherent states of electric current*, J. Math. Phys. **37**, 4845 (1996).

[136] D. A. Ivanov, H. W. Lee, and L. S. Levitov, *Coherent states of alternating current*, Phys. Rev. B **56**, 6839 (1997).

[137] J. Keeling, I. Klich, and L. S. Levitov, *Minimal excitation states of electrons in one-dimensional wires*, Phys. Rev. Lett. **97**, 116403 (2006).

[138] J. Dubois, T. Jullien, C. Grenier, P. Degiovanni, P. Roulleau, and D. C. Glattli, *Integer and fractional charge Lorentzian voltage pulses analyzed in the framework of photon-assisted shot noise*, Phys. Rev. B **88**, 085301 (2013).

[139] J. Dubois, T. Jullien, F. Portier, P. Roche, A. Cavanna, Y. Jin, W. Wegscheider, P. Roulleau, and D. C. Glattli, *Minimal-excitation states for electron quantum optics using levitons*, Nature (London) **502**, 659 (2013).

[140] J. P. Pekola, O.-P. Saira, V. F. Maisi, A. Kemppinen, M. Möttönen, Y. A. Pashkin, and D. V. Averin, *Single-electron current sources: Toward a refined definition of the ampere*, Rev. Mod. Phys. **85**, 1421 (2013).

[141] S. Ol'khovskaya, J. Splettstoesser, M. Moskalets, and M. Büttiker, *Shot noise of a mesoscopic two-particle collider*, Phys. Rev. Lett. **101**, 166802 (2008).

[142] J. Splettstoesser, M. Moskalets, and M. Büttiker, *Two-particle nonlocal Aharonov-Bohm effect from two single-particle emitters*, Phys. Rev. Lett. **103**, 076804 (2009).

[143] Y. Sherkunov, N. d'Ambrumenil, P. Samuelsson, and M. Büttiker, *Optimal pumping of orbital entanglement with single-particle emitters*, Phys. Rev. B **85**, 081108 (2012).

[144] H. Grabert and M. H. Devoret, *Single charge tunneling* (Plenum Press, New York, 1992).

[145] H. W. C. Postma, T. Teepen, Z. Yao, M. Grifoni, and C. Dekker, *Carbon nanotube single-electron transistors at room temperature*, Science **293**, 76 (2001).

[146] J. Park, A. N. Pasupathy, J. I. Goldsmith, C. Chang, Y. Yaish, J. R. Petta, M. Rinkoski, J. P. Sethna, H. D. Abruña, P. L. McEuen, et al., *Coulomb blockade and the Kondo effect in single-atom transistors*, Nature (London) **417**, 722 (2002).

[147] P. Cheinet, S. Trotzky, M. Feld, U. Schnorrberger, M. Moreno-Cardoner, S. Fölling, and I. Bloch, *Counting atoms using interaction blockade in an optical superlattice*, Phys. Rev. Lett. **101**, 090404 (2008).

[148] S. E. Nigg, R. López, and M. Büttiker, *Mesoscopic charge relaxation*, Phys. Rev. Lett. **97**, 206804 (2006).

[149] M. Büttiker and S. E. Nigg, *Mesoscopic capacitance oscillations*, Nanotechnol. **18**, 044029 (2007).

[150] S. E. Nigg and M. Büttiker, *Quantum to classical transition of the charge relaxation resistance of a mesoscopic capacitor*, Phys. Rev. B **77**, 085312 (2008).

[151] Z. Ringel, Y. Imry, and O. Entin-Wohlman, *Delayed currents and interaction effects in mesoscopic capacitors*, Phys. Rev. B **78**, 165304 (2008).

[152] Y. I. Rodionov, I. S. Burmistrov, and A. S. Ioselevich, *Charge relaxation resistance in the Coulomb blockade problem*, Phys. Rev. B **80**, 035332 (2009).

[153] C. Mora and K. Le Hur, *Universal resistances of the quantum resistance-capacitance circuit*, Nat. Phys. **6**, 697 (2010).

[154] Y. Hamamoto, T. Jonckheere, T. Kato, and T. Martin, *Dynamic response of a mesoscopic capacitor in the presence of strong electron interactions*, Phys. Rev. B **81**, 153305 (2010).

[155] J. Splettstoesser, M. Governale, J. König, and M. Büttiker, *Charge and spin dynamics in interacting quantum dots*, Phys. Rev. B **81**, 165318 (2010).

[156] M. Albert, C. Flindt, and M. Büttiker, *Accuracy of the quantum capacitor as a single-electron source*, Phys. Rev. B **82**, 041407 (2010).

[157] M. Filippone, K. Le Hur, and C. Mora, *Giant charge relaxation resistance in the Anderson model*, Phys. Rev. Lett. **107**, 176601 (2011).

[158] M. Lee, R. López, M.-S. Choi, T. Jonckheere, and T. Martin, *Effect of many-body correlations on mesoscopic charge relaxation*, Phys. Rev. B **83**, 201304 (2011).

[159] M. Filippone and C. Mora, *Fermi liquid approach to the quantum RC circuit: Renormalization group analysis of the Anderson and Coulomb blockade models*, Phys. Rev. B **86**, 125311 (2012).

[160] L. D. Contreras-Pulido, J. Splettstoesser, M. Governale, J. König, and M. Büttiker, *Time scales in the dynamics of an interacting quantum dot*, Phys. Rev. B **85**, 075301 (2012).

[161] O. Kashuba, H. Schoeller, and J. Splettstoesser, *Nonlinear adiabatic response of interacting quantum dots*, Europhys. Lett. **98**, 57003 (2012).

[162] P. Dutt, T. L. Schmidt, C. Mora, and K. Le Hur, *Strongly correlated dynamics in multichannel quantum RC circuits*, Phys. Rev. B **87**, 155134 (2013).

[163] J. S. Lim, R. López, and D. Sánchez, *Dynamic thermoelectric and heat transport in mesoscopic capacitors*, Phys. Rev. B **88**, 201304 (2013).

[164] G. Rosselló, R. López, and J. S. Lim, *Time-dependent heat flow in interacting quantum conductors*, Phys. Rev. B **92**, 115402 (2015).

[165] I. S. Burmistrov and Y. I. Rodionov, *Charge relaxation resistance in the cotunneling regime of multichannel Coulomb blockade: Violation of Korringa-Shiba relation*, Phys. Rev. B **92**, 195412 (2015).

[166] M. Moskalets, P. Samuelsson, and M. Büttiker, *Quantized dynamics of a coherent capacitor*, Phys. Rev. Lett. **100**, 086601 (2008).

[167] A.-P. Jauho, N. S. Wingreen, and Y. Meir, *Time-dependent transport in interacting and noninteracting resonant-tunneling systems*, Phys. Rev. B **50**, 5528 (1994).

[168] H. Haug and A.-P. Jauho, *Quantum kinetics in transport and optics of semiconductors* (Springer, Berlin, 2008).

[169] L. Arrachea, *Green-function approach to transport phenomena in quantum pumps*, Phys. Rev. B **72**, 125349 (2005).

[170] L. Arrachea and M. Moskalets, *Relation between scattering-matrix and Keldysh formalisms for quantum transport driven by time-periodic fields*, Phys. Rev. B **74**, 245322 (2006).

[171] M. Moskalets and M. Büttiker, *Heat production and current noise for single- and double-cavity quantum capacitors*, Phys. Rev. B **80**, 081302 (2009).

[172] M. V. Moskalets, *Scattering matrix approach to non-stationary quantum transport* (Imperial College Press, London, 2012).

[173] J. Wang, B. Wang, and H. Guo, *Quantum inductance and negative electrochemical capacitance at finite frequency in a two-plate quantum capacitor*, Phys. Rev. B **75**, 155336 (2007).

[174] R. Van Roermund, S.-y. Shiau, and M. Lavagna, *Anderson model out of equilibrium: Decoherence effects in transport through a quantum dot*, Phys. Rev. B **81**, 165115 (2010).

[175] M. F. Ludovico, J. S. Lim, M. Moskalets, L. Arrachea, and D. Sánchez, *Dynamical energy transfer in ac-driven quantum systems*, Phys. Rev. B **89**, 161306 (2014).

[176] M. F. Ludovico, M. Moskalets, D. Sánchez, and L. Arrachea, *Dynamics of energy transport and entropy production in ac-driven quantum electron systems*, Phys. Rev. B **94**, 035436 (2016).

[177] E. Muñoz, *Phonon-limited transport coefficients in extrinsic graphene*, J. Phys.: Condens. Matter **24**, 195302 (2012).

[178] N. M. Gabor, J. C. W. Song, Q. Ma, N. L. Nair, T. Taychatanapat, K. Watanabe, T. Taniguchi, L. S. Levitov, and P. Jarillo-Herrero, *Hot carrier-assisted intrinsic photoresponse in graphene*, Science **334**, 648 (2011).

[179] L. Chico, A. Latgé, and L. Brey, *Symmetries of quantum transport with Rashba spin–orbit: graphene spintronics*, Phys. Chem. Chem. Phys. **17**, 16469 (2015).

[180] B. Z. Rameshti and A. G. Moghaddam, *Spin-dependent Seebeck effect and spin caloritronics in magnetic graphene*, Phys. Rev. B **91**, 155407 (2015).

[181] Z. Ping Niu and S. Dong, *Valley and spin thermoelectric transport in ferromagnetic silicene junctions*, Appl. Phys. Lett. **104**, 202401 (2014).

[182] I. Appelbaum, B. Huang, and D. J. Monsma, *Electronic measurement and control of spin transport in silicon*, Nature (London) **447**, 295 (2007).

[183] C. L. Dennis, C. Sirisathitkul, G. J. Ensell, J. F. Gregg, and S. M. Thompson, *High current gain silicon-based spin transistor*, J. Phys. D: Appl. Phys. **36**, 81 (2003).

[184] S. Cho, Y.-F. Chen, and M. S. Fuhrer, *Gate-tunable graphene spin valve*, Appl. Phys. Lett. **91**, 123105 (2007).

[185] Y. G. Semenov, K. W. Kim, and J. M. Zavada, *Spin field effect transistor with a graphene channel*, Appl. Phys. Lett. **91**, 153105 (2007).

[186] M.-K. Lee, N.-Y. Lue, C.-K. Wen, and G. Y. Wu, *Valley-based field-effect transistors in graphene*, Phys. Rev. B **86**, 165411 (2012).

[187] M. I. Alomar and D. Sánchez, *Thermoelectric effects in graphene with local spin-orbit interaction*, Phys. Rev. B **89**, 115422 (2014).

[188] A. Dankert, L. Langouche, M. V. Kamalakar, and S. P. Dash, *High-performance molybdenum disulfide field-effect transistors with spin tunnel contacts*, ACS Nano **8**, 476 (2014).

[189] T. Ando, A. B. Fowler, and F. Stern, *Electronic properties of two-dimensional systems*, Rev. Mod. Phys. **54**, 437 (1982).

[190] C. L. Yang, J. Zhang, R. R. Du, J. A. Simmons, and J. L. Reno, *Zener tunneling between landau orbits in a high-mobility two-dimensional electron gas*, Phys. Rev. Lett. **89**, 076801 (2002).

[191] X. Lou, C. Adelmann, S. A. Crooker, E. S. Garlid, J. Zhang, K. S. M. Reddy, S. D. Flexner, C. J. Palmstrøm, and P. A. Crowell, *Electrical detection of spin transport in lateral ferromagnet-semiconductor devices*, Nat. Phys. **3**, 197 (2007).

[192] A. D. Stone and P. A. Lee, *Effect of inelastic processes on resonant tunneling in one dimension*, Phys. Rev. Lett. **54**, 1196 (1985).

[193] M. Büttiker, *Coherent and sequential tunneling in series barriers*, IBM J. Res. Dev. **32**, 63 (1988).

[194] A. D. Martin, M. L. F. Lerch, P. E. Simmonds, and L. Eaves, *Observation of intrinsic tristability in a resonant tunneling structure*, Appl. Phys. Lett. **64**, 1248 (1994).

[195] A. Slobodskyy, C. Gould, T. Slobodskyy, C. R. Becker, G. Schmidt, and L. W. Molenkamp, *Voltage-controlled spin selection in a magnetic resonant tunneling diode*, Phys. Rev. Lett. **90**, 246601 (2003).

[196] P. Wójcik, J. Adamowski, M. Wołoszyn, and B. J. Spisak, *Spin filter effect at room temperature in GaN/GaMnN ferromagnetic resonant tunnelling diode*, Appl. Phys. Lett. **102**, 242411 (2013).

[197] J. C. Egues, C. Gould, G. Richter, and L. W. Molenkamp, *Spin filtering and magnetoresistance in ballistic tunnel junctions*, Phys. Rev. B **64**, 195319 (2001).

[198] C. M. Marcus, A. J. Rimberg, R. M. Westervelt, P. F. Hopkins, and A. C. Gossard, *Conductance fluctuations and chaotic scattering in ballistic microstructures*, Phys. Rev. Lett. **69**, 506 (1992).

[199] I. L. Aleiner, P. W. Brouwer, and L. I. Glazman, *Quantum effects in Coulomb blockade*, Phys. Rep. **358**, 309 (2002).

[200] G. P. Lansbergen, Y. Ono, and A. Fujiwara, *Donor-based single electron pumps with tunable donor binding energy*, Nano Lett. **12**, 763 (2012).

[201] B. Roche, R.-P. Riwar, B. Voisin, E. Dupont-Ferrier, R. Wacquez, M. Vinet, M. Sanquer, J. Splettstoesser, and X. Jehl, *A two-atom electron pump*, Nature Commun. **4**, 1581 (2013).

[202] G. C. Tettamanzi, R. Wacquez, and S. Rogge, *Charge pumping through a single donor atom*, New J. Phys. **16**, 063036 (2014).

[203] M. R. Delbecq, V. Schmitt, F. D. Parmentier, N. Roch, J. J. Viennot, G. Fève, B. Huard, C. Mora, A. Cottet, and T. Kontos, *Coupling a quantum dot, fermionic leads, and a microwave cavity on a chip*, Phys. Rev. Lett. **107**, 256804 (2011).

[204] T. Frey, P. J. Leek, M. Beck, A. Blais, T. Ihn, K. Ensslin, and A. Wallraff, *Dipole coupling of a double quantum dot to a microwave resonator*, Phys. Rev. Lett. **108**, 046807 (2012).

[205] A. Cottet, T. Kontos, and B. Douçot, *Electron-photon coupling in mesoscopic quantum electrodynamics*, Phys. Rev. B **91**, 205417 (2015).

[206] L. Bruhat, J. Viennot, M. Dartiailh, M. Desjardins, T. Kontos, and A. Cottet, *Cavity photons as a probe for charge relaxation resistance and photon emission in a quantum dot coupled to normal and superconducting continua*, Phys. Rev. X **6**, 021014 (2016).

[207] F. Battista and P. Samuelsson, *Proposal for nonlocal electron-hole turnstile in the quantum Hall regime*, Phys. Rev. B **83**, 125324 (2011).

[208] F. Battista and P. Samuelsson, *Spectral distribution and wave function of electrons emitted from a single-particle source in the quantum Hall regime*, Phys. Rev. B **85**, 075428 (2012).

[209] L. P. Kouwenhoven, S. Jauhar, J. Orenstein, P. L. McEuen, Y. Nagamune, J. Motohisa, and H. Sakaki, *Observation of photon-assisted tunneling through a quantum dot*, Phys. Rev. Lett. **73**, 3443 (1994).

[210] A. Kogan, S. Amasha, and M. A. Kastner, *Photon-induced Kondo satellites in a single-electron transistor*, Science **304**, 1293 (2004).

[211] Y. M. Blanter and M. Büttiker, *Shot noise in mesoscopic conductors*, Physics Reports **336**, 1 (2000).

[212] B. H. Bransden and C. J. Joachain, *Physics of atoms and molecules* (Longman Scientific and Technical, New York, 1983).